

# Frequency Stabilization of a 729 nm Ti:Sa Laser for Qubit Manipulation in Trapped Calcium Ions

A master's thesis submitted to the faculty of mathematics,  
computer science and physics, of the University of Innsbruck  
in partial fulfillment of the requirements for the degree of

**Master of Science (MSc)**

carried out at the Institute of Experimental Physics  
under the supervision of

o.Univ.-Prof. Dr. Rainer Blatt,  
Asst.-Prof. Dr. Ben Lanyon

presented by

**Armin Winkler**

March 12, 2023

# Abstract

Quantum information science experiments with trapped  $^{40}\text{Ca}^+$  ions require a narrow-line-width laser at a wavelength of 729 nm to drive the qubit transition between  $4^2\text{S}_{1/2}$  and  $3^2\text{D}_{5/2}$ . In this thesis, a Titanium:Sapphire laser is presented that is frequency-stabilized to a reference cavity at a wavelength of 729 nm using the Pound-Drever-Hall technique. The laser linewidth was measured through beat measurements with other frequency-stabilized lasers and Ramsey experiments on a single trapped  $^{40}\text{Ca}^+$  ion. The narrowest measured linewidth (FWHM) was obtained via a beat measurement and is 4.2(17) Hz at a measurement time of 1 s, representing an upper limit for the Titanium:Sapphire laser linewidth. This narrowest linewidth was achieved after a vibration-isolation board was installed underneath the reference cavity. An analysis of the installed fiber noise cancellation and laser intensity stabilization suggests that fiber and laser intensity noise do not limit the narrowest measured linewidth. The beat measurements with other frequency-stabilized lasers were additionally used to obtain a value for the stabilized laser's frequency drift, which is measured to be -371(3) mHz/s.

# Zusammenfassung

Quanteninformationsexperimente mit gefangenen  $^{40}\text{Ca}^+$  Ionen benötigen einen schmalbandigen Laser bei einer Wellenlänge von 729 nm zum Anregen des Qubitübergangs zwischen  $4^2\text{S}_{1/2}$  und  $3^2\text{D}_{5/2}$ . In dieser Arbeit wird ein Titan:Saphir-Laser beschrieben, welcher bei einer Wellenlänge von 729 nm mithilfe des Pound-Drever-Hall-Verfahrens auf einen externen Resonator frequenzstabilisiert wird. Die Laserlinienbreite wurde mittels Schwebungsmessungen mit anderen frequenzstabilisierten Lasern und Ramsey-Experimenten mit einem einzelnen gefangenen  $^{40}\text{Ca}^+$  gemessen. Die niedrigste gemessene Linienbreite (FWHM) wurde mittels einer Schwebungsmessung erhalten und beträgt 4.2(17) Hz bei einer Messzeit von 1 s, was eine obere Grenze für die Linienbreite des Titan:Saphir-Lasers darstellt. Diese niedrigste Linienbreite wurde erreicht, nachdem eine Vibrationsisolationsplatte unter dem Resonator installiert wurde. Eine Analyse der installierten Faserrauschunterdrückung und Laserintensitätsstabilisierung legt nahe, dass Faser- und Laserintensitätsrauschen die niedrigste gemessene Linienbreite nicht limitieren. Die Schwebungsmessungen mit anderen frequenzstabilisierten Lasern wurden zusätzlich verwendet, um einen Wert für die Drift der Laserfrequenz des stabilisierten Lasers zu erhalten, und die gemessene Drift ist -371(3) mHz/s.

# Contents

<b>1. Introduction</b>	<b>1</b>
<b>2. Quantum Information Science with Trapped Ions</b>	<b>4</b>
2.1. Quantum Mechanics and Qubits . . . . .	4
2.2. Encoding and Manipulating Qubits in Trapped $^{40}\text{Ca}^+$ . . . . .	8
2.2.1. Laser-ion interaction in the quadrupole approximation . . . . .	8
2.2.2. Initialization, manipulation and measurement of the encoded qubit . . . . .	14
2.2.3. Performing a universal gate set using $^{40}\text{Ca}^+$ . . . . .	15
<b>3. Laser Physics</b>	<b>19</b>
3.1. Laser Theory . . . . .	19
3.1.1. Principle of work of a laser . . . . .	19
3.1.2. Laser beams . . . . .	21
3.1.3. Laser linewidth . . . . .	23
3.2. Measuring the Laser Linewidth . . . . .	25
3.2.1. Beat measurement . . . . .	25
3.2.2. Ramsey experiment . . . . .	27
3.3. The Titanium:Sapphire Laser . . . . .	29
<b>4. The Pound-Drever-Hall Locking Technique</b>	<b>30</b>
4.1. Control Theory . . . . .	30
4.1.1. Principles of control theory . . . . .	30
4.1.2. PID control . . . . .	32
4.2. An Optical Cavity as a Frequency Reference . . . . .	33
4.3. The Pound-Drever-Hall (PDH) Technique . . . . .	36
4.3.1. Motivation and outline of the PDH technique . . . . .	36
4.3.2. Summarized derivation of the PDH error signal . . . . .	37
<b>5. The Experimental Setup</b>	<b>42</b>
5.1. The MSquared SolsTiS and Equinox Lasers . . . . .	42
5.1.1. Operating the SolsTiS and Equinox . . . . .	42
5.1.2. Elements in the SolsTiS bowtie . . . . .	43
5.2. Reference Cavity Characteristics . . . . .	45
5.3. The Experimental Setup at UIBK . . . . .	46
5.3.1. Overview of the experimental setup at UIBK . . . . .	46
5.3.2. Intensity stabilization . . . . .	49
5.3.3. Fiber noise cancellation . . . . .	50
5.3.4. Wooden shielding box . . . . .	52
5.3.5. Setup for an optical beat with the QSIM Ti:Sa laser at UIBK . . . . .	52
5.3.6. The three-cornered hat measurement setup at UIBK . . . . .	53
5.3.7. Connections to other setups at UIBK . . . . .	53
5.4. Historical Development of the Setup . . . . .	56
5.4.1. Experimental setup at IQOQI Innsbruck . . . . .	57

## Contents

5.4.2. Moving the setup to UIBK . . . . .	58
<b>6. Results at IQOQI</b>	<b>60</b>
6.1. Laser Linewidth Measurement at IQOQI . . . . .	60
6.1.1. Beat measurement with QSIM at IQOQI . . . . .	60
6.1.2. Discussion of the beat result at IQOQI . . . . .	62
6.2. Laser Linewidth Broadening from Intensity Fluctuations . . . . .	63
6.2.1. Controlled intensity changes in the reference cavity light field . . . . .	64
6.2.2. Intensity fluctuations of the three lasers . . . . .	66
<b>7. Results at UIBK</b>	<b>69</b>
7.1. Intensity Stabilization Performance . . . . .	69
7.2. Fiber Noise Cancellation Performance . . . . .	71
7.3. Frequency Stability of the new Ti:Sa laser at UIBK . . . . .	73
7.3.1. Beat measurement with QSIM at UIBK . . . . .	74
7.3.2. Subsequent changes to the experimental setup . . . . .	75
7.3.3. Three-cornered hat measurement . . . . .	77
7.3.4. Frequency drift of the new Ti:Sa laser . . . . .	78
7.4. Ramsey Experiments on a Single Ion . . . . .	82
7.5. Towards a sub-10 Hz Linewidth . . . . .	86
<b>8. Conclusion and Outlook</b>	<b>90</b>
<b>A. Step-by-step Derivation of the PDH Error Signal</b>	<b>92</b>
<b>B. Analysis of the PDH Error Signal at UIBK</b>	<b>96</b>
<b>C. Proposing a Way to Optimize FALC Parameters in the PDH Lock</b>	<b>98</b>
<b>D. Simulation of a Controller's Response to a Step Disturbance</b>	<b>100</b>

# 1. Introduction

Information must be encoded into a physical system [1]. The laws that describe physical systems are the same laws that determine what can be done with information that is encoded into them. The modern world relies heavily on classical information. *Bits*, the fundamental unit of classical information, are encoded into systems that are well described by the laws of classical physics. In analogy and demarcation to a classical bit, a *qubit* is the fundamental unit of quantum information. The laws of quantum mechanics are different from the laws of classical physics and change fundamentally what can be done with the encoded information. Since the advent of quantum physics in the early 20th century, major progress in theory and experiments has led to a point where it is now possible to develop and use new technology that employs individual quantum objects in which quantum information can be encoded. Such technology is seen as a natural progression as the scale at which we engineer physical systems reduces, and realizing this, scientists have ambitions to create new computers, networks and sensors. The theoretical and experimental developments that contribute to our understanding of and applications for quantum information are summarized in the field of *quantum information science*.

The field can be split into four main subfields: quantum computers, quantum simulations, quantum communication and quantum metrology. In the center of focus is a quantum information processor, the *quantum computer* [2]. In 1982, David Deutsch found a computational problem that can be solved with fewer computational steps using a quantum computer rather than a classical computer [3], showing the theoretical capabilities of a quantum information processor. This problem was later generalized to what is today known as the *Deutsch-Josza algorithm* [4]. The breakthrough that sparked interest in quantum computers globally was *Shor's algorithm* in 1994 [5], a quantum algorithm that allows the prime factors of integers to be found faster than any algorithm for a classical computer is known to be able to. Since then, additional algorithms like the *Grover algorithm* [6] for searching an element in an unsorted list were discovered, and the goal of building a quantum machine that surpasses any classical computation capability has fascinated and has driven the work of many scientists ever since. The key requirements for a quantum computer were stated in 2001 by David P. DiVincenzo [7]: A quantum computer needs a scalable system with well-defined qubits, a way to initialize qubits in a low-entropy fiducial quantum state, a universal gate set (set of operations on the qubit), a possibility to read out single qubits individually and coherence times that are significantly longer than any calculation step that is performed. As of 2022, the most advanced quantum information processors employ between 20 and 50 qubits [8, 9]. A quantum information processor can also be used for *quantum simulations*. Richard Feynman first discussed the far-reaching capabilities of quantum simulators in a 1981 lecture [10]. Simulating a quantum system with classical computers sets the limit of feasibility to approximately 50 interacting qubits. Feynman's proposal was to use controllable quantum systems in order to simulate quantum behavior. One can differentiate between two types of quantum simulators. A *digital quantum simulator* simulates an arbitrary system by employing an algorithm running on a quantum computer, much like a quantum Turing machine. However, the creation of a digital simulator seems a far-away goal for now. The other type is an *analog quantum simulator* that directly reproduces the states and dynamics of specific

## 1. Introduction

physical problems. Some analog simulators are attainable with today's quantum technology [11].

Another important subfield of quantum information science is *quantum communication*. The long-term goal is to create a *quantum internet* [12] in analogy to the classical internet that connects processors of information around the globe. The connection between quantum processors that are separated by kilometers could be faithfully established with *quantum repeaters* [13] that are at the focus of ongoing research [14]. Quantum communication is also of relevance as distributed quantum computing is seen as a way to overcome principle limitations of quantum computer scalability [15]. Finally, an important part of quantum communication is *quantum cryptography* that would allow for the fundamentally secure transmission of information between two parties without an eavesdropper being able to intercept the communication undetected. Historical proposals for quantum cryptography schemes include most notably the *BB84 protocol* [16] and the *E91 protocol* [17], while research on quantum cryptography is still ongoing today [18].

The last subfield in quantum information science that is here presented is *quantum metrology*. The laws of quantum mechanics allow for measurements whose uncertainties are in theory only limited by the *Heisenberg limit* that arises from the fundamental complementarity [19] of nature [20]. Quantum metrology aims to develop measurements with a precision and accuracy that cannot be attained with classical measuring devices.

Coming back to the first sentence in the introduction: information must be encoded into a physical system. Every application in quantum information science needs a physical platform in which qubits can be encoded and manipulated. Since the beginning of quantum information science, a variety of candidate platforms from the most disparate fields of physics have emerged, including photons [21], neutral atoms [22], ionized atoms [23], superconducting circuits [24] and solid state spins such as quantum dots and nitrogen-vacancy (NV) centers [25]. One of the most successful platforms for encoding and manipulating qubits are trapped ionized atoms, usually referred to as *trapped ions*. Building a quantum computer from trapped ions was first proposed by Peter Zoller and Ignacio Cirac at the University of Innsbruck in 1995 [26]. In the subsequent years, research groups e.g., around Rainer Blatt and David J. Wineland experimentally realized the key steps that the theoretical proposal requires for an ion-trap quantum computer [27, 28].

The ionic species  $^{40}\text{Ca}^+$  has emerged as one of the prime candidates for quantum information science experiments [29, 30]. The qubit is encoded into two energy levels within the ion's fine structure manifolds. Specifically, one approach is to encode one logical state inside the ground state manifold  $4^2\text{S}_{J=1/2}$  and the other logical state inside the excited state manifold  $3^2\text{D}_{J=5/2}$ . Lasers can be used to manipulate the ion-qubit in the quantum processor. The qubit transition from  $4^2\text{S}_{J=1/2}$  to  $3^2\text{D}_{J=5/2}$  requires a laser that emits light at a wavelength of 729 nm. The excited state has a lifetime of 1.17 s [31], setting the maximum coherence time of the qubit. A lifetime of 1.17 s means that the excited state of the qubit has a natural *linewidth* on the order of 1 Hz. It is therefore desirable for the laser that manipulates the qubit transition to have a linewidth that is less or equal than 1 Hz, such that the laser is not the limit to the qubit's coherence time. To achieve this specification for the laser, a feedback loop can be implemented that stabilizes the laser frequency to an isolated optical reference cavity. A laser linewidth of 1 Hz and below can be obtained by the *Pound-Drever-Hall (PDH) locking technique* [32] that was first proposed in 1983. The PDH technique builds on the 1946 work from Robert Pound on microwave stabilizers [33].

This master thesis presents the frequency stabilization of a Titanium-Doped Sapphire (Ti:Sa) laser at 729 nm to an optical reference cavity using the PDH technique. The stabilization was done to prepare the laser to be used in quantum information science experiments with

## 1. Introduction

trapped  $^{40}\text{Ca}^+$  ions. The laser system will be used by three research teams at the University of Innsbruck. The first team, in which I am doing my Master's thesis, is known as the "Quantum Frequency Conversion" (QFC) team, led by Ben Lanyon, whose work lies in the field of quantum communication. The second team, known as the "2D Crystals" team, is led by Christian Roos and works on quantum simulations. The third team is the "Quantum Molecules" team, led by Philipp Schindler, who will work on quantum computing with polyatomic molecules.

The outline of the thesis is as follows: Chapter 2 presents a theoretical introduction to quantum information science with trapped ions. Specifically, after first recalling the relevant aspects of quantum mechanics and light-particle interaction, the methods for encoding and manipulating qubits in trapped  $^{40}\text{Ca}^+$  ions are summarized. Chapter 3 deals with lasers and their properties. That chapter includes three parts. In the first part, the principles of laser theory are summarized. In the second part, the concept of the laser linewidth and means to measure the laser linewidth are given. In the third part, a generic description of the Ti:Sa Laser is given. Chapter 4 presents an overview of the PDH technique. That chapter starts off with a general introduction to control theory and PID control. Afterwards, an optical cavity as a frequency reference is introduced. Finally, the PDH technique is motivated, summarized and the error signal is derived. Chapter 5 presents the experimental setup. The two main constituents of the experimental setup, our new Ti:Sa laser and the optical reference cavity, are first presented. A description of the optical and electronic setup that is needed to implement the PDH technique and to measure the linewidth of the new Ti:Sa laser follows. Next, the optical setups of two other lasers that are locked to the same optical reference cavity are presented. A final section in Chapter 5 describes the differences in the experimental setup between the two laboratories in which it was developed, as well as the move between them. Chapters 6 and 7 present the experimental results of the master project. In Chapter 6, the measurement results that were obtained at the Institute of Quantum Optics and Quantum Information (IQOQI) in Innsbruck are presented. Those results include a linewidth estimated from a beat measurement and the effect of laser intensity fluctuations on the optical reference cavity frequency. In Chapter 7, the measurement results that were obtained in a new laboratory at the University of Innsbruck (UIBK) are presented and discussed. The results include an assessment of the fiber noise cancellation and intensity stabilization performance. Moreover, the results of further beat measurements are presented. The obtained linewidth was compared with the measured linewidth through Ramsey experiments on a single ion. In a final section the path towards a sub-10 Hz linewidth is presented. The thesis ends with a conclusion and outlook in Chapter 8.

# 2. Quantum Information Science with Trapped Ions

As described in the introduction, the field of quantum information science gives rise to a variety of applications that differ from their classical counterparts. One physical system that allows for encoding and manipulation of the fundamental unit of quantum information, the qubit, are trapped ions. The species  $^{40}\text{Ca}^+$  has emerged as one of the most successful platforms for quantum information science experiments.

Section 2.1 presents the foundations of quantum mechanics. After the foundations follows an algebraic description of qubits and how they can be manipulated. Section 2.2 begins with the theory behind the interaction of a laser and an ion, in the quadrupole approximation. Next, it is summarized how the different electronic transitions inside the ion are used in experiments in our team. Finally, it is shown how a universal gate set can be performed on  $^{40}\text{Ca}^+$ .

## 2.1. Quantum Mechanics and Qubits

### The postulates of quantum mechanics and consequences

Quantum mechanics gives a framework for the development of theories in physics [34]. Quantum mechanics is based on four postulates. Those postulates, paraphrased from [34], and immediate consequences are summarized in the following paragraphs.

1. A quantum mechanical system is described by its *state*. This state  $|\psi\rangle$  is a unit vector in a Hilbert space  $\mathcal{H}$ : A complex vector space with inner product.

The state vector, also called the *ket* vector, can be expressed as a linear combination or *superposition* of a set of vectors  $|u_i\rangle$  that form an orthonormal basis in  $\mathcal{H}$ ,

$$|\psi\rangle = \sum_i c_i |u_i\rangle \quad (2.1)$$

where  $c_i \in \mathbb{C}$  denote the vector components. Furthermore, there exists a dual Hilbert space  $\mathcal{H}^*$ , whose elements are linear functionals  $\langle\phi|$  or *bra* vectors that assign a complex number  $\langle\phi|\psi\rangle$  to every  $|\psi\rangle$  [35]. The bra vector is constructed by transposing and complex conjugating its corresponding ket.

2. The time evolution of a state is described by a *unitary transformation*. A state  $|\psi\rangle$  at one point in time is connected to  $|\psi'\rangle$  at another point in time via

$$|\psi'\rangle = \hat{U} |\psi\rangle, \quad (2.2)$$

where  $\hat{U}$  is a unitary operator.

## 2. Quantum Information Science with Trapped Ions

The state's continuous-time evolution in  $t$  is described by the *Schrödinger equation*

$$i\hbar \frac{d}{dt} |\psi\rangle = \hat{H} |\psi\rangle. \quad (2.3)$$

The number  $i$  is here the complex unit,  $\hbar$  the reduced Planck constant  $h/(2\pi)$  and  $\hat{H}$  the Hamiltonian of the system. Unitary evolution requires that the norm of the quantum state is conserved over time and that the temporal evolution of a quantum state is a reversible process.

3. Measurements in quantum mechanics are described by *measurement operators*  $\{\hat{M}_m\}$ , where the index indicates the measurement outcome  $m$ . If a quantum mechanical system is in the state  $|\psi\rangle$  right before the measurement, the probability of outcome  $m$  occurring, corresponding to operator  $\hat{M}_m$ , is

$$p_m = \langle \psi | \hat{M}_m^\dagger \hat{M}_m | \psi \rangle \quad (2.4)$$

and the state of the system right after the measurement is

$$|\psi'_m\rangle = \frac{\hat{M}_m |\psi\rangle}{\sqrt{p_m}}. \quad (2.5)$$

The operation of Eq. (2.5) is irreversible and is known as the *collapse of the wave function*. In the special case of *projective measurements*, the measurement operators  $\hat{M}_m$  are orthogonal projectors that fulfill the identity

$$\hat{M}_m \hat{M}_{m'} = \delta_{m m'} \hat{M}_m \quad (2.6)$$

where  $\delta$  is the Kronecker delta. In this case, the sum

$$\hat{A} = \sum_m m \hat{M}_m \quad (2.7)$$

is called an *observable*. The observable  $\hat{A}$  is a hermitian operator [35], and the real numbers  $m$ , the measurement outcomes, are the eigenvalues of the operator. The Hamiltonian in Eq. (2.3) is one such example of an observable.

4. The state space of the composite system is the tensor product  $\otimes$  of the state spaces of the component systems.

As a consequence of this postulate, the dimension of the composite system's state space is the product of the dimensions of the component systems' state spaces. If the state of a composite system,  $|\psi\rangle \in \mathcal{H} = \otimes_i \mathcal{H}_i$ , can be written as

$$|\psi\rangle = \bigotimes_i |\psi_i\rangle \quad (2.8)$$

with  $|\psi_i\rangle \in \mathcal{H}_i$ , then the state  $|\psi\rangle$  is said to be a *product state*. If, however,  $|\psi\rangle$  cannot be written in this form,

$$|\psi\rangle \neq \bigotimes_i |\psi_i\rangle, \quad (2.9)$$

then the state is said to be *entangled*. Entanglement, as will be touched upon later, plays a central role in quantum information processing. It is regarded as a resource that fuels the advantages that quantum technologies have over their classical counterparts [36]. In a broader context, entanglement has been studied for decades, as it gives an insight into the properties of nature and physical reality [37, 38].

### Qubits and qubit operations

The simplest nontrivial system in quantum mechanics consists of a state in a two-dimensional Hilbert space  $\mathcal{H}_2$ . One orthonormal basis that can be found in  $\mathcal{H}_2$  — the so-called “logical basis” — is formed by the basis vectors

$$|0\rangle = \begin{bmatrix} 1 \\ 0 \end{bmatrix}, \quad |1\rangle = \begin{bmatrix} 0 \\ 1 \end{bmatrix}. \quad (2.10)$$

An arbitrary state in  $\mathcal{H}_2$  can be expressed as

$$|\psi\rangle = a|0\rangle + b|1\rangle \quad (2.11)$$

with  $a, b \in \mathbb{C}$ . This state  $|\psi\rangle$  is called a *qubit* in analogy to a classical bit. Combining the ket with its corresponding bra yields the number

$$\langle\psi|\psi\rangle = \langle\psi|\left(\sum_{n=0,1} |n\rangle\langle n|\right)|\psi\rangle = |a|^2 + |b|^2. \quad (2.12)$$

Here,  $|a|^2$  is the probability  $p_0$  of finding the qubit in the state  $|0\rangle$  after a measurement ( $\hat{M}_0 = |0\rangle\langle 0|$  being the measurement operator, an orthogonal projector) and  $|b|^2$  is the probability  $p_1$  of finding the qubit in  $|1\rangle$  (measurement operator  $\hat{M}_1 = |1\rangle\langle 1|$ , also an orthogonal projector). A necessary condition for probabilities is that  $p_0 + p_1 = |a|^2 + |b|^2 = 1$ , constraining  $|\psi\rangle$  to be a unit vector at all times.

A qubit state can also be written in spherical coordinates as

$$|\psi\rangle = \left( \cos\left(\frac{\theta}{2}\right)|0\rangle + e^{i\phi}\sin\left(\frac{\theta}{2}\right)|1\rangle \right) \cdot e^{i\gamma} \quad (2.13)$$

where  $\theta$  is the polar angle and  $\phi$  is the azimuthal angle. The term  $e^{i\gamma}$  is a global phase factor that has no observable relevance. The term  $e^{i\phi}$  is denoted the relative phase factor, and  $\phi$  is the *relative phase*. This description allows an arbitrary qubit state to be displayed as a vector on a sphere, known as the *Bloch sphere*. A portrayal of the qubit state on the Bloch sphere can be seen in Figure 2.1. The Bloch sphere shows that it is natural to introduce two additional orthonormal bases in which a qubit can be represented. For an equal superposition between  $|0\rangle$  and  $|1\rangle$  and relative phase factors  $e^{i\phi} = \pm 1$  or  $e^{i\phi} = \pm i$ , two orthonormal bases lie in the equatorial plane of the Bloch sphere. Their corresponding basis vectors read

$$|+\rangle = \frac{1}{\sqrt{2}}(|0\rangle + |1\rangle), \quad |-\rangle = \frac{1}{\sqrt{2}}(|0\rangle - |1\rangle) \quad (2.14)$$

and

$$|i\rangle = \frac{1}{\sqrt{2}}(|0\rangle + i|1\rangle), \quad |-i\rangle = \frac{1}{\sqrt{2}}(|0\rangle - i|1\rangle). \quad (2.15)$$

The second postulate states that the evolution of quantum states is described by unitary operators. Applying unitaries to a qubit leads to rotations of  $|\psi\rangle$  to other points on the surface of the Bloch sphere around axes that intersect the origin. Three unitary operators, known as the *Pauli operators*, are given by

$$\begin{aligned} \hat{\sigma}_z &= |0\rangle\langle 0| - |1\rangle\langle 1|, \\ \hat{\sigma}_x &= |+\rangle\langle +| - |-\rangle\langle -|, \\ \hat{\sigma}_y &= |i\rangle\langle i| - |-i\rangle\langle -i|. \end{aligned} \quad (2.16)$$

The first of the three Pauli operators causes a rotation by an angle  $\pi$  on the sphere around an axis that is spanned by the basis vectors  $\{|0\rangle, |1\rangle\}$ , the second a rotation of  $\pi$  around  $\{|+\rangle, |-\rangle\}$  and the third around  $\{|i\rangle, |-i\rangle\}$ . These axes are also denoted the z-axis, the x-axis and the y-axis, respectively. Another useful operator, known as the *Hadamard gate*, leads to a  $\pi/2$  rotation around the y-axis, that is a change from  $|0\rangle$  to  $|+\rangle$ :

$$\hat{H}_{\text{ad}} = |+\rangle\langle 0| + |-\rangle\langle 1|. \quad (2.17)$$

The set of possible 2 by 2 unitaries with determinant +1 that describe all possible rotations on the Bloch sphere is called  $\text{SU}(2)$ . One way to describe an arbitrary element of  $\text{SU}(2)$  is to use a sequence of at most three rotations out of [39]

$$\begin{aligned} \hat{R}_{x,y}(\theta_1, \phi_1) &= \exp\left(-i\theta_1(\cos(\phi_1)\hat{\sigma}_x + \sin(\phi_1)\hat{\sigma}_y)/2\right), \\ \hat{R}_z(\theta_1) &= \exp\left(-i\theta_1\hat{\sigma}_z/2\right), \end{aligned} \quad (2.18)$$

where  $\theta_1, \phi_1 \in \mathbb{R}$ . Out of the continuum of possible rotations on the Bloch sphere, one prominent representative should be additionally mentioned, the so-called  $\pi/8$  operator

$$\hat{T} = |0\rangle\langle 0| + e^{i\pi/4}|1\rangle\langle 1|. \quad (2.19)$$

The Hilbert space dimension of  $n$  qubits scales with  $2^n$  according to the fourth postulate. So for  $n = 2$ , the Hilbert space in question is  $\mathcal{H}_4$ . There are unitaries that operate on two qubits that are capable of generating entanglement, most notably the *controlled-NOT* or *CNOT* gate

$$\hat{C}(\hat{\sigma}_x) = \mathbb{I}_2 \otimes |0\rangle\langle 0| + \hat{\sigma}_x \otimes |1\rangle\langle 1| \quad (2.20)$$

where  $\mathbb{I}_2$  is the 2 by 2 identity matrix. Applying this gate to the two-qubit state  $|+\rangle \otimes |0\rangle = |+, 0\rangle$  yields an entangled state, one of the four *Bell states* that together form a basis in  $\mathcal{H}_4$ . A further discussion on Bell states and on a graphical representation of operators applied to states (quantum circuits) can be found in detail in [34].

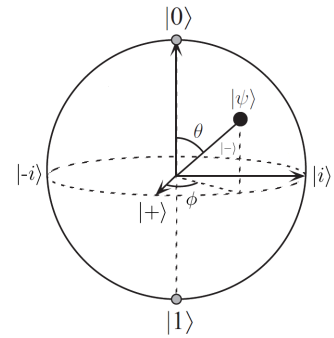


**Figure 2.1.:**  
**The Bloch sphere.**  
Representation of  $|\psi\rangle$  as a projection on the surface of the Bloch-Sphere. The state  $|0\rangle$  is set on the north pole while  $|1\rangle$  is located at the south pole. The states  $\{|+\rangle, |-\rangle\}$  and  $\{|i\rangle, |-i\rangle\}$  can be found on the equatorial plane. The angle  $\phi$  denotes the azimuthal angle and  $\theta$  the polar angle.

Encoding qubits in physical systems and manipulating them is the foundation of all applications in the field of quantum information science, be it in quantum computation, simulation, communication or metrology. Manipulation of qubits here means unitary evolution. A set of unitary operators or *gates* that can be duplicated and reconfigured to realize arbitrary unitaries is called a *universal gate set*. A universal quantum computer should be able to implement any arbitrary evolution of qubits, so that it can implement any algorithm. In [34] it is proven that one possible universal set of operations, the *standard set of universal gates*, consists of  $\hat{T}$ ,  $\hat{H}_{\text{ad}}$  and  $\hat{C}(\hat{\sigma}_x)$ . Another gate set that is used in experiments on trapped ions consists of single qubit operations that create the rotations in Eq. (2.18) and the *Mølmer-Sørensen gate*, which will be further explained in Subsection 2.2.3.

## 2.2. Encoding and Manipulating Qubits in Trapped $^{40}\text{Ca}^+$

In their paper from 1995 [26], Ignacio Cirac and Peter Zoller proposed to encode a qubit into the ground state and one excited state of an ion. Unitary operations are performed by applying laser light to the ions and the two-qubit entangling gate is established by additionally coupling two ions over their shared quantized harmonic motion.

In order to work with ions in quantum information science, the particles are isolated from the environment in an ion trap. Due to *Gauss's law* and the consequential *Earnshaw theorem*, it is not possible to trap ions with static electric fields. One powerful way to trap individual ions is by using alternating electric quadrupole fields in a design called the *Paul trap*, which was invented by Wolfgang Paul in 1989 [40]. Paul traps are not directly relevant for understanding the experimental results of this thesis, therefore Paul traps will not be touched upon further. For extended reading on Paul traps the reader is referred to [41].

As previously stated, trapped  $^{40}\text{Ca}^+$  ions have become prime candidates for platforms into which qubits can be encoded. The element calcium (Ca) can be found in the second group of the periodic table and so  $^{40}\text{Ca}^+$  ion has one valence electron. A schematic of the energy levels of the single outer valence electron in  $^{40}\text{Ca}^+$  that are relevant to this thesis is shown in Figure 2.2. Due to the Zeeman effect, the energy levels shown in Figure 2.2 split further into sublevels when an external magnetic field is applied to the ion. As  $^{40}\text{Ca}$  has no nuclear spin ( $I = 0$ ), the energy level structure shows no hyperfine splitting. In the case of  $^{40}\text{Ca}^+$ , one successful choice of encoding a qubit is by denoting one Zeeman state of the ground state manifold  $4^2\text{S}_{1/2}$  as the lower qubit level  $|1\rangle$  and one Zeeman state of the excited state manifold  $3^2\text{D}_{5/2}$  as the upper qubit level  $|0\rangle$ . Laser light at a wavelength of 729 nm couples the  $|0\rangle$  and  $|1\rangle$  states of the qubit on an electric quadrupole transition. The ground state is typically denoted  $|1\rangle$ : As a discussion about the measurement procedure will show, the state  $|1\rangle$  can be identified through a bright fluorescing ion in this case, while  $|0\rangle$  is identified through no signal, a “dark ion”. In the following subsections, the physics behind the manipulation of qubits that are encoded in trapped  $^{40}\text{Ca}^+$  is described more rigorously.

### 2.2.1. Laser-ion interaction in the quadrupole approximation

The ion can change its internal electronic state when energy is applied or removed. This energy can be given to the ion in the form of radiation. The Hamiltonian that describes the interaction of radiation with a particle is [42]

$$\hat{H} = \hat{H}_{\text{part}} + \hat{H}_{\text{rad}} + \hat{H}_{\text{int}}. \quad (2.21)$$

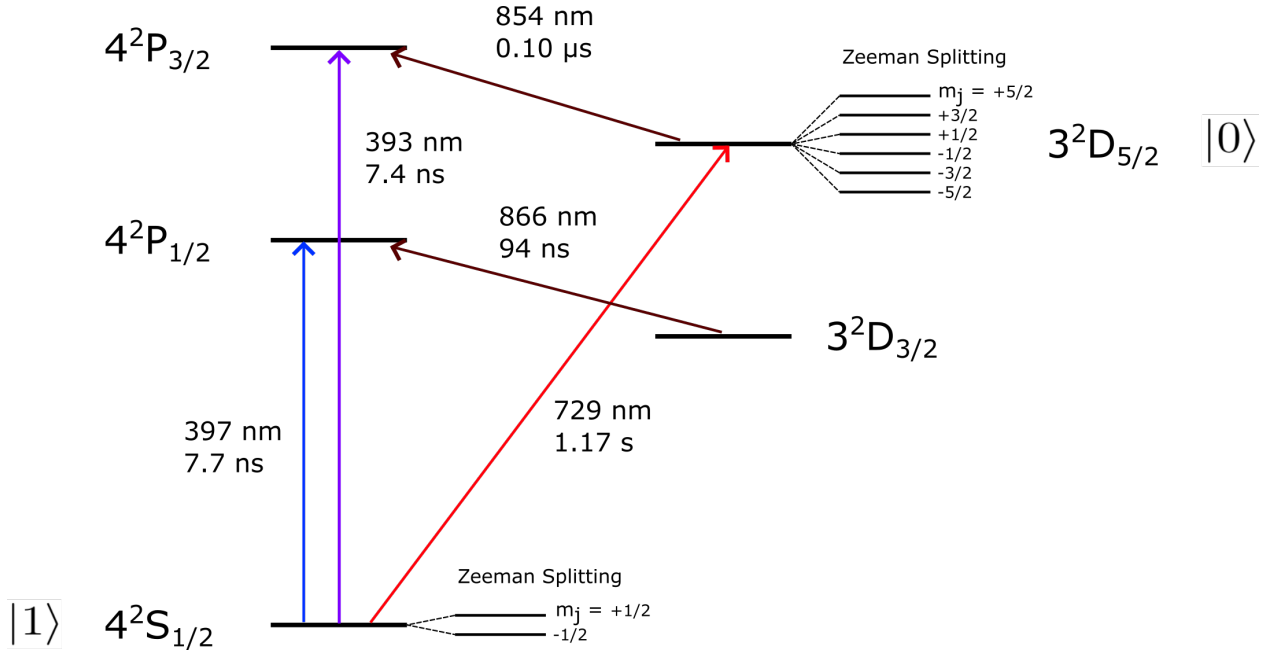


**Figure 2.2.: Reduced energy level scheme of the  $^{40}\text{Ca}^+$  ion.** The transitions between states are depicted as arrows. Next to the arrows, the transition wavelength and the natural lifetime of the excited state are shown. The transition at 729 nm between the  $4^2\text{S}_{1/2}$  and  $3^2\text{D}_{5/2}$  manifolds is an electric quadrupole transition, with an excited lifetime of 1.17 s [31]. A magnetic field further splits the energy levels into different Zeeman levels. The Zeeman splitting is shown for the  $4^2\text{S}_{1/2}$  and  $3^2\text{D}_{5/2}$  manifolds, and the logical  $|1\rangle$  and  $|0\rangle$  states of a qubit are typically encoded in individual Zeeman sub-levels within these manifolds, respectively. The isotope  $^{40}\text{Ca}$  has no nuclear spin, so  $^{40}\text{Ca}^+$  has no hyperfine structure.

The term  $\hat{H}_{\text{part}}$  is called the particle Hamiltonian, containing the kinetic and potential energy of the particle (e.g., an ion). The second term  $\hat{H}_{\text{rad}}$  includes the energy of the radiation (e.g., laser light), and the last term  $\hat{H}_{\text{int}}$  is the interaction Hamiltonian that describes the interaction between radiation and the particle. In the upcoming paragraphs, phenomena that arise as a consequence of radiation-particle interaction are derived and discussed. First, the interaction Hamiltonian in the quadrupole approximation is derived, starting from classical electrostatics.

In classical electrostatics, a charge distribution  $\rho(\vec{r})$  in a scalar electric potential  $\phi(\vec{r})$ , where  $\vec{r}$  is position, yields an electrostatic energy [43, 44]

$$H = \int \rho(\vec{r})\phi(\vec{r})d^3r. \quad (2.22)$$

Taking a Taylor expansion of  $\phi(\vec{r})$  around  $\vec{r} = 0$  up to second order yields

$$\phi(\vec{r}) = \phi(0) + \sum_i r_i \frac{\partial}{\partial r_i} \phi(0) + \frac{1}{2} \sum_i \sum_j r_i r_j \frac{\partial^2}{\partial r_i \partial r_j} \phi(0). \quad (2.23)$$

In this equation, the indices  $i$  and  $j$  run from 1 to 3. The scalars  $r_1$ ,  $r_2$  and  $r_3$  are the components of the position vector  $\vec{r}$ . Using that the electric field is the negative gradient of the electric potential ( $\vec{E} = -\nabla\phi$ ) and that there are no free charges in the environment ( $\nabla \cdot \vec{E} = 0$ ), the previous equation can be rewritten as

## 2. Quantum Information Science with Trapped Ions

$$\phi(\vec{r}) = \phi(0) - \vec{r} \cdot \vec{E}(0) - \frac{1}{6} \sum_i \sum_j (3r_i r_j - r^2 \delta_{ij}) \frac{\partial}{\partial r_i} E_j(0) \quad (2.24)$$

where  $\delta_{ij}$  is the Kronecker delta.

By plugging this expression for the scalar potential back into Eq. (2.22), the electrostatic energy can be expressed as

$$H = q \cdot \phi(0) - \vec{p} \cdot \vec{E}(0) - \frac{1}{6} \sum_i \sum_j Q_{ij} \frac{\partial}{\partial r_i} E_j(0). \quad (2.25)$$

Here,  $q = \int \rho(\vec{r}) d^3r$  is the total electric charge,  $\vec{p} = \int \vec{r} \cdot \rho(\vec{r}) d^3r$  is the *electric dipole moment* of  $\rho(\vec{r})$  and  $Q_{ij} = \int (3r_i r_j - r^2 \delta_{ij}) \rho(\vec{r}) d^3r$  is the *electric quadrupole moment* of  $\rho(\vec{r})$ . It is clear that the charge distribution's electric dipole couples to the electric field, while the charge distribution's electric quadrupole couples to the gradient of the electric field.

The  $^{40}\text{Ca}^+$  ion has a diameter in the regime of  $\sim 0.1$  nm, while the electric field of visible light has a wavelength in the regime of  $\sim 100$  nm. As a consequence, the ion sees a slow spatial variation of the external electric field and the coupling of the ion's multipole moments to the external electric field becomes significantly weaker with increasing multipole orders. Therefore, it is justified to use the Taylor expansion up to second order in Eq. (2.23) when describing visible light interacting with a  $^{40}\text{Ca}^+$  ion, only regarding the interaction of light with the ion's dipole and quadrupole moments.

In a semiclassical description of ion-light interaction, the electrostatic energy in Eq. (2.25) can be quantized to the interaction Hamiltonian in Eq. (2.21),

$$\begin{aligned} \hat{H}_{\text{int}} &= \hat{H}_{\text{stat}} + \hat{H}_{\text{dip}} + \hat{H}_{\text{quad}} \\ &= \hat{q} \cdot \phi(0) - \hat{\vec{p}} \cdot \vec{E}(0) - \frac{1}{6} \sum_i \sum_j \hat{Q}_{ij} \frac{\partial}{\partial r_i} E_j(0). \end{aligned} \quad (2.26)$$

The first term is just an electrostatic energy as the ion's charge rests at an electric potential  $\phi(0)$ . The second term is the electric dipole Hamiltonian and the third term the electric quadrupole Hamiltonian. Now, the consequences that follow from the interaction Hamiltonian in Eq. (2.26) for the outer valence electron's occupation probability of different states in  $^{40}\text{Ca}^+$  will be discussed.

### Transition matrix elements

The transition matrix element is a measure of the coupling strength between two states in a particle. For a two-level particle, the first term in equation Eq. (2.21) can be written as

$$\hat{H}_{\text{part}} = E_g |g\rangle \langle g| + E_e |e\rangle \langle e|, \quad (2.27)$$

where  $|g\rangle$  is the particle's ground state,  $|e\rangle$  the excited state and  $E_g$  and  $E_e$  the corresponding states' energies. The energy difference is  $E_e - E_g = \hbar\omega_0$ , where the variable  $\omega_0$  is the transition resonance frequency.

For a charge of value  $q$ , the *dipole transition matrix element* between the state  $|g\rangle$  and  $|e\rangle$  is given by [45]

$$\vec{M}_{\text{ge,dip}} = \langle g | \vec{\hat{p}} | e \rangle = q \langle g | \vec{\hat{r}} | e \rangle \quad (2.28)$$

## 2. Quantum Information Science with Trapped Ions

where  $\vec{p}$  is the dipole operator and  $\vec{r}$  is the position operator. The position operator is a continuous linear operator that is defined as [35]

$$\vec{r}|\psi\rangle = \int |\vec{r}\rangle \vec{r} \langle \vec{r}|\psi\rangle d\vec{r} = \int \psi(\vec{r})\vec{r}|\vec{r}\rangle d\vec{r}. \quad (2.29)$$

In this equation,  $\vec{r} \in \mathbb{R}^3$  and  $\psi(\vec{r}) = \langle \vec{r}|\psi\rangle$  is the wavefunction in position space. The *quadrupole transition matrix element* is

$$M_{\text{ge,quad}_{ij}} = \langle g|\hat{Q}_{ij}|e\rangle = q \langle g|3\hat{r}_i\hat{r}_j|e\rangle - q \langle g|\hat{r}^2\delta_{ij}|e\rangle. \quad (2.30)$$

The position operator is further a multiplication operator with negative parity. The parity of the wave functions  $\langle \vec{r}|g\rangle$  and  $\langle \vec{r}|e\rangle$  depends on the orbital angular momentum quantum number  $L$  of the states  $|g\rangle$  and  $|e\rangle$ . If  $L$  is an even number, the parity is positive, if  $L$  is an odd number, the parity is negative. An integral over  $d\vec{r}$  of a function with negative parity is 0. Therefore, the following two statements can be made. First, for a dipole transition, the transition matrix element is 0 if both wave functions have the same parity. For a quadrupole transition, the position operator appears twice in each term of the matrix element, making the product of positive parity. So the second statement is that the quadrupole transition element is 0 if the wavefunctions have a different parity. Looking at the reduced level scheme of  $^{40}\text{Ca}^+$  in Figure 2.2 again, it becomes apparent that all shown transitions are dipole transitions except for  $4^2\text{S}_{1/2}$  to  $3^2\text{D}_{5/2}$ . It follows that the qubit transition between  $|0\rangle$  and  $|1\rangle$  is a quadrupole transition.

### Rabi frequency

Here, a short derivation of the Rabi frequency — quantifying the rate at which an external drive field (e.g., laser light) causes the electron state to change in an atom — is given. The Hamiltonian  $\hat{H}_{\text{rad}}$  in Eq. (2.21), that describes the energy of the interacting laser light, can be written as [42]

$$\begin{aligned} \hat{H}_{\text{rad}} &= \frac{\epsilon_0}{2} \int \left( \vec{E}^2(\vec{r}) + c^2 \vec{B}^2(\vec{r}) \right) d\vec{r}, \text{ or} \\ \hat{H}_{\text{rad}} &= \sum_k \hbar\omega_k (\hat{a}_k^\dagger \hat{a}_k + \frac{1}{2}). \end{aligned} \quad (2.31)$$

What term to use in the above equation array depends on whether one chooses a semiclassical approach (first line) to describe the laser-ion interaction or an approach that includes the second quantization (second line). In the first equation,  $\epsilon_0$  is the electric field constant,  $\vec{B}$  is the magnetic field and  $c$  the speed of light in vacuum. In a quantized model, light is described as a sum of harmonic oscillators. Here,  $\omega_k$  denotes the light frequency of mode  $k$ , and the operators  $\hat{a}_k^\dagger$  and  $\hat{a}_k$  correspond to creation and annihilation operators of a photon in mode  $k$ , respectively.

It suffices to describe laser light interacting with a single ion semiclassically: The laser light is seen as a reservoir, and the state of the reservoir changes negligibly under the influence of coupling to the particles [42]. The time-dependent electric field used in the description of the laser-ion interaction in the following discussion (the ion is situated at  $\vec{r} = 0$ ) is given by

$$\vec{E}(t) = \vec{E}_0 \cos(\omega t + \phi_1), \quad (2.32)$$

## 2. Quantum Information Science with Trapped Ions

where  $\vec{E}_0$  is the field amplitude,  $\omega$  the light frequency,  $t$  time and  $\phi_1$  an arbitrary phase that is set to 0 in the following discussion.

Consider again the particle described in Eq. (2.27), where the two states are e.g., two energy levels the outer valence electron of an ion can occupy. In the electric dipole approximation, the coupling between the ground state  $|g\rangle$  and the excited state  $|e\rangle$  is given by the interaction of the electric dipole operator  $\vec{p}$  of the particle and an external electric field. An external time-dependent electric field of the type Eq. (2.32) allows the electron to switch between the coupled states  $|g\rangle$  and  $|e\rangle$ . The dipole interaction Hamiltonian in Eq. (2.26),

$$\hat{H}_{\text{dip}} = -\vec{p} \cdot \vec{E}(t), \quad (2.33)$$

can be seen as a time-dependent perturbation to the particle in addition to the stationary particle Hamiltonian  $\hat{H}_{\text{part}}$ . Therefore, the time evolution of the system can be described by the Schrödinger equation

$$i\hbar \frac{d}{dt} |\psi(t)\rangle = (\hat{H}_{\text{part}} + \hat{H}_{\text{dip}}) |\psi(t)\rangle. \quad (2.34)$$

The state

$$|\psi(t)\rangle = c_1(t) |g\rangle + c_2(t) |e\rangle \quad (2.35)$$

is a general solution of Eq. (2.34) and the component  $c_1(t)$  squared,

$$|c_1(t)|^2 = p_1(t) = |\langle g|\psi(t)\rangle|^2 \quad (2.36)$$

gives the probability  $p_1(t)$  to find the electron in the ground state. Multiplying Eq. (2.34) by  $\langle g|$  and, separately,  $\langle e|$  from the left side gives two coupled differential equations for  $c_1(t)$  and  $c_2(t)$  that can be combined to obtain [46]

$$\frac{d^2}{dt^2} c_1(t) = -\frac{1}{4\hbar^2} |\vec{M}_{\text{ge,dip}} \cdot \vec{E}_0|^2 c_1(t). \quad (2.37)$$

where  $\vec{M}_{\text{ge,dip}}$  is the dipole transition matrix element that was introduced in Eq. (2.28). In order to arrive at the equation above, the *rotating wave approximation* (that is commonly abbreviated as RWA) has to be made. Here, terms that include  $\exp(\pm i(\omega + \omega_0))$  are neglected, since for a near-resonant frequency of the light field,  $\omega \sim \omega_0$ , they oscillate so fast that they average to 0 when integrating over a large number of oscillations. With the initial conditions  $c_1(0) = 1$  (the electron is in the ground state before the electric field is applied) and  $\frac{d}{dt} c_1(0) = 0$ , the solution for the probability for finding the electron to be in the ground state is

$$p_1(t) = \cos^2 \left( \frac{|\vec{M}_{\text{ge,dip}} \cdot \vec{E}_0| t}{2\hbar} \right). \quad (2.38)$$

The frequency  $\Omega = |\vec{M}_{\text{ge,dip}} \cdot \vec{E}_0|/\hbar$  is called the *Rabi frequency* and is a measure for the coupling strength between the transition and the electric field. It is the frequency at which the electron's occupation probability changes between the two states, and at a time  $t = \pi/\Omega$  the electron changes from  $|g\rangle$  to  $|e\rangle$ .

An analogous derivation can be made for a quadrupole transition by using the interaction

## 2. Quantum Information Science with Trapped Ions

Hamiltonian  $\hat{H}_{\text{int}} = \hat{H}_{\text{quad}}$ . A calculation gives a Rabi frequency for a quadrupole transition of [39, 47],

$$\Omega = \frac{q|\vec{E}_0|}{2\hbar} \sqrt{\frac{15\Gamma c^2}{\omega^3 \alpha_0}} \Lambda g. \quad (2.39)$$

In this equation  $\alpha_0 \sim 1/137$  is the fine structure constant and  $\Gamma$  is the linewidth of the excited state, a quantity that will be discussed later. If a magnetic field leads to a Zeeman-splitting of the energy levels  $|g\rangle$  and  $|e\rangle$ , the *Clebsch-Gordan coefficient*  $\Lambda$  and the geometrical factor  $g$  account for corrections to the Rabi frequency.

### Natural lifetime and linewidth

Coupling between two discrete states shows an oscillatory behaviour. However, coupling between a discrete state and a continuum of states leads to *decay* [46]. The situation in the following paragraphs is that a single ion rests in a vacuum. The initial state of the ion is  $|e\rangle$ , and the initial state of the vacuum is  $\otimes_k |0\rangle$ , a product state where none of the vacuum modes  $k$  contain a photon. The ion couples to the vacuum electromagnetic field, and initially the ion plus vacuum is described by the product state  $|e, 0\rangle$ . The coupling leads to final states  $|g, 1_k\rangle$  that indicate that the particle is in its ground state and mode  $k$  of the vacuum contains one photon. After a transformation to the interaction picture, the state of the ion plus vacuum can be given at any time  $t$  as [48]

$$|\psi(t)\rangle = c_i(t)e^{-iE_e t/\hbar} |e, 0\rangle + \sum_k c_{f,k}(t)e^{-i(E_g+E)t/\hbar} |g, 1_k\rangle \quad (2.40)$$

where  $E = \hbar\omega$ ,  $c_i(t) = e^{iE_e t/\hbar} \langle e, 0|\psi(t)\rangle$  and  $c_{f,k}(t) = e^{i(E_g+E)t/\hbar} \langle g, 1_k|\psi(t)\rangle$ . Multiplying the Schrödinger equation by  $\langle e, 0|$  and, separately,  $\langle g, 1_k|$  from the left yields two coupled differential equations [46]

$$\begin{aligned} i\hbar \frac{d}{dt} c_i(t) &= \sum_k e^{i(E_0-E)t/\hbar} \langle e, 0|\hat{H}_{\text{int}}|g, 1_k\rangle c_{f,k}(t) \\ i\hbar \frac{d}{dt} c_{f,k}(t) &= e^{i(E-E_0)t/\hbar} \langle g, 1_k|\hat{H}_{\text{int}}|e, 0\rangle c_i(t) \end{aligned} \quad (2.41)$$

where  $E_0 = \hbar\omega_0$ . Combining these equations to the *Weisskopf-Wigner solution* [42, 46, 48] gives the differential equation

$$\frac{d}{dt} c_i(t) = -\frac{\Gamma}{2} c_i(t), \quad (2.42)$$

where  $\Gamma$  is the *natural linewidth* of the transition, the sum over all coupling strengths between the initial state and the final states,

$$\Gamma = \frac{2\pi}{\hbar} \cdot \sum_k |\langle e, 0|\hat{H}_{\text{int}}|g, 1_k\rangle|^2 \cdot \delta(E - E_k), \quad (2.43)$$

where  $\delta$  is the Dirac delta function and  $E_k$  the energy of the photon in mode  $k$ . The solution of Eq. (2.42) is simply

$$c_i(t) = e^{-\Gamma t/2} \quad (2.44)$$

and the probability to find the electron in  $|e\rangle$  is thus

$$p_i(t) = |c_i(t)|^2 = e^{-\Gamma t}. \quad (2.45)$$

So  $|e\rangle$  decays exponentially in time to  $|g\rangle$ , accompanied by the emission of a photon ( $\hat{a}^\dagger$ ). The probability  $p_i(t)$  falls irreversibly from  $p_i(0) = 1$  to  $p_i(t \rightarrow \infty) = 0$ . As a consequence, the excited state  $|e\rangle$  has a finite *natural lifetime*  $\tau = 1/\Gamma$ . After  $\tau$ , the excited state has decayed with a probability of  $1 - 1/e$  and a photon was emitted.

The emitted photon energy  $E = \hbar\omega$ , however, can vary. Plugging Eq. (2.44) into the second differential equation in Eq. (2.41) and looking at times  $t \gg 1/\Gamma$  gives the probability density

$$|c_{f,k}(t)|^2 = |\langle g, 1_k | \hat{H}_{\text{int}} | e, 0 \rangle|^2 \cdot \frac{1}{(E - \hbar\omega_0)^2 + \frac{1}{4}\hbar^2\Gamma^2} \quad (2.46)$$

that describes what photon energy is emitted with what probability. The probability density is described by a Lorentzian curve that has a maximum at  $E = \hbar\omega_0$ . This equation shows that the smaller  $\Gamma$  (larger  $\tau$ ), the narrower the frequency width of the Lorentzian. An intuitive view is that the Fourier transform of an exponentially decaying function in time is a Lorentzian curve in frequency. The slower the decay, the narrower the Lorentzian. The factor in front of the Lorentzian, the transition matrix element squared, changes much slower in value over an energy range  $\hbar\Gamma$  around  $E_0$  compared to the Lorentzian, and can thus be seen as an approximately constant term [46].

In Figure 2.2, the different natural lifetimes  $\tau$  of the excited states of  $^{40}\text{Ca}^+$  are shown. The excited state  $3^2\text{D}_{5/2}$  manifold of the qubit quadrupole transition has a lifetime of 1.17 s [31], which is by orders of magnitudes longer compared to the other excited states. The reason for this increased lifetime is that for the case where the diameter of the ion is by orders of magnitude smaller than the resonant photon's wavelength, the matrix element  $\langle g, 1_k | \hat{H}_{\text{int}} | e, 0 \rangle$  for a quadrupole transition is by orders of magnitude smaller compared to a dipole transition.

The correspondingly narrow linewidth in a quadrupole transition goes both ways: A photon can only drive the  $|1\rangle$  to  $|0\rangle$  transition in  $^{40}\text{Ca}^+$  with a non-negligible probability when the energy  $E$  is close to  $\hbar\omega_0$  by  $\sim \hbar\Gamma$ . A light source that can fulfill this requirement, of a frequency linewidth on the order of a few Hz, is a *laser*.

### 2.2.2. Initialization, manipulation and measurement of the encoded qubit

Five different transitions are depicted in the energy level spectrum in Figure 2.2. All five depicted transitions are at optical frequencies and can be driven by lasers. The quadrupole transition that couples the  $4^2\text{S}_{1/2}$  ( $|1\rangle$ ) and  $3^2\text{D}_{5/2}$  ( $|0\rangle$ ) manifolds at 729 nm can be used to manipulate a qubit whose logical states are encoded into  $^{40}\text{Ca}^+$  across these manifolds. The methods to perform quantum gates via this transition are presented in the next subsection. Next to the qubit transition there are four additional transitions shown in the figure, which are used for initialization, manipulation and measurement of the qubit in our research team at the University of Innsbruck and many other research teams and groups that work with trapped  $^{40}\text{Ca}^+$ . The rest of this subsection will be devoted to a brief introduction to those methods. For more details on the experimental methods of initialization and measurement

of  $^{40}\text{Ca}^+$  ion-qubits in a linear Paul trap the reader is referred to [39].

DiVincenzo's second requirement for a quantum computer states that there has to be a way to initialize qubits in a low-entropy fiducial state [7]. From this requirement it follows that once the ion is trapped, it needs to be slowed down. One process for reducing the ion's speed that is used in our team is *Doppler cooling* [49], which is done via a 397 nm laser driving the  $4^2\text{S}_{1/2}$  ( $|1\rangle$ ) to  $4^2\text{P}_{1/2}$  ( $|0\rangle$ ) transition. For Doppler cooling, this laser is red-detuned from the transition center frequency. The idea behind Doppler cooling is that when the ion is moving against the direction of laser light propagation, it experiences the light shifted more towards the center frequency because of the Doppler effect, which increases the probability of excitation. The excitation of the ion is accompanied by a momentum kick that reduces the speed of the ion. The subsequent photon emission is also accompanied by a momentum kick, but this time the direction of emission is random. So, after several cycles of excitation and emission, there is a net reduction of the ion's speed along the axis of laser propagation. The ion's lowest possible temperature through Doppler cooling is reached at the *Doppler limit*, which is [45] (in the simplified case of a two-level ion and laser light whose intensity is below the transition's saturation intensity [50])

$$T_{\min} = \frac{\hbar\Gamma}{2k_{\text{B}}} \quad (2.47)$$

where  $\Gamma$  is the natural linewidth and  $k_{\text{B}}$  the Boltzmann constant. Using the 397 nm transition for Doppler cooling sets the Doppler limit at  $T_{\min} \sim 0.5$  mK. In approximately 6% of cases, the electron jumps from  $4^2\text{P}_{1/2}$  to  $3^2\text{D}_{3/2}$ . In order to get the electron back to  $4^2\text{P}_{1/2}$ , a repumping laser at 866 nm is used.

A 397 nm laser can also be used for the measurement of the qubit state. The measurement process is called *fluorescence spectroscopy* or *electron shelving* [51] and works as follows: In case the electron is in  $4^2\text{S}_{1/2}$  ( $|1\rangle$ ), a 397 nm laser can bring it to  $4^2\text{P}_{1/2}$ . The photon, which is emitted after 7.7 ns, is recorded by a camera with a probability  $< 1$ . If the electron is in  $3^2\text{D}_{5/2}$  ( $|0\rangle$ ), no excitation to  $4^2\text{P}_{1/2}$  and no subsequential photon emission can happen, leading to a "dark ion". After a large number of ion excitations and photon emissions, it can be determined whether the electron is in  $|0\rangle$  or  $|1\rangle$ .

The 393 nm and 854 nm transitions can be used to implement a *Raman process*. In this process, the electron is shelved from  $4^2\text{S}_{1/2}$  ( $|1\rangle$ ) to  $3^2\text{D}_{5/2}$  ( $|0\rangle$ ) via the 393 nm and 854 nm transitions, using  $4^2\text{P}_{3/2}$  as an intermediate virtual state. One application in our team that uses this process is the deterministic creation of a single photon via a *cavity-mediated Raman process*. A description of the Raman process and more specifically a cavity-mediated Raman process can be read in [52].

### 2.2.3. Performing a universal gate set using $^{40}\text{Ca}^+$

As stated in Section 2.1, arbitrary unitary evolution of qubits can be realized using a gate set consisting of single-qubit operations and a two-qubit entangling gate. This section presents a universal gate set that can be realized on qubits encoded in  $^{40}\text{Ca}^+$  ions [39]. For single-qubit operations, 729 nm laser light and the *AC Stark effect* are used to achieve arbitrary rotations on the Bloch sphere. For the entangling gate the so-called *Mølmer-Sørensen gate* [53] is used.

With the exception of Eq. (2.49), this subsection is not needed to understand the experimental results of this thesis in Chapter 6 and Chapter 7. However, this subsection uses the theoretical background that was presented and gives a justification for the importance of the 729 nm laser in quantum information science experiments with trapped  $^{40}\text{Ca}^+$  ions.

### Single qubit operations in $^{40}\text{Ca}^+$

Arbitrary single qubit rotations on the Bloch sphere can be realized using the rotations  $\hat{R}_{x,y}(\theta_1, \phi_1)$  and  $\hat{R}_z(\theta_1)$  (Eq. (2.18)). A way to implement these two rotations using 729 nm laser light is now presented. A derivation of the interaction Hamiltonians that are introduced can be found in [39].

In the case where the 729 nm laser frequency  $\omega$  is equal to the qubit transition frequency  $\omega_0$ , the interaction Hamiltonian can be approximated by

$$\hat{H}_{\text{SQO},1} = \hbar\Omega \left( \cos(\phi_1)\hat{\sigma}_x - \sin(\phi_1)\hat{\sigma}_y \right). \quad (2.48)$$

Here,  $\Omega$  is the electric quadrupole Rabi frequency (Eq. (2.39)) and  $\phi_1$  denotes the optical phase of the laser light. A more complete model of the resonant case that includes the coupling of the laser to the motional sidebands of the ion (parameterized by the *Lamb-Dicke parameter*) is given later in this subsection, when the Mølmer-Sørensen gate is presented. The Schrödinger equation can be solved for this time-independent Hamiltonian to arrive at the unitary operation

$$\hat{R}_{x,y}(\theta_1, \phi_1) = \exp \left( -it\hat{H}_{\text{SQO},1}/\hbar \right) \quad (2.49)$$

This is a rotation around an axis in the  $x$ - $y$  plane of the Bloch sphere.

In the case where the 729 nm laser frequency has a detuning  $\delta$  that is large in comparison to the Rabi frequency ( $\delta \gg \Omega$ ), resonant excitation can be ignored and an AC Stark shift  $\delta_{\text{AC}}$  appears that changes the transition frequency by [45]

$$\delta_{\text{AC}} = \frac{\Omega^2}{2\delta} \quad (2.50)$$

and leads to a laser-qubit interaction that can be described by the Hamiltonian

$$\hat{H}_{\text{SQO},2} = \frac{1}{2}\hbar\delta_{\text{AC}} \hat{\sigma}_z. \quad (2.51)$$

Using again the Schrödinger equation to arrive at the unitary operator

$$\hat{R}_z(\theta_1) = \exp \left( -it\hat{H}_{\text{SQO},2}/\hbar \right) \quad (2.52)$$

where  $\theta_1 = \delta_{\text{AC}} t$ . This is a rotation around the  $z$ -axis of the Bloch sphere. In conclusion, by using sequences of 729 nm laser operations in which the laser is either on resonance with the qubit transition frequency or at a detuning  $\delta \gg \Omega$ , arbitrary single-qubit operations on a trapped ion can be performed.

### Entangling operations: The Mølmer-Sørensen gate

The three orthogonal motional states of a trapped single ion can each be described as states of a quantum harmonic oscillator. Consider one oscillator with frequency  $\omega_m$ . The creation of one quantum of motion or *phonon* in the oscillator is achieved via the creation operator

## 2. Quantum Information Science with Trapped Ions

$\hat{a}^\dagger$ , the removal via the annihilation operator  $\hat{a}$ . In the following paragraphs, the interaction between 729 nm laser light at a frequency  $\omega$ , the ion's internal electronic states and one of the ion's external motional states is considered.

So-called *sideband transitions* at laser frequencies  $\omega = \omega_0 \pm \omega_m$  allow for a simultaneous interaction with the ion's internal electronic states and external motional states (of a quantum harmonic oscillator with frequency  $\omega_m$ ). The coupling strength between the internal and external motional oscillator is quantified by the *Lamb-Dicke parameter* [54]

$$\eta = \frac{\omega}{c} \sqrt{\frac{\hbar}{2m\omega_m}} \cdot \cos(\theta). \quad (2.53)$$

Here,  $\theta$  is the angle between the laser beam's direction and the ion's direction of motion,  $c$  is the speed of light in vacuum and  $m$  is the ion's mass. The *Lamb-Dicke regime* [54] is fulfilled when  $\eta^2(2\bar{n} + 1) \ll 1$ , where  $\bar{n}$  is the average number of phonons in the oscillator. In the Lamb-Dicke regime, the coupling between the ion's internal electronic states and external motional states is so weak that the probability for the phonon number  $n$  to be changed by more than 1 when a finite length laser pulse is sent to the ion at a frequency set at  $\omega = \omega_0 \pm \omega_m$  is negligibly small. The Doppler cooling temperature for  $^{40}\text{Ca}^+$  (Doppler cooling with 397 nm) is according to Eq. (2.47)  $T_{\min} \sim 0.5$  mK. The mean phonon number of a trapped ion oscillating at a frequency  $\omega_m$  after Doppler cooling can be calculated via [39]

$$\bar{n} = \frac{k_B T_{\min}}{\hbar\omega_m}. \quad (2.54)$$

For typical parameters ([39]) of  $\omega_m \sim 2\pi \cdot 1$  MHz and  $\eta \sim 0.1$ , the mean phonon number is  $\bar{n} \sim 10$  and the condition for the Lamb-Dicke regime is fulfilled ( $0.21 \ll 1$ ). In our team, the condition for the Lamb-Dicke regime is fulfilled after Doppler cooling.

If additionally  $\Omega \ll \omega_m$ , the laser-ion system is in the *resolved sideband limit* [50]. Then, three interaction Hamiltonians can be found and selectively driven by the 729 nm laser by choosing the appropriate detuning  $\delta$  from  $\omega_0$ .

For  $\delta = 0$ , the *carrier* transition Hamiltonian is given by

$$\hat{H}_{\text{car}} = \hbar\Omega (1 - \eta n) \left( \cos(\phi_1) \hat{\sigma}_x - \sin(\phi_1) \hat{\sigma}_y \right) \quad (2.55)$$

Here, the interaction couples the states  $|g\rangle \otimes |n\rangle$  with the states  $|e\rangle \otimes |n\rangle$  and thus only changes the internal electronic configuration, not the motional state.

For  $\delta = -\omega_m$ , the *red sideband* transition Hamiltonian is given by

$$\hat{H}_{\text{rsb}} = \frac{i}{2} \hbar \eta \sqrt{n} \Omega \left( e^{i\phi_1} \hat{a} \hat{\sigma}_+ + e^{-i\phi_1} \hat{a}^\dagger \hat{\sigma}_- \right) \quad (2.56)$$

Here,  $\hat{\sigma}_\pm = (\hat{\sigma}_x \pm i\hat{\sigma}_y)$ . Here, the interaction couples  $|g\rangle \otimes |n\rangle$  with  $|e\rangle \otimes |n-1\rangle$ .

The *blue sideband* transition Hamiltonian is used to describe the interaction when  $\delta = +\omega_m$ ,

$$\hat{H}_{\text{bsb}} = \frac{i}{2} \hbar \eta \sqrt{n+1} \Omega \left( e^{i\phi_1} \hat{a}^\dagger \hat{\sigma}_+ + e^{-i\phi_1} \hat{a} \hat{\sigma}_- \right). \quad (2.57)$$

At the blue sideband transition, the interaction couples  $|g\rangle \otimes |n\rangle$  with  $|e\rangle \otimes |n+1\rangle$ .

In the original publication on realizing an ion-trap quantum computer [26], the authors propose the creation of a CNOT gate (Eq. (2.20)) by entangling the electronic states of cotrapped ions with the help of their shared motion, using finite length laser pulses with a

## 2. Quantum Information Science with Trapped Ions

frequency set at  $\omega \pm \omega_m$ . The realization of this *Cirac-Zoller CNOT gate* requires the ion to be prepared in the motional ground state.

In modern quantum information science experiments with trapped ions the Mølmer-Sørensen gate is more commonly used [55] that does not initially require a motional ground state, only the Lamb-Dicke regime. For a Mølmer-Sørensen gate, two laser beams detuned to  $\omega = \omega_0 \pm (\omega_m + \delta_{\text{add}})$  are added to create a *bichromatic light field*, which simultaneously off-resonantly excites the ion's blue and red sidebands. Here,  $\delta_{\text{add}}$  is an additional detuning, small in comparison to  $\omega_m$ . In the two-ion Mølmer-Sørensen gate, both ions are excited by this bichromatic light field, leading to the time-dependent two-qubit interaction Hamiltonian [53]

$$\hat{H}_{\text{MS}}(t) = -\hbar\eta\Omega \left( \hat{a}^\dagger e^{i\delta_{\text{add}}t} + \hat{a} e^{-i\delta_{\text{add}}t} \right) \cdot \left( \hat{\sigma}_y \otimes \mathbb{I}_2 + \mathbb{I}_2 \otimes \hat{\sigma}_y \right). \quad (2.58)$$

The Hamiltonian can be integrated to yield the unitary, which at the time  $t_{\text{MS}} = 2\pi/\delta_{\text{add}}$  reads

$$\hat{U}(t_{\text{MS}}) = \exp \left( 2\pi i \left( \frac{\eta\Omega}{\delta_{\text{add}}} \right)^2 \cdot \left( \hat{\sigma}_y \otimes \mathbb{I}_2 + \mathbb{I}_2 \otimes \hat{\sigma}_y \right)^2 \right). \quad (2.59)$$

This unitary can create entanglement between the two ion-qubits. For example, the product state  $|g\rangle \otimes |g\rangle = |g, g\rangle$  is evolved into a Bell state. This unitary is therefore equal to a two-qubit maximally entangling gate, completing a universal gate set for trapped  $^{40}\text{Ca}^+$  ions driven by a 729 nm laser.

# 3. Laser Physics

Chapter 2 lays out the importance of lasers in quantum information science experiments with trapped ions. In this chapter, the relevant physics of lasers is summarized. In Section 3.1, an introduction to laser theory is given, beginning with a summary of the fundamental processes that happen in a laser medium and followed by a plan on how to construct a laser. Further, laser beams and the laser linewidth are presented. In Section 3.2, different approaches to measure the linewidth are given. Finally, in Section 3.3, a generic description of the titanium-doped sapphire laser is given.

## 3.1. Laser Theory

### 3.1.1. Principle of work of a laser

#### Absorption, spontaneous and stimulated emission in an ensemble of particles

In Subsection 2.2.1, it is shown that an excited two-level particle that couples to the vacuum electromagnetic field modes gives this energy irreversibly into the vacuum in the form of a photon after a characteristic time  $\tau = 1/\Gamma$ . This process is known as *spontaneous emission*. Further it is noted that if there is a photon in the vacuum with an adequate energy, the particle can be excited. This process is called *absorption*. A third process, *stimulated emission* [42], happens when the particle is already excited and then interacts with a photon of adequate energy in the vacuum. As a consequence of this interaction, the particle gives its energy irreversibly into the vacuum in the form of a photon. It follows from energy and momentum conservation that the emitted photon has the same momentum vector  $\hbar\vec{k}$  and polarization vector  $\vec{\epsilon}$  as the stimulating photon. Spontaneous emission, absorption and stimulated emission all play a crucial role in laser physics, as will be further elaborated.

#### Construction of a laser

Now, an ensemble of identical particles is considered. If one of the excited states that can be found in every particle of the ensemble is sustainably more populated than the ground state, which is called *population inversion*, an “avalanche” of identical photons can be produced because stimulated emission can happen more often than absorption. One piece of technology that builds on this phenomenon is the *laser*, which is an acronym for *light amplification by stimulated emission of radiation*.

It can be shown that a two-level particle cannot reach population inversion [48]. As a consequence, a two-level laser cannot exist. However, population inversion can be reached through three- or four-level systems. Figure 3.1 shows the energy level scheme of a four-level laser. The electrons in the particles are pumped from a ground state  $|0\rangle$  to the pump state  $|p\rangle$ , from where they decay into the upper laser level  $|e\rangle$ . The combined pump rate to the

### 3. Laser Physics

upper laser level is denoted  $R$ . A three-level laser can exist when  $|p\rangle$  and  $|e\rangle$  are the same energy level. In order to pump electrons to  $|e\rangle$ , energy has to be applied to the system. This can be done in several ways, for example by applying an electric current, a flashlight or another laser. The electron in the upper laser level then decays spontaneously at a rate  $\Gamma$  to the lower laser level  $|g\rangle$ , and from there back to  $|0\rangle$  at a depopulation rate  $\Gamma_d$ . The master equation describing the dynamics of the electron population in the upper lasing level  $\sigma_e$  and the electron population in the lower lasing level  $\sigma_g$  reads [48]

$$\begin{aligned}\frac{d}{dt}\sigma_e &= R - \Gamma\sigma_e \\ \frac{d}{dt}\sigma_g &= \Gamma\sigma_e + \Gamma_d\sigma_g.\end{aligned}\tag{3.1}$$

In the steady-state case where  $d\sigma_e/dt = 0$ , the difference between the populations is

$$\Delta\sigma = \sigma_e - \sigma_g = \frac{R}{\Gamma} \left(1 - \frac{\Gamma}{\Gamma_d}\right).\tag{3.2}$$

Stimulated emission is not considered in this equation yet because the first goal is to achieve population inversion —  $\Delta\sigma > 1$  — a resource that can then provide for sustained stimulated emission. Eq. (3.2) shows that population inversion can be achieved if  $\Gamma < \Gamma_d$ . Furthermore,  $\Delta\sigma$  is increased the larger  $R$ , the larger  $\Gamma_d$  and the smaller  $\Gamma$ . So the ideal four-level scheme for a laser would have an upper laser level  $|e\rangle$  with a lifetime that is much longer than either the pump state  $|p\rangle$  or the lower laser level  $|g\rangle$ . The ensemble of particles that allows for population inversion now also allows for light amplification by stimulated emission of radiation [48]. In the context of a laser, this ensemble of particles is called the *optical gain medium*. The final ingredient for a laser is a *resonator*, usually two mirrors, that reflect emitted photons back into the optical gain medium, leading to an “avalanche” of stimulated radiation. If one mirror is intentionally designed to transmit a fraction of photons, a *laser beam* can be created. Stimulated emission and spontaneous emission reduce  $\Delta\sigma$ , but through pumping the amplification can be maintained. As long as the optical gain  $\gamma$  through pumping outweighs the losses  $\alpha$  of photons, the light field is amplified. Losses include outcoupling of photons through the mirrors as well as absorption and scattering of photons. After a certain time, however, the laser reaches the point where  $\gamma = \alpha$ . This is the *steady-state regime*, and the laser outputs a constant power. A sketch of the basic elements that are needed to construct a laser is shown in Figure 3.2.

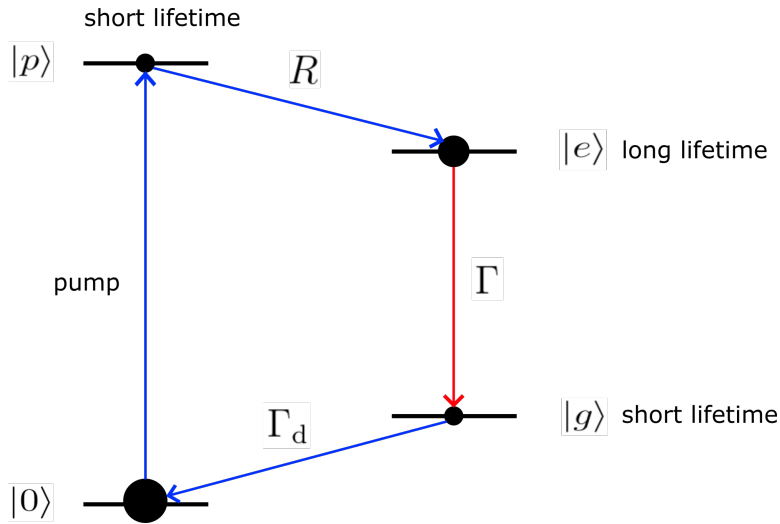


**Figure 3.1.: Energy level diagram of a four-level laser.** The state  $|0\rangle$  is the ground state,  $|p\rangle$  the pump state,  $|e\rangle$  the upper laser level and  $|g\rangle$  the lower laser level. In the figure,  $R$  denotes the pump rate,  $\Gamma$  the rate of spontaneous emission between the laser levels and  $\Gamma_d$  the depopulation rate. The red arrow indicates the lasing transition. The black circles on the energy levels indicate the populations in the whole gain medium. Population inversion is when the circle of  $|e\rangle$  is larger than the circle of  $|g\rangle$ .

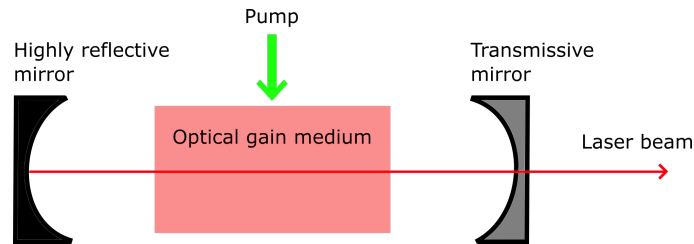


**Figure 3.2.: A minimal setup that realizes a laser.** The optical gain medium is pumped with external energy so that a population inversion sets in. An example energy level diagram of a four-level particle in the gain medium is shown in the previous figure, Figure 3.1. Stimulated emission is amplified by placing the gain medium in a resonator, which can be constructed by two mirrors. One mirror is highly reflective, the other mirror is partially transmissive so that a laser beam can exit the resonator.

### 3.1.2. Laser beams

Two mirrors placed on opposite sides around the optical gain medium can be used to build a laser resonator. The pair of mirrors can work as a resonator if they fulfill the condition [48]

$$0 \leq \left(1 - \frac{L}{R_1}\right) \left(1 - \frac{L}{R_2}\right) \leq 1, \quad (3.3)$$

where  $L$  is the distance between the two mirrors and  $R_1, R_2$  are the mirrors' radii of curvature. Electric fields that can form in resonators along an optical axis  $z$  are solutions of the Helmholtz equation in the paraxial approximation and are called *Gaussian modes*. The paraxial approximation can be made when the angle between the wave vector  $\vec{k}$  of the electric field inside the resonator and the optical axis  $z$  is  $\ll 1$ . The electric field of a Gaussian mode with amplitude  $E_0$  reads [48]

### 3. Laser Physics

$$E_{mn}(x, y, z) = E_0 \mathcal{H}_m\left(\frac{\sqrt{2}x}{w(z)}\right) \mathcal{H}_n\left(\frac{\sqrt{2}y}{w(z)}\right) \frac{w_0}{w(z)} \exp\left(-\frac{x^2 + y^2}{w^2(z)}\right) \exp\left(ik\frac{x^2 + y^2}{2R(z)}\right) \exp\left(i((kz - (m + n + 1)\eta(z)))\right) \quad (3.4)$$

when the two mirrors are separated in  $z$ -direction. In this equation,  $m$  and  $n$  indicate the different *transversal electromagnetic modes* (TEM <sub>$mn$</sub> ) and define the spatial distribution of the electric field perpendicular to the optical axis, the  $x$ - $y$  plane, through the Hermite polynomials  $\mathcal{H}_{m,n}$ . The Gaussian principle mode is TEM<sub>00</sub> and reads

$$E_{00}(x, y, z) = E_0 \frac{w_0}{w(z)} \exp\left(-\frac{x^2 + y^2}{w^2(z)}\right) \exp\left(ik\frac{x^2 + y^2}{2R(z)}\right) \exp\left(i(kz - \eta(z))\right). \quad (3.5)$$

When one of the two resonator mirrors is partially transmissive, the  $E_{00}$  field that has built up inside the resonator can propagate into free space. This freely propagating electric field is also called a *Gaussian beam* and is colloquially known as a laser beam. With the choice of coordinates in Eq. 3.5, the laser beam is propagating in the  $z$ -direction. In the following paragraphs, the different quantities appearing in Eq. (3.5) are further elaborated.

In Eq. (3.5), the first exponential term shows that the electric field strength is changing its value in  $x$ - $y$  direction according to a Gaussian (normal) distribution. The beam radius  $w(z)$  is the circle in the  $x - y$  plane at which the field strength has reduced to  $1/e$  from the value in the center. A Gaussian beam can be regarded as a spatially constrained superposition of plane waves. In contrast to plane waves however, due to their finite spatial extent, Gaussian beams have a finite momentum extent and are thus prone to divergence. The smallest beam radius is called the *beam waist radius*  $w_0$ , and the beam radius  $w(z)$  at a position  $z$  can be calculated via [48]

$$w(z) = w_0 \sqrt{1 + \left(\frac{z}{z_0}\right)^2}. \quad (3.6)$$

Here,  $z_0$  is the *Rayleigh length*: The position along the  $z$ -direction at which the beam cross section has doubled compared to the cross section at  $w_0$ . For light of wavelength  $\lambda = 2\pi/k$ , the Rayleigh length is given by

$$z_0 = \frac{\pi w_0^2}{\lambda}. \quad (3.7)$$

In the far field where  $z \gg z_0$ , the beam radius can be approximated by

$$w(z) \sim w_0 \frac{z}{z_0} = z \theta_{\text{div}} \quad (3.8)$$

where  $\theta_{\text{div}} = w_0/z_0$  is the beam's angle of divergence.

A Gaussian beam's curvature can be calculated to be

$$R(z) = z \left(1 + \left(\frac{z_0}{z}\right)^2\right). \quad (3.9)$$

The third term in Eq. (3.5) includes the *Gouy phase*

### 3. Laser Physics

$$\eta(z) = \arctan\left(\frac{z}{z_0}\right), \quad (3.10)$$

which describes the deviation in phase evolution that a Gaussian beam experiences compared to a plane wave.

A laser beam's intensity is calculated via

$$I(x, y, z) = \frac{1}{2}\epsilon_0 c |E_{mn}(x, y, z)|^2 \quad (3.11)$$

and the *radiation pressure* exhibited by the laser beam is proportional to the intensity,

$$p_{\text{rad}}(x, y, z) = \frac{I(x, y, z)}{c}. \quad (3.12)$$

The laser power is calculated by integration of the intensity over the  $x$ - $y$  plane,

$$P(z) = \int_{-\infty}^{\infty} \int_{-\infty}^{\infty} I(x, y, z) dx dy. \quad (3.13)$$

#### 3.1.3. Laser linewidth

##### Reasons for a linewidth

Up to now, laser light was described as being monochromatic, only consisting of a single frequency  $\omega$ . However, spontaneous emission and losses in the optical gain medium lead to phase fluctuations of the laser field, and as a consequence the laser transition has an unavoidable broadening of its optical spectrum. The contribution of spontaneous emission and losses in the optical gain medium of a laser to the linewidth (FWHM) of the laser is given by the *Schawlow-Townes linewidth* [48]

$$\Delta\nu = \frac{\pi h\nu(\delta\nu_c)^2}{P}, \quad (3.14)$$

where  $h$  is the Planck constant,  $\nu$  is the laser frequency,  $\delta\nu_c$  is the laser resonator linewidth and  $P$  is the laser power. The frequency is here expressed as  $\nu = \omega/2\pi$ . For example, a laser linewidth of  $\Delta\nu = 1$  Hz means that the center frequency  $\nu$  is expected to vary by  $\pm 1$  Hz over the course of one second i.e., there is one oscillation of the light field more or less per second. From now on,  $\nu$ , which is in the unit of Hertz, will be used instead of  $\omega$ .

Even though the Schawlow-Townes linewidth sets a fundamental limit to the laser linewidth, this lower limit is hardly reached in practice. Environmental effects like mechanical vibrations, temperature or air pressure fluctuations can change the laser resonator length or the laser transition frequency on different timescales. Effects like these lead to a laser linewidth that is usually orders of magnitude broader than the Schawlow-Townes limit.

##### Lineshape

A monochromatic light source has one frequency  $\nu_0$ . The laser linewidth originates from phase — and thus frequency — noise, which contributes to nonzero laser frequency components below and above the value  $\nu_0$ . This noise can be expressed by the frequency noise

### 3. Laser Physics

spectral density  $S_n(\nu)$ . The following autocorrelation function compares the electric field of the laser light  $E$ , with amplitude  $E_0$ , at two separate points  $t, t + t'$  in time [56]:

$$\Gamma_A(t') = E^*(t) \cdot E(t + t') = E_0^2 \exp\left(2\pi i \nu t' - \frac{2}{(\pi t')^2} \int_0^\infty S_n(\nu') \operatorname{sinc}^2(\pi \nu' t') d\nu'\right), \quad (3.15)$$

where  $*$  denotes the complex conjugate. The lineshape  $g(\nu)$  of the laser can then be evaluated via the *Wiener-Khintchin theorem* [48] that connects  $g(\nu)$  to the Fourier transform of the autocorrelation function

$$g(\nu) = 2 \int_{-\infty}^{\infty} e^{-2\pi i \nu t'} \Gamma_A(t') dt'. \quad (3.16)$$

For an arbitrary noise spectrum  $S_n(\nu)$  the lineshape function cannot be analytically solved. However, in [56], two extreme cases are presented for which an analytical solution exists. The spectral noise density  $S_n(\nu)$  is approximated by

$$S_n(\nu) = \begin{cases} h_0, & \nu \leq \nu_c \\ 0, & \nu > \nu_c, \end{cases} \quad (3.17)$$

where  $\nu_c$  is the cutoff frequency and  $h_0$  is a constant. At one extreme, sending  $\nu_c \rightarrow \infty$ , which corresponds to white noise, yields a lineshape

$$g_{\text{white}}(\nu) = E_0^2 \cdot \frac{h_0}{(\nu - \nu_0)^2 + (h_0 \pi / 2)^2}, \quad (3.18)$$

which is a Lorentzian distribution in the frequency picture around  $\nu_0$  with a FWHM of  $\pi h_0$ . At the other extreme, sending  $\nu_c \rightarrow 0$ , which corresponds to low frequency noise, gives

$$g_{\text{low}}(\nu) = E_0^2 \sqrt{\frac{2}{h_0 \pi \nu_c}} e^{-\frac{(\nu - \nu_0)^2}{2 h_0 \nu_c}}, \quad (3.19)$$

which is a Gaussian distribution in the frequency picture around  $\nu_0$  with a FWHM of  $\sqrt{8 \ln(2) h_0 \nu_c}$ .

In summary, white noise gives a Lorentzian lineshape, while low frequency noise contributes to a Gaussian shape [56]. In case the cutoff frequency is inbetween the two extremes, the lineshape can be described by a Voigt profile: the convolution between a Lorentzian and a Gaussian.

#### Fiber noise

One reason for a broadening of the laser light's linewidth outside the laser resonator is known as *fiber noise*. When light travels through an optical fiber, there are several effects that lead to a modulation of phase noise on the light. These effects include pressure changes, especially from vibrations and speech, as well as thermal fluctuations and bending of the fiber. Optical fibers are linear and reciprocal, so two counterpropagating laser beams propagate independently and experience the same noise. These properties of optical fibers are used to remove fiber noise through a negative feedback loop called *fiber noise cancellation* that was first introduced in 1994 [57]. One way to set up a fiber noise cancellation feedback loop is shown in Subsection 5.3.3.

## 3.2. Measuring the Laser Linewidth

In order for the laser to not be the limiting factor for the coherence time in quantum information science experiments with trapped  $^{40}\text{Ca}^+$  ions where the qubit is encoded between the  $4^2\text{S}_{1/2}$  and  $3^2\text{D}_{5/2}$  manifolds, the laser linewidth should not be greater than  $\Delta\nu = 1$  Hz. A mathematical derivation of the link between the laser linewidth and the qubit coherence time can be found e.g., in [58]. It follows that the measurement of the linewidth is a key characterization of a laser. Three ways to measure the laser linewidth will be discussed.

### 3.2.1. Beat measurement

The fastest photodetectors that are available have bandwidths up to around  $\sim 10$  GHz. No photodetector is capable of measuring optical frequencies, which lie in the  $\sim 100$  THz regime. To overcome this limitation, a *beat note* between two lasers can be measured. For this, two light fields are superimposed and the resulting frequency difference is measured by a photodetector. The result is a convolution of the spectrum of the two lasers. In order to determine the spectrum of any one of the lasers, the spectrum of the other has to be known. To overcome this limitation, a so-called *three-cornered hat measurement* can be performed. Here, beats between all pairs of three lasers are taken, which allow the linewidths of each individual laser to be determined. In the following subsections, these techniques are described mathematically.

#### Beat measurement between two lasers

Two electric fields  $E_1$ ,  $E_2$  of the type Eq. (2.32) are superimposed on a photodetector. In the case that the phases of both electric fields are set to 0, the superimposed field can be written as

$$E(t) = E_1(t) + E_2(t) = E_{0,1} \cos(2\pi\nu_1 t) + E_{0,2} \cos(2\pi\nu_2 t). \quad (3.20)$$

Using Eq. (3.11), the intensity measured by the photodetector is

$$I(t) = I_1(t) + I_2(t) + \sqrt{I_{0,1}I_{0,2}} \left( \cos((2\pi\nu_1 + 2\pi\nu_2)t) + \cos((2\pi\nu_1 - 2\pi\nu_2)t) \right), \quad (3.21)$$

where the first three terms oscillate at optical frequencies. In the case where the frequency difference of the laser fields is less than the bandwidth of the photodetector, the oscillation in the last term in Eq. (3.21) that includes the frequency difference can be measured by a photodetector. A spectrum analyzer can then measure the frequency distribution present in the photodetector output signal.

In the case that the spectrum of both lasers is described by a Lorentzian lineshape, the standard deviations of the individual lasers' frequencies add up to the total measured standard deviation [59]

$$\sigma_{12} = \sigma_1 + \sigma_2. \quad (3.22)$$

The standard deviation of a Lorentzian distribution is connected to the linewidth (FWHM) via

$$\Delta\nu = \sigma. \quad (3.23)$$

In the case that the spectrum of both lasers is described by a Gaussian lineshape, the squares of the individual standard deviations add to the square of the total standard deviation [59]

$$\sigma_{12}^2 = \sigma_1^2 + \sigma_2^2. \quad (3.24)$$

The standard deviation of a Gaussian distribution is connected to the linewidth (FWHM) via

$$\Delta\nu = \sqrt{8 \ln(2)} \sigma. \quad (3.25)$$

The previous two equations show that when beating two lasers, the linewidth of one laser can only be known when the other laser's linewidth is known. Otherwise, the measured linewidth can only be interpreted as an upper limit for the individual linewidths.

### The three-cornered hat measurement

For a three-cornered hat measurement, beats between all pairs of three lasers are taken. This measurement allows the linewidths of three lasers to be determined. Just as in Eq. (3.22), three beats between the three lasers with standard deviations of their frequency spectrum  $\sigma_{12}$ ,  $\sigma_{23}$  and  $\sigma_{13}$  are performed. The three beats yield a linear system of three equations with three variables that can be solved for  $\sigma_1$ ,  $\sigma_2$  and  $\sigma_3$ . For the case in which all three lasers have a Lorentzian lineshape, the solutions read

$$\begin{aligned} \sigma_1 &= \frac{1}{2}(\sigma_{12} + \sigma_{13} - \sigma_{23}) \\ \sigma_2 &= \frac{1}{2}(\sigma_{12} + \sigma_{23} - \sigma_{13}) \\ \sigma_3 &= \frac{1}{2}(\sigma_{13} + \sigma_{23} - \sigma_{12}) \end{aligned} \quad (3.26)$$

and for the case in which all three lasers have a Gaussian lineshape the solutions read

$$\begin{aligned} \sigma_1^2 &= \frac{1}{2}(\sigma_{12}^2 + \sigma_{13}^2 - \sigma_{23}^2) \\ \sigma_2^2 &= \frac{1}{2}(\sigma_{12}^2 + \sigma_{23}^2 - \sigma_{13}^2) \\ \sigma_3^2 &= \frac{1}{2}(\sigma_{13}^2 + \sigma_{23}^2 - \sigma_{12}^2). \end{aligned} \quad (3.27)$$

One assumption for the measurement is that the causes for linewidth broadening are independent for each laser. Further, the three beat measurements are ideally performed simultaneously so that any time-dependent changes of the linewidth can be assigned to a specific laser system.

The center frequency of the beat can be prone to a frequency *drift* over time, shifting the entire beat profile along the frequency axis. Using a three-cornered hat measurement, the *absolute* frequency drift of each involved laser can be calculated via

$$\begin{aligned}
 D_1 &= \frac{1}{2}(D_{12} + D_{13} - D_{23}) \\
 D_2 &= \frac{1}{2}(D_{12} + D_{23} - D_{13}) \\
 D_3 &= \frac{1}{2}(D_{13} + D_{23} - D_{12}).
 \end{aligned} \tag{3.28}$$

Here,  $D_{12}, D_{13}, D_{23}$  are the frequency drifts of the center values of the beat measurements between laser pairs that are the sum of the individual lasers' frequency drifts.

### 3.2.2. Ramsey experiment

Another way to determine a laser's linewidth is with the help of a *Ramsey experiment* [60]. In the case of  $^{40}\text{Ca}^+$ , the qubit transition at 729 nm can be used for a Ramsey experiment, in which a sequence of laser operations are carried out. In the following, the laser pulses defined in Section 2.1 are employed. At the beginning, the ion-qubit is in the state  $|0\rangle$ . As a first step, a  $\pi/2$  pulse  $\hat{R}_{x,y}(\pi/2, \phi_1)$  is sent to the ion, which changes the qubit state  $|0\rangle$  to the superposition  $|+\rangle$ .

Without any interaction to an external field, the Hamiltonian of a qubit reads

$$\hat{H}_{\text{qubit}} = E_0 |0\rangle \langle 0| + E_1 |1\rangle \langle 1|, \tag{3.29}$$

in analogy to the particle Hamiltonian in Eq. (2.27). Solving the Schrödinger equation for this time-independent Hamiltonian yields the solution

$$|\psi(t)\rangle = e^{-i\hat{H}t/\hbar} |+\rangle = \hat{U}_{\text{free}} |+\rangle \tag{3.30}$$

where  $\hat{U}_{\text{free}}$  is the free evolution operator and  $|+\rangle$  is the state at a time  $t = 0$ , right after the  $\pi/2$  pulse. Using the spectral theorem to expand the solution in the energy eigenbasis of a qubit yields

$$|\psi(t)\rangle = \frac{e^{-iE_0t/\hbar}}{\sqrt{2}} \left( |0\rangle + e^{-2\pi i\nu_0 t} |1\rangle \right), \tag{3.31}$$

where  $\nu_0 = (E_1 - E_0)/\hbar$ . The expression  $\phi = 2\pi\nu_0 t$  is then the relative phase that was introduced in Eq. (2.13). The relative phase  $\phi$  evolves in time  $t$ , leading to a rotation of the qubit vector on the equator of the Bloch sphere at a frequency  $\nu_0$ .

Now, the laser field is again taken into consideration. If the laser field is resonant with the ion, the laser phase  $\phi_1$  is also evolving at the same rate, so that the phase relation between the ion and the laser stays constant. A second  $\pi/2$  pulse  $\hat{R}_{x,y}(\pi/2, \phi_1)$  after a waiting time  $\tau$  then puts the qubit state in the equatorial plane,  $|\psi\rangle = (|0\rangle + e^{-i\phi} |1\rangle)/\sqrt{2}$ , to  $|1\rangle$  (up to a global phase) if  $\phi + \phi_1 = \pi/2$ . Scanning the laser phase  $\phi_1$ , and thereby changing the phase relation  $\phi + \phi_1$  in a controlled way, gives rise to oscillations in the excitation probability  $p_1$  following a  $\cos^2$  curve between  $p_1 = 0$  and  $p_1 = 1$ ,

$$p_1(\phi_1) = \langle \psi | \hat{R}_{x,y}^\dagger(\pi/2, \phi_1) \hat{M}_1^\dagger \hat{M}_1 \hat{R}_{x,y}(\pi/2, \phi_1) | \psi \rangle = \cos^2 \left( \frac{1}{2}(\phi + \phi_1) - \frac{\pi}{4} \right), \tag{3.32}$$

where  $\hat{M}_1 = |1\rangle \langle 1|$  is a projector.

Phase fluctuations of the laser, however, disrupt the phase relation between the qubit and the

### 3. Laser Physics

laser in an uncontrolled way, leading to damped oscillations of the excitation probability when scanning  $\phi_1$  [58]. The damping of oscillations can be quantified by introducing the *Ramsey contrast*  $C$ . To obtain a value for the Ramsey contrast, the data points of the excitation probability  $p_1$  for different chosen laser phases  $\phi_1$  are fitted by a function of the type Eq. (3.32), with a constant added. This constant additionally takes oscillation damping into account. The amplitude of the oscillating fit function then yields the contrast. Oscillations between 0 and 1 mean a full contrast of  $C = 1$ , while the contrast of damped oscillations is reduced. The longer the waiting time  $\tau$ , the more phase fluctuations can happen in the laser light. A plot of  $C$  versus  $\tau$  shows a decay in contrast. If the phase relation  $\phi + \phi_1$  stays constant within a measurement of  $p_1$  at a chosen laser phase  $\phi_1$ , but changes for the next measurement of  $p_1$  at another chosen laser phase, the fluctuations are said to be slow [23]. In the case of such slow fluctuations, the contrast as a function of the free evolution time is described by [58]

$$C(\tau) = \exp\left(-\frac{(\pi\nu_a\tau)^2}{4 \ln(2)}\right), \quad (3.33)$$

where  $\nu_a$  is a frequency. The *coherence time*  $\tau_c$  of the system can be extracted as the time when the contrast has decayed to a fraction  $1/e$  of its initial value. The frequency in Eq. (3.33) can then be associated with the coherence time,

$$\nu_a = \frac{\sqrt{4 \ln(2)}}{\pi \tau_c}. \quad (3.34)$$

The frequency  $\nu_a$  can be interpreted as the laser linewidth if no magnetic field noise is present. Magnetic field noise can change the energy differences between the ion's Zeeman levels and thus introduce fluctuations in the state evolution. To extract the laser phase fluctuations from the Ramsey contrast, two different electric quadrupole transitions at 729 nm that respond differently to magnetic field noise can be examined by Ramsey experiments. Assuming that the laser frequency and the magnetic field are described by independent Gaussian variables, the frequency  $\nu_a$  is related to the laser linewidth (FWHM)  $\Delta\nu$  and the magnetic field fluctuations  $\Delta B$ ,

$$\nu_a^2 = \Delta\nu^2 + (\kappa \Delta B)^2. \quad (3.35)$$

In this equation,

$$\kappa = \left| \frac{\mu_B}{h} (g_U m_U - g_L m_L) \right| \quad (3.36)$$

is the so-called sensitivity of a transition to magnetic field fluctuations. The quantity  $g_L$  is the Landé-factor of the lower level in the transition, denoted  $L$ , and  $m_L$  is the magnetic quantum number of  $L$ . The quantity  $g_U$  is the Landé-factor of the upper level in the transition, denoted  $U$ , and  $m_U$  is the magnetic quantum number of  $U$ . Further,  $\mu_B$  is the Bohr magneton and  $h$  is the Planck constant. Performing Ramsey experiments on two different transitions 1 and 2 yields the two frequencies  $\nu_{a,1}$  and  $\nu_{a,2}$ . The laser linewidth can be extracted by solving the system of two equations,

$$\Delta\nu^2 = \frac{\kappa_2^2 \nu_{a,1}^2 - \kappa_1^2 \nu_{a,2}^2}{\kappa_2^2 - \kappa_1^2}, \quad (3.37)$$

### 3.3. The Titanium:Sapphire Laser

A laser at 729 nm allows the corresponding transition to be manipulated in  $^{40}\text{Ca}^+$ . A laser system proven capable of fulfilling this requirement [61, 62] is a continuous-wave (cw) titanium-doped sapphire laser. The titanium-doped sapphire laser (also Ti:Sapphire laser or Ti:Sa laser) is a solid state laser that can emit light of multiple Watts of power over a wavelength range from about 650 nm to 1100 nm with a maximum gain at  $\sim 800$  nm. The laser's name derives from the gain medium used: A sapphire crystal (aluminium oxide,  $\text{Al}_2\text{O}_3$ ) doped with titanium  $\text{Ti}^{3+}$  ions with a concentration of about 0.2%. In Figure 3.3a, a titanium-doped sapphire crystal can be seen. In Figure 3.3b, the emission and absorption spectrum of the crystal is shown. The laser is pumped with a separate laser in the green wavelength spectrum, hence the pump light photons have more energy than the emitted light. Nowadays, Ti:Sa lasers are typically pumped by diode-pumped solid-state (DPSS) lasers that are based on neodymium-doped gain media at a wavelength of 1064 nm and frequency-doubled to 532 nm. Population inversion in the gain medium is achieved through this green laser light exciting the titanium ions. Every excited titanium ion in the gain medium displaces itself from the neighboring oxygen atoms to lower the total energy (*Jahn-Teller effect* [63]), which leads to an excitation of phonons, relaxing the ion to a vibrational ground state of the electronic excited state. This is the upper laser level, and the energy of the upper laser level depends on how far the ion is displaced from the neighboring oxygen atoms. From the upper laser level, the titanium ion de-energizes via photon emission to a vibrationally-excited level of the electronic ground state, the lower laser level. This is the lasing transition, and the emitted wavelength depends on the displacement of the titanium ion with respect to the neighboring oxygen atoms. From the vibrationally excited state of the electronic ground state, the  $\text{Ti}^{3+}$  ion relaxes into the vibrational ground state very quickly via phonon excitation. This quick de-excitation to the vibrational ground state contributes to achieving population inversion. From the vibrational ground state of the electronic ground state, the lasing cycle repeats.

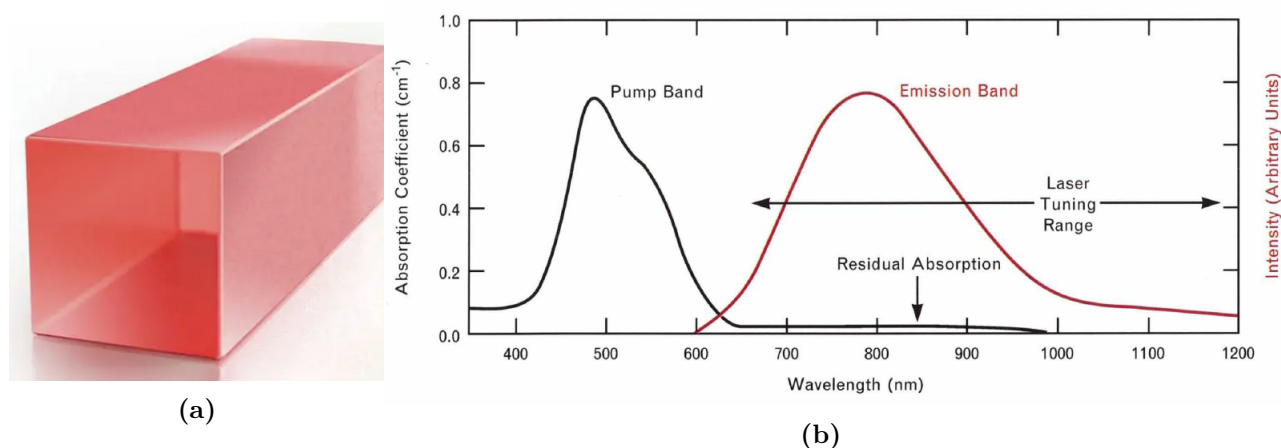


**Figure 3.3.: The gain medium of a Ti:Sa laser.** (a): An  $\text{Al}_2\text{O}_3:\text{Ti}^{3+}$  titanium-doped sapphire crystal. The approximate size of this crystal is in the  $\sim \text{cm}^3$  regime. When this crystal is put into an optical resonator consisting of two mirrors and pumped by green laser light, it starts to lase. Image taken from [64].

(b): Emission and pump absorption spectra of  $\text{Al}_2\text{O}_3:\text{Ti}^{3+}$ . The absorption and emission bands are not overlapping for the most part, so absorption of emitted photons by the crystal is avoided. Image taken from [62].

# 4. The Pound-Drever-Hall Locking Technique

In 1983, Drever *et al.* presented a method to phase- and frequency-stabilize a laser that is known contemporarily as the *Pound-Drever-Hall (PDH) Locking Technique* [32]. The PDH technique uses an optical cavity as a frequency reference. Laser light sent to the optical cavity is phase-modulated and the light reflected by the cavity is recorded by a photodiode. Following standard control techniques, an error signal is created from the photodiode signal and given to a controller. The controller creates a correction signal that is fed back to elements that control the laser frequency. The goal of this feedback loop is to reduce the laser linewidth. In Section 4.1, the principles of control theory in general, and more specifically when working with a PID-controller, are given. Section 4.2 presents how an optical cavity can be used as a frequency reference. Section 4.3 presents a motivation of the PDH technique and a derivation of the error signal. The section closes by discussing different limitations of the PDH technique to reduce a laser's linewidth.

## 4.1. Control Theory

Control is sometimes referred to as a hidden technology [65]. Feedback control can be found in a variety of applications in science and technology, but it seems to be out of sight for the most part. Historical applications include the incubator, the float valve for controlling the flow of a liquid or the fly-ball governor that was used for windmills or steam engines. Nowadays, feedback control is also used in thermostats, automated processes and aerospace engineering just to name a few important applications. Next to technical applications, feedback control plays a crucial role in living beings, most notably the human body. By using the same principles of control theory that govern the dynamics of the aforementioned systems, a laser can be frequency-stabilized to a reference cavity. In this section the general theory behind feedback control is explained. The section uses [65] and [66] as principle references.

### 4.1.1. Principles of control theory

Figure 4.1 shows a feedback loop for a physical system depicted as a block diagram. Feedback control is used when an *output signal*  $y(t)$  that describes the physical system's *process* is meant to follow a desired quantity, the *input signal* or *reference*  $w(t)$ . The goal is that the output signal  $y(t)$  follows the reference  $w(t)$  as closely as possible. This goal has to be achieved under the influence of a disturbance  $d(t)$  that is present in the feedback loop. To achieve that  $y(t)$  follows  $w(t)$  as close as possible, the value  $y(t)$  is measured by a *sensor* and compared to  $w(t)$  to create the *error signal*  $e(t) = w(t) - y(t)$ . The error signal is given to a *controller* with an internal function  $g(t)$  that creates a correction signal  $u(t)$ . The correction signal is fed back to the *plant* that consists of the *actuator* and the process. Similar to the

#### 4. The Pound-Drever-Hall Locking Technique

controller, the actuator has a characteristic function  $s(t)$  that describes its behavior. The actuator works on the process in a way that is determined by  $u(t)$ , so that the output signal changes from  $y(t)$  ideally back to  $w(t)$ . If a physical system is designed to hold an output constant (the reference is a constant) in spite of a disturbance, it is called a *regulator*. If the system is designed to follow a reference signal that is changing its value over time, it is called a *servo*. Now, feedback control is introduced more rigorously, but the rest of this Section 4.1 is not needed to understand the experimental results of this thesis in Chapter 6 and Chapter 7. However, for the reader who is new to control theory, this section is recommended to understand why and how feedback control and thus the PDH technique works. The rest of Section 4.1 is also necessary to understand the Appendix Chapters C and D.

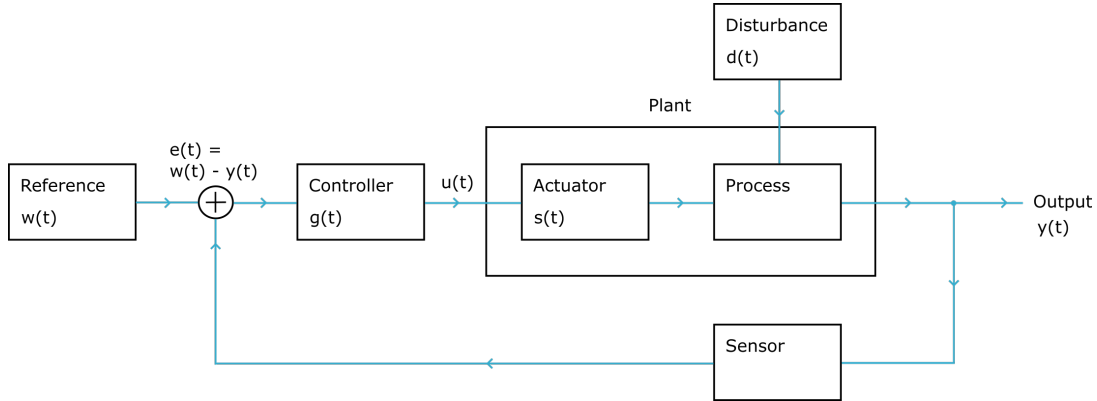


**Figure 4.1.: Sketch of a feedback loop in a block diagram.** Arrows indicate signal flow. The quantity  $w(t)$  is the input signal or reference,  $y(t)$  is the output signal,  $e(t)$  is the error signal,  $g(t)$  is a function that describes the controller behavior,  $u(t)$  is the correction signal,  $s(t)$  is a function that describes the actuator behavior and  $d(t)$  is a disturbance.

First, the impulse response  $h(t)$  has to be introduced. If a Dirac delta function is chosen as  $w(t)$ , then  $h(t)$  is the output of the physical system as a specific case of  $y(t)$ . For an arbitrary input signal  $w(t)$ , the convolution with  $h(t)$  gives the output signal,

$$y(t) = \int_{-\infty}^{+\infty} w(\tau)h(t - \tau)d\tau = w(t) * h(t). \quad (4.1)$$

According to the convolution theorem [65], the solution for the output signal takes an easier form in the frequency picture after a Laplace transformation,

$$Y(s) = W(s) \cdot H(s) \quad (4.2)$$

where in this thesis  $s = 2\pi i\nu$  with frequency  $\nu$ . The quantity  $H(s)$  is called the *transfer function* of the physical system. Instead of regarding the reference  $w(t)$ , the same approach with the impulse response can be used for an input from the disturbance  $d(t)$ , leading to a different transfer function,

$$Y(s) = D(s) \cdot H'(s). \quad (4.3)$$

Block diagram algebra has two fundamental rules [65]: The functions of two blocks in series are multiplied in the frequency picture, while the functions of two parallel blocks are added in the frequency picture. From these rules it follows that in the block diagram in Figure 4.1, the controller and the plant create the functions [66]

#### 4. The Pound-Drever-Hall Locking Technique

$$\begin{aligned} U(s) &= G(s) \cdot E(s) = G(s) \cdot (W(s) - Y(s)) \\ Y(s) &= S(s) \cdot (U(s) + D(s)). \end{aligned} \quad (4.4)$$

In these two equations,  $G(s)$  is the controller transfer function and  $S(s)$  is the actuator transfer function. Combining the two equations in Eq. (4.4) shows that

$$\begin{aligned} H(s) &= \frac{\partial Y(s)}{\partial W(s)} = \frac{G(s)S(s)}{1 + G(s)S(s)}, \\ H'(s) &= \frac{\partial Y(s)}{\partial D(s)} = \frac{S(s)}{1 + G(s)S(s)}. \end{aligned} \quad (4.5)$$

The first line in the equation array shows how well the system can track the input function. The second line gives the system's ability to cancel a disturbance. If the system has a constant reference signal  $w(t) = w$ , an investigation of the second equation is of more importance. The behavior of the output signal  $y(t)$  in time due to a disturbance  $d(t)$  can then be calculated by back-transforming  $Y(s)$  in Eq. (4.3) into the time picture. The actuator transfer function  $S(s)$  is usually given by the physical system, for example when the plant includes a filter, a Piezo mirror, an acousto-optic modulator or an electro-optic modulator as an actuator. The controller transfer function  $G(s)$ , however, can be adjusted to meet the requirements imposed by the disturbance  $d(t)$ , so that the goal of  $y(t)$  following  $w(t)$  as close as possible can be achieved. In the following subsection, possible adjustments for  $G(s)$  will be discussed.

#### 4.1.2. PID control

The most straightforward way to set a controller is by *proportional gain*. A controller that includes a proportional gain is called a P-controller. Here, the correction signal  $u(t)$  is linearly proportional to the error signal  $e(t)$ ,

$$u(t) = k_P e(t) = k_P (w(t) - y(t)), \quad (4.6)$$

where  $k_P$  is the proportional gain. It is important to note that  $y(t)$  is subtracted from  $w(t)$ , which introduces negative feedback: Ideally,  $e(t) = 0$ , which means no error. If  $y(t) > w(t)$ ,  $u(t)$  is negative and it will thus reduce the value of  $y(t)$  in the next feedback lap, bringing  $e(t)$  closer to 0. If  $y(t) < w(t)$  the opposite happens, but  $e(t)$  is still being brought closer to 0. After a Laplace transformation, Eq. (4.6) can be rewritten as

$$\frac{U(s)}{E(s)} = G_P(s) = k_P. \quad (4.7)$$

The main disadvantage of the proportional gain is the *steady-state error* [65], where the output signal  $y(t)$  will stay at a constant value from  $w(t)$  after a disturbance  $d(t)$  has influenced the physical system's behavior. A simulation of a P-controller's response to a step disturbance can be seen in the Appendix Chapter D. To overcome this limitation for a P-controller, an integral I-part is introduced,

$$u(t) = k_I \int_{t_0}^t e(\tau) d\tau. \quad (4.8)$$

In the frequency picture, the controller transfer function  $U(s)/E(s)$  reads

#### 4. The Pound-Drever-Hall Locking Technique

$$G_I(s) = \frac{k_I}{s} \quad (4.9)$$

by using the integration theorem for Laplace transformations. The integral part sums up the error signal  $e(t)$  from the starting time  $t_0$ . If  $y(t) < w(t)$ , the value of  $u(t)$  increases, if  $y(t) > w(t)$  the value decreases. Adding an I-part to a P-controller, rendering it a PI-controller, removes the steady state error. However, another disadvantage arises as an integral part introduces overshooting [65], where the output signal  $y(t)$  is too much corrected for and  $w(t) - y(t)$  flips sign instead of staying at 0. In Appendix Chapter D, a simulation of a PI-controller's response to a step disturbance is shown. To reduce overshooting, a derivative or D-part is introduced. The correction function for the D-part reads

$$u(t) = k_D \frac{d}{dt} e(t), \quad (4.10)$$

and after a Laplace transformation the controller transfer function reads

$$G_D(s) = k_D \cdot s \quad (4.11)$$

with the help of the derivative theorem. A derivative part slows the speed at which  $y(t)$  approaches  $w(t)$ . On the other hand, it can give a sharp response to suddenly changing signals. Adding the D-part to the PI-controller yields a PID-controller. For a PID-controller, the combined controller transfer function is

$$G_{PID}(s) = k_P + \frac{k_I}{s} + k_D \cdot s. \quad (4.12)$$

In Appendix Chapter D, a simulation of a PID-controller's response to a step disturbance is shown. The art of control theory is how to find adequate PID parameters  $k_P$ ,  $k_I$  and  $k_D$  so that  $y(t)$  is following  $w(t)$  as close as possible under the given circumstances in the physical system. Several methods to find adequate PID parameters can be found e.g., in [65].

## 4.2. An Optical Cavity as a Frequency Reference

An optical cavity is a resonator for electromagnetic radiation. For two mirrors separated in distance by  $L$ , Eq. (3.3) provides the conditions on the mirror radii of curvature for the resonator stability criterion. The radiation field that builds up inside a stable resonator is a solution of the paraxial Helmholtz equation and is thus described by Gaussian modes, Eq. (3.4). This section will describe how an optical cavity (or just "cavity") can be used as a frequency reference.

The spatial extent of a standing wave is an integer number times half the wavelength  $\lambda$ . It follows that the frequency separation between two longitudinal modes in a cavity is [48]

$$\Delta\nu_{\text{FSR}} = \frac{c}{2nL}, \quad (4.13)$$

where in the above equation,  $n$  is the index of refraction of the material inbetween the cavity mirrors. The frequency spacing in Eq. (4.13) is known as the *free spectral range*. In many applications the cavity is evacuated so that  $n \rightarrow 1$ .

In the following, a model is derived for the linewidth and spectral lineshape of a cavity. Before this model is extended to an arbitrary cavity geometry, it suffices to look at the

#### 4. The Pound-Drever-Hall Locking Technique

behavior of an electric field that is incident on a *Fabry-Perot étalon*: Two semi-transparent planar mirrors separated by  $L$ . The word “*étalon*” is French and means “calibration spacer” or “gauge” [48], already indicating the use of optical cavities as frequency references. An electric field of the type Eq. (2.32) is incident on a Fabry-Perot étalon as is shown in Figure 4.2. The electric field can either be reflected, transmitted, absorbed or scattered by the cavity. In the coming derivation, losses through absorption and scattering are neglected (for now). The reflection amplitude  $r$  indicates the fraction of the incident electric field  $E_i$  that is reflected, the transmission amplitude  $t$  indicates how much is transmitted. It is further assumed that for both mirrors the values of  $r$  and  $t$  are the same. The electric field that is reflected at incidence on the first mirror is [48]

$$E_{r1} = E_i r e^{i\pi} = -E_i r. \quad (4.14)$$

The factor  $e^{i\pi}$  appears because a wave experiences a phase shift of  $\pi$  upon reflection at the surface on an optically denser medium. The transmitted electric field is either reflected or transmitted through the second mirror. When traveling the distance between the mirrors, the electric field accumulates the phase  $e^{2\pi i L/\lambda}$ . When the field is reflected, there is a chance of another reflection or of transmission. Considering all possible events for the electric field to be reflected, the total reflected electric field can be written as

$$\begin{aligned} E_r &= -E_i r + E_i t^2 r e^{4\pi i L/\lambda} \sum_{j=2}^{\infty} \left( r^2 e^{4\pi i L/\lambda} \right)^{j-2} \\ &= -E_i r + E_i t^2 r e^{4\pi i L/\lambda} \frac{1}{1 - r^2 e^{4\pi i L/\lambda}}. \end{aligned} \quad (4.15)$$

In the upper line of the equation, the term in front of the sum  $\Sigma$  accounts for one reflection at the second mirror and the sum for additional reflections inside the étalon. In the second line, the sum is rewritten as the result of a geometric series. The cavity reflection signal  $\mathcal{R}(\nu)$ , the ratio of the reflected and the incident electric field, reads

$$\mathcal{R}(\nu) = \frac{E_r}{E_i} = \frac{r(e^{4\pi i L/\lambda} - 1)}{1 - r^2 e^{4\pi i L/\lambda}} = \frac{r(e^{2\pi i \nu / \Delta\nu_{\text{FSR}}} - 1)}{1 - r^2 e^{2\pi i \nu / \Delta\nu_{\text{FSR}}}}. \quad (4.16)$$

Here, the identities for the reflection and transmission coefficients  $r^2 = R$ ,  $t^2 = T$  and  $R + T = 1$  were used, such that  $t^2 = 1 - r^2$ .

The intensity of a light field is calculated by Eq. (3.11), so that the ratio of the reflected to incident intensity is

$$\frac{I_r}{I_i} = |\mathcal{R}(\nu)|^2 = \frac{\mathcal{F} \sin^2(\pi \nu / \Delta\nu_{\text{FSR}})}{1 + \mathcal{F} \sin^2(\pi \nu / \Delta\nu_{\text{FSR}})} \quad (4.17)$$

where

$$\mathcal{F} = \frac{4r^2}{(1 - r^2)^2}. \quad (4.18)$$

If the frequency  $\nu$  is an integer multiple  $N$  of the free spectral range,  $\nu = N \cdot \Delta\nu_{\text{FSR}}$ , the reflection signal  $\mathcal{R}(\nu)$  is 0. If  $\nu$  approaches  $N \cdot \Delta\nu_{\text{FSR}}$ , Eq. (4.17) can be approximated by

$$|\mathcal{R}(\nu)|^2 \sim \frac{\mathcal{F} \pi \left( \frac{\nu}{\Delta\nu_{\text{FSR}}} \right)^2}{1 + \mathcal{F} \pi \left( \frac{\nu}{\Delta\nu_{\text{FSR}}} \right)^2}. \quad (4.19)$$

#### 4. The Pound-Drever-Hall Locking Technique

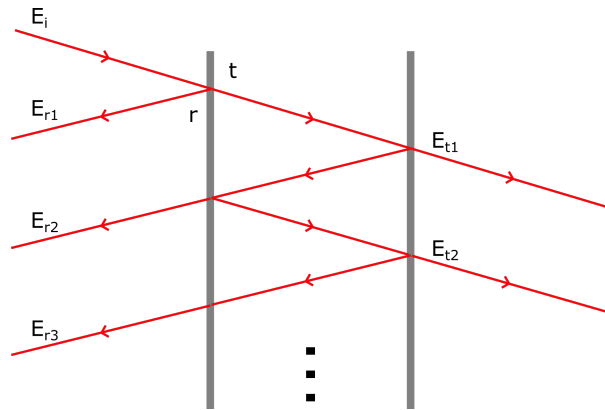


**Figure 4.2.: An electric field interacting with a Fabry-Pérot étalon.** An electric field is incident on a Fabry-Pérot étalon. The étalon consists of two planar mirrors with reflection amplitude  $r$  and transmission amplitude  $t$ . A fraction  $E_{rn}$  ( $E_{tn}$ ) of the incident electric field  $E_i$  is reflected (transmitted), where  $n \in \mathbb{N}$  denotes the  $n$ -th reflection (transmission).

From energy conservation it follows that for  $\nu$  approaching  $N \cdot \Delta\nu_{\text{FSR}}$  the cavity transmission signal is

$$|\mathcal{T}(\nu)|^2 = 1 - |\mathcal{R}(\nu)|^2 \sim \frac{1}{1 + \mathcal{F}\pi\left(\frac{\nu}{\Delta\nu_{\text{FSR}}}\right)^2}. \quad (4.20)$$

In Figure 4.3, the cavity reflection  $|\mathcal{R}(\nu)|^2$  (Eq. (4.17), not approximated) and the transmission signal  $|\mathcal{T}(\nu)|^2 = 1 - |\mathcal{R}(\nu)|^2$  (also not approximated) of a Fabry-Pérot étalon can be seen.

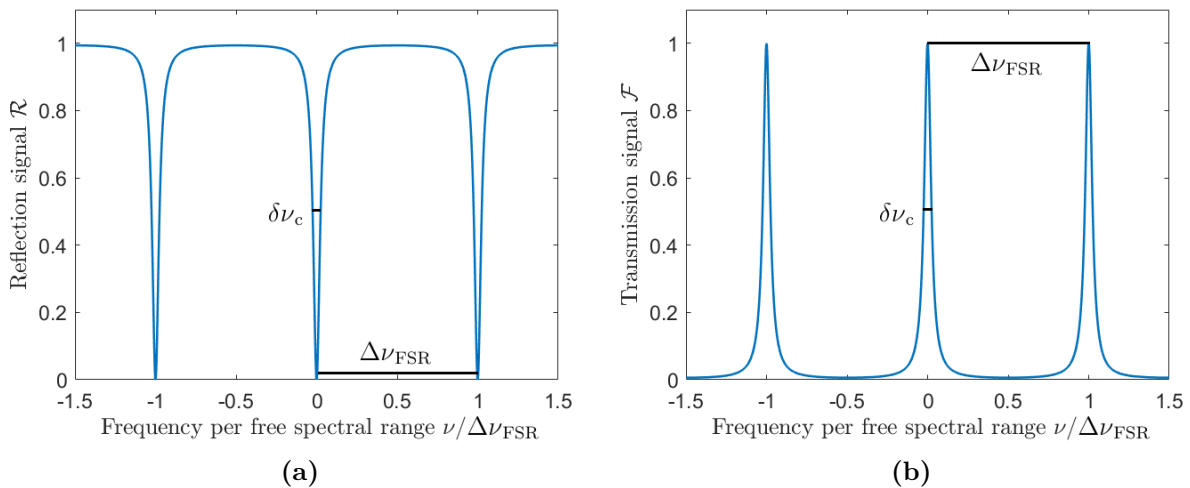


**Figure 4.3.: Reflection and transmission signal of a Fabry-Pérot étalon.** (a) Reflection and (b) transmission signal with a free spectral range of  $\Delta\nu_{\text{FSR}} = 20 \cdot \delta\nu_c$ , twenty times the cavity linewidth, yielding a Finesse of  $F = 20$ . The center frequency  $\nu = 0$  Hz is chosen to be at a cavity resonance frequency. At  $\nu = \Delta\nu_{\text{FSR}}$  from the center frequency, the next resonance takes place.

In contrast to a Fabry-Pérot étalon, the frequency spacing from one transmission peak to the next is not only given by the separation of  $\Delta\nu_{\text{FSR}}$  for an arbitrary optical cavity that consists of two semi-transparent mirrors. The frequency separation of Gaussian modes inside an arbitrary optical cavity that consists of two semi-transparent mirrors is [48]

#### 4. The Pound-Drever-Hall Locking Technique

$$\begin{aligned}\Delta\nu_{qmn} &= q\Delta\nu_{\text{FSR}} + (m+n+1)\Delta\nu_{\text{Gouy}} \\ &= q\Delta\nu_{\text{FSR}} + (m+n+1)\frac{1}{\pi}\arccos\left(\sqrt{\left(1-\frac{L}{R_1}\right)\left(1-\frac{L}{R_2}\right)}\right).\end{aligned}\quad (4.21)$$

In this equation,  $q$  is the longitudinal mode number and  $m, n$  are the indices of the transversal  $\text{TEM}_{mn}$  modes. The factor  $\Delta\nu_{\text{Gouy}}$  is the resonator Gouy frequency shift. The quantities  $R_1$  and  $R_2$  are the cavity mirrors' radii of curvature. It can be seen that for a Fabry-Perot étalon only  $\Delta\nu_{qmn} = q\Delta\nu_{\text{FSR}}$  remains. After every spacing  $\Delta\nu_{qmn}$ , a transmission peak and simultaneously a reflection dip can form.

The FWHM of the Lorentzian dip (or peak) is the *cavity linewidth*  $\delta\nu_c$ , which was already ad hoc introduced in Eq. (3.14). The *Finesse*  $F$  is defined as

$$F = \frac{\Delta\nu_{\text{FSR}}}{\delta\nu_c} = \frac{\pi}{2}\sqrt{\mathcal{F}} = \pi \cdot \frac{r}{t}. \quad (4.22)$$

The finesse is a key characterization quantity for a cavity. One interpretation of the finesse is the average number of times the electric field is reflected inside the cavity.

Up to now, losses in the electric field through absorption and scattering were neglected. If the transmission coefficients  $T_1, T_2$  and loss coefficients  $L_1, L_2$  of each cavity mirror are known, the finesse can be approximated for small losses by [52]

$$F = \frac{2\pi}{T_1 + T_2 + L_1 + L_2}. \quad (4.23)$$

Losses reduce the finesse and therefore, plugging Eq. (4.23) into Eq. (4.22), broaden the cavity linewidth.

### 4.3. The Pound-Drever-Hall (PDH) Technique

#### 4.3.1. Motivation and outline of the PDH technique

The previous section reveals that the reflected or transmitted intensity of a laser beam that is near-resonant with a cavity, within the cavity linewidth, provides information on the relative frequency difference between the laser and the resonant mode of the cavity. This can be used to frequency-stabilize (or *lock*) the laser using feedback control. Different techniques to do so have been invented so far. A broad overview of laser frequency stabilization techniques is given in [67], which is used together with [68] as a reference for this subsection.

A straightforward way to lock a laser with frequency  $\nu(t)$  to a cavity is via *side-of-fringe locking*. For this technique, the transmission signal is recorded by a photodiode which converts the light power to a frequency-dependent voltage  $V(\nu(t))$ . The frequency  $\nu(t)$  is changing over time due to disturbances, so the voltage is also time-dependent. By choosing a point at a frequency  $\nu_0$  on the slope (side) of the cavity transmission signal as a reference, an error signal is defined by  $e(\nu(t)) = V(\nu_0) - V(\nu(t))$ . The slope is necessary to introduce an asymmetry, because a larger voltage has to indicate an increase in frequency and a smaller voltage a decrease, and vice versa. Once the error signal is created by producing  $V(\nu_0)$  and subtracting  $V(\nu(t))$ , standard feedback control allows one to lock the laser to  $\nu_0$ . The simplicity of the side-of-fringe technique comes with a disadvantage. Intensity changes of the laser light lead to a change in transmission power and therefore the controller will implement

a frequency change on the laser.

Another laser locking technique is the *top-of-fringe lock*, which is further described in [68]. Here, as the name indicates, the laser is locked to the top of the transmission signal profile. The main difference to the side-of-fringe lock is that this technique does not have a natural asymmetry, as  $dV(\nu)/d\nu = 0$  on top of the transmission peak. So, a sinusoidal modulation of the laser frequency  $\nu(t)$  is created with a frequency  $\nu_d$  around the peak center frequency  $\nu_0$ . This modulation is also called a *dither*. The error signal is then extracted from the Fourier component of  $V(\nu(t))$  at the dither frequency  $\nu_d$ . Then,  $e(\nu_0) = 0$  and  $dV(\nu)/d\nu \neq 0$  at  $\nu = \nu_0$ . As the error signal depends on the change of  $V(\nu(t))$  with frequency and thus on the derivative  $dV(\nu)/d\nu$ , the laser frequency is mostly insensitive to intensity changes of the laser light. However, the main drawback of the top-of-fringe lock is that it can only correct for frequencies that are much less than the dither frequency  $\nu_d$ , which in turn has to be much less than the cavity linewidth. For laser stabilization applications that require a narrow linewidth, the highest frequency the feedback loop can correct for might be too low. The Pound-Drever-Hall (PDH) technique or PDH lock is similar to the top-of-fringe technique, but allows for correction at much higher frequencies. To do so, the PDH technique uses the cavity reflection signal, and the cavity-incident laser light is phase modulated at a frequency  $\Omega$  which is much higher than the cavity linewidth. In Figure 4.4, a minimal optical and electronic setup to realize the PDH locking technique is depicted, which assumes the laser light to be linearly polarized. A function generator produces a voltage oscillating at frequency  $\Omega$ . The phase modulation at this frequency  $\Omega$  is then done via an electro-optic modulator (EOM). If the laser is not exactly on resonance with the cavity, light is reflected. After passing a quarter-wave plate twice, the reflected light is reflected at a polarizing beam splitter. The reflected laser light is incident on a photodiode, where the laser power is converted to an electric current. The current passes a low-pass filter that removes the Fourier components oscillating at twice the modulation frequency or above. Then, the error signal  $e(t)$  is created by mixing the filtered photodiode signal with the modulation signal from the function generator. The error signal passes a low-pass filter, which removes the Fourier component that includes twice the modulation frequency because of the mixer. The error signal is then sent to a PID controller that creates the correction signal. The correction signal is transformed to a suitable voltage for the laser frequency actuators by a laser control device and finally given back to the laser, closing the feedback loop. In the next subsection, a summarized mathematical derivation of the PDH error signal  $e(t)$  is shown. In the Appendix Chapter A, a step-by-step derivation of the error signal is given.

### 4.3.2. Summarized derivation of the PDH error signal

This subsection was developed based on the references [32] and [69]. The cavity-incident electric field may be described in a complex form,  $E_0 e^{2\pi\nu it}$ . After phase modulation by the EOM at a frequency  $\Omega$ , the cavity-incident electric field reads

$$E_i = E_0 e^{i(2\pi\nu t + \beta \sin(2\pi\Omega t))}, \quad (4.24)$$

where  $\beta$  is the modulation index. This expression can be expanded into a series of Bessel functions  $J_n(\beta)$  [70]. If the peak phase deviation, the modulation index  $\beta$ , is  $< 1$  or close to 1, Eq. (4.24) can be approximately rewritten as

$$E_i \sim E_0 e^{2\pi\nu it} \cdot \left( J_0(\beta) + J_1(\beta) e^{2\pi\Omega it} - J_1(\beta) e^{-2\pi\Omega it} \right). \quad (4.25)$$

#### 4. The Pound-Drever-Hall Locking Technique

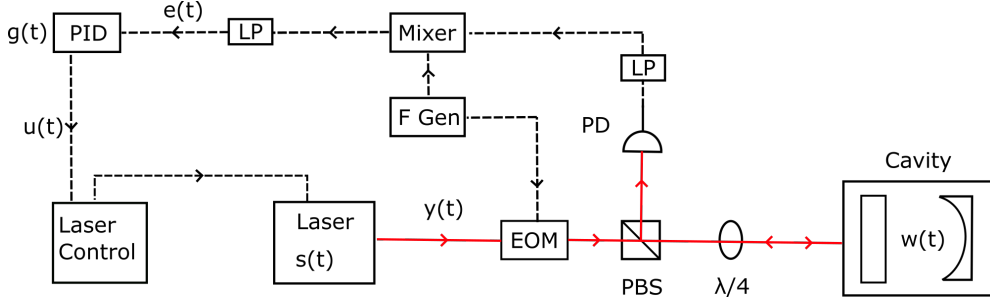


**Figure 4.4.: A minimal laser locking setup for the PDH technique.** In this setup, it is assumed that the output laser light is linearly polarized. The cavity gives a reference frequency as the reference signal  $w(t)$ . The output laser frequency is  $y(t)$ . The error signal  $e(t)$  is given to the controller, whose response is described by  $g(t)$ . From there, the correction signal  $u(t)$  is given to the actuator in the laser, whose response is described by  $s(t)$ . Red lines indicate laser light and dashed black lines indicate electrical connections. Arrows indicate the direction of light resp. electrical signal propagation. EOM: Electro-optic modulator, PBS: polarizing beam splitter,  $\lambda/4$ : quarter-wave plate, PD: photodiode, F Gen: function generator (local oscillator), LP: low-pass filter, PID: PID-controller.

So, the modulated cavity-incident electric field can be regarded as three different frequency components in superposition, one at the *carrier* frequency  $\nu$  and two at the *sideband* frequencies  $\nu \pm \Omega$ , respectively. After reflection of the modulated field of Eq. (4.25) from a cavity, the electric field can be calculated using Eq. (4.16):

$$E_r = E_0 e^{2\pi i \nu t} \left( \mathcal{R}(\nu) J_0(\beta) + \mathcal{R}(\nu + \Omega) J_1(\beta) e^{2\pi i \Omega t} - \mathcal{R}(\nu - \Omega) J_1(\beta) e^{-2\pi i \Omega t} \right). \quad (4.26)$$

The power measured by the photodiode (Figure 4.4) is, according to Eq. (3.13),

$$\begin{aligned} P_r &= P_C |\mathcal{R}(\nu)|^2 + P_S |\mathcal{R}(\nu + \Omega)|^2 + P_S |\mathcal{R}(\nu - \Omega)|^2 \\ &+ 2\sqrt{P_C P_S} \left( \text{Re} \left\{ \mathcal{R}(\nu) \mathcal{R}^*(\nu + \Omega) - \mathcal{R}^*(\nu) \mathcal{R}(\nu - \Omega) \right\} \cos(2\pi \Omega t) \right. \\ &\left. - \text{Im} \left\{ \mathcal{R}(\nu) \mathcal{R}^*(\nu + \Omega) - \mathcal{R}^*(\nu) \mathcal{R}(\nu - \Omega) \right\} \sin(2\pi \Omega t) \right) + 2\Omega \text{ terms..} \end{aligned} \quad (4.27)$$

In this equation,  $P_C = J_0^2(\beta) P_0$  is the fraction of the total power  $P_0$  in the carrier and  $P_S = J_1^2(\beta) P_0$  is the fraction in each sideband. The terms oscillating at  $2\Omega$  can be neglected as they are removed by the first low-pass filter in the PDH lock setup (Figure 4.4). The real and imaginary parts of  $\mathcal{R}(\nu) \mathcal{R}^*(\nu + \Omega) - \mathcal{R}^*(\nu) \mathcal{R}(\nu - \Omega)$  are asymmetric in frequency around  $\nu = N \cdot \Delta\nu_{\text{FSR}}$ , which gives the asymmetry that is needed for the error signal. For modulation frequencies that are much higher than the cavity linewidth the factor  $\mathcal{R}(\nu) \mathcal{R}^*(\nu + \Omega) - \mathcal{R}^*(\nu) \mathcal{R}(\nu - \Omega)$  becomes purely imaginary, and so only the  $\sin(2\pi \Omega t)$  term survives in Eq. (4.27), while the  $\cos(2\pi \Omega t)$  term vanishes.

The mixer in Figure 4.4 creates a product of two input signals. One input signal at a frequency  $\Omega$  comes from the photodiode after the first low-pass filter and the other from the local oscillator (function generator F Gen in Figure 4.4) at a frequency  $\Omega'$  (for now, allow  $\Omega'$  not equal to  $\Omega$ ). The second low-pass filter in Figure 4.4 removes the term oscillating at  $\Omega + \Omega'$  after the mixer, so that only the term oscillating at  $\Omega - \Omega'$  remains. In the case of the PDH technique  $\Omega - \Omega' = 0$  so that the error signal after the second low-pass filter reads

$$e(\nu) = -\sqrt{P_C P_S} \text{Im} \left\{ \mathcal{R}(\nu) \mathcal{R}^*(\nu + \Omega) - \mathcal{R}^*(\nu) \mathcal{R}(\nu - \Omega) \right\} \cdot \cos(\phi). \quad (4.28)$$

The phase  $\phi$  stands for the relative phase between the two sinusoidal signals going into the

#### 4. The Pound-Drever-Hall Locking Technique

mixer. In Figure 4.5, the error signal for a lossless cavity with identical mirrors and  $\phi = 0$  is depicted. In case  $\phi = \pi/2$ , no error signal would be created, as can be seen in Eq. (4.28), and a phase close to  $\pi/2$  reduces the amplitude of the error signal. It is therefore important to set the relative phase near  $n \cdot \pi$  with  $n \in \mathbb{N}$ . However it has to be further considered that a phase change from 0 to  $\pi$  would invert the signal in Figure 4.5. The controller has to be informed about a change in phase of  $\pi$ , otherwise it has the wrong polarity and the negative feedback loop turns into a positive feedback loop: The controller works with full force against locking the laser. A change of the relative phase  $\phi$  can be achieved by a phase-shifter device, by adjusting cable lengths from either the function generator to the EOM or the function generator to the mixer, or by changing the modulation frequency  $\Omega$  for given cable lengths. When the laser is locked, the laser frequency is kept close to the cavity resonance frequency, within the cavity linewidth. For a modulation frequency that is by orders of magnitude higher than the cavity linewidth, the sidebands are totally reflected so that  $\mathcal{R}(\nu \pm \Omega) = -1$ . The cavity reflection signal in Eq. (4.16) contains a factor  $2\pi\nu/\Delta\nu_{\text{FSR}}$  that is an integer multiple  $N$  of  $2\pi$  on resonance. When a time-dependent frequency disturbance  $\delta\nu(t)$  is introduced for which  $\delta\nu(t) \ll \Delta\nu_{\text{FSR}}$  holds, then that factor can be approximated by

$$\frac{2\pi\nu(t)}{\Delta\nu_{\text{FSR}}} \sim 2\pi N + \frac{2\pi\delta\nu(t)}{\Delta\nu_{\text{FSR}}}. \quad (4.29)$$

Substitution of Eq. (4.29) into Eq. (4.16) yields the carrier reflection signal

$$\mathcal{R}(\delta\nu(t)) = \frac{r}{1-r^2} \cdot \frac{2\pi i \delta\nu(t)}{\Delta\nu_{\text{FSR}}} = \frac{2iF\delta\nu(t)}{\Delta\nu_{\text{FSR}}} \quad (4.30)$$

where  $\exp(x) \sim 1+x$  for  $x$  small and the expression for the finesse in Eq. (4.22) have been used. Near resonance, the reflected power can thus be approximated to be proportional to

$$P_r \propto 2P_S - 8\sqrt{P_C P_S} \frac{F\delta\nu(t)}{\Delta\nu_{\text{FSR}}} \sin(2\pi\Omega t). \quad (4.31)$$

The error signal after the mixer and the second low-pass filter in Figure 4.4 (assuming  $\phi = 0$ ) is thus linearly dependent on time-dependent frequency fluctuations,

$$e(\delta\nu(t)) = -4\sqrt{P_C P_S} \frac{F\delta\nu(t)}{\Delta\nu_{\text{FSR}}} = D \cdot \delta\nu(t) \quad (4.32)$$

where the constant  $D$  is known as the *frequency discriminant*. This discriminant can be maximized when the modulation index is chosen as  $\beta = 1.08$ , so that  $P_S = 0.42 P_C$  [69]. The error signal is then given to the controller that creates the correction signal  $u(t)$ . The correction signal is sent back to the laser system, closing the feedback loop.

#### Limitations in frequency stabilization when using the PDH technique

A perfectly locked laser ( $\delta\nu(t) = 0$ ) produces a zero valued error signal ( $e(t) = 0$ ). However, zero frequency fluctuations are impossible to reach as this value is fundamentally lower-bounded by photoelectric shot noise. Light falls on the photodetector as a discrete number of photons. As a result, an electric signal produced by the photodiode shows shot noise that cannot be distinguished from a current due to a frequency fluctuation of the laser light. For

#### 4. The Pound-Drever-Hall Locking Technique

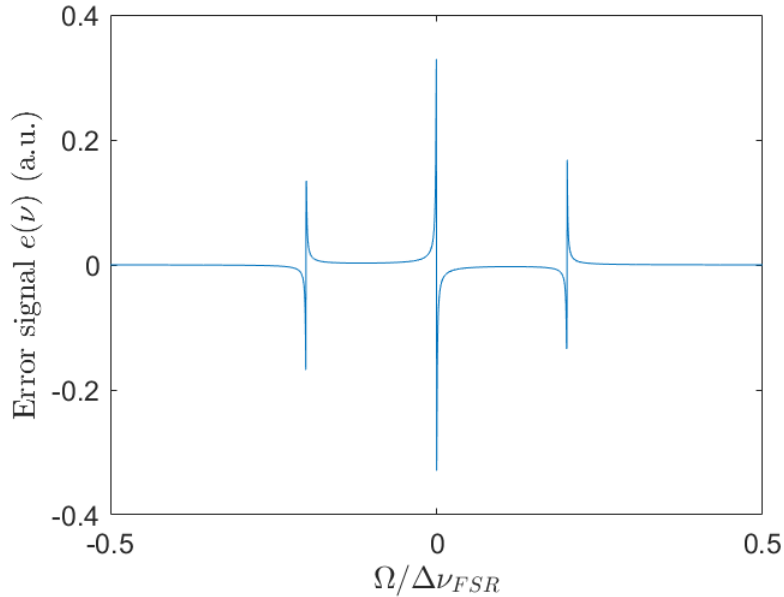


**Figure 4.5.: Pound-Drever-Hall error signal.** The signal is calculated by Eq. 4.28. The chosen parameters are: The modulation frequency  $\Omega$  is 20% of the free spectral range  $\Delta\nu_{\text{FSR}}$ ,  $\Omega/\Delta\nu_{\text{FSR}} = 0.2$ , cavity reflection amplitude  $r = 0.999$ , total power  $P_0 = 1$  a.u., modulation index  $\beta = 1.08$ . The sidebands are at  $\Omega = 0.2 \cdot \Delta\nu_{\text{FSR}}$  from the carrier frequency. The phase is  $\phi = 0$  and the cavity is assumed to be lossless. In Appendix Chapter B, the PDH error signal that was recorded in our laboratory is presented.

an average measurement time of  $\tau$ , the linewidth (FWHM) of the laser locked by the PDH technique due to the photoelectric shot noise is given by [32]

$$\delta\nu(\tau) = \delta\nu_c \sqrt{\frac{h\nu}{\tau P_0(1-r^2)\eta}} \quad (4.33)$$

where  $h$  is the Planck constant and  $\eta$  is the photodiode's quantum efficiency. The quantum efficiency of a photodiode is given by

$$\eta = R \cdot \frac{h\nu}{e} = \frac{I_{\text{ph}}h\nu}{P_{\text{r,in}}e} \quad (4.34)$$

where  $R$  is the so-called responsivity,  $I_{\text{ph}}$  is the photocurrent and  $P_{\text{r,in}}$  is the incident power on the photodiode (reflected by the cavity). The quantity  $e$  is the amplitude of the elementary charge.

Another issue arises from changes in cavity length. Recall that two standing waves in a Fabry-Perot étalon are separated in frequency by  $\Delta\nu_{\text{FSR}}$  (Eq. (4.13)). A cavity length change  $\delta L$  causes a change in the free spectral range  $\delta(\Delta\nu_{\text{FSR}})$  according to the relation

$$\delta(\Delta\nu_{\text{FSR}}) = \frac{1}{2} \frac{c}{\delta L}. \quad (4.35)$$

where  $c$  is the speed of light in vacuum. The PDH error signal of Eq. (4.32) cannot distinguish between a change in laser frequency or free spectral range in the cavity. So, in response to a change in  $\Delta\nu_{\text{FSR}}$ , the controller assumes that a laser frequency fluctuation has happened and corrects for it. Time-dependent changes in cavity length can arise for different reasons. First, mechanical vibrations on the cavity lead to an oscillation in cavity length. Vibrational

#### 4. *The Pound-Drever-Hall Locking Technique*

stabilization of the reference cavity can be implemented to mitigate mechanical vibrations. Second, fluctuations in laser intensity change the cavity length through fluctuations in light pressure on the mirrors [71]. A laser intensity stabilization feedback loop can be installed to reduce this effect. In Subsection 5.3.2, one way to set up an intensity stabilization feedback loop is shown. Third, temperature changes of the cavity through the laser or the environment can change the cavity length. Temperature stabilization of the cavity can help to reduce this effect. Finally, optical cavities built from ultra-low expansion (ULE) glass are slowly increasing in length on a timescale of months to years [72], leading to a persistent drift in the reference frequency.

# 5. The Experimental Setup

The master’s project involved setting up a Titanium-Doped Sapphire laser system emitting light at 729 nm and stabilizing its frequency to an external reference cavity via the PDH technique to a linewidth below 10 Hz. One additional requirement for the laser was that once it is locked, it should stay locked over the course of several days. In this chapter, the key parts of the experimental setup are presented. In Section 5.1, the laser model, control and specifications are described. In Section 5.2, the characteristics of the reference cavity are presented. The laser stabilization setup and connections are then presented in Section 5.3. During the master project, our team and the entire laboratory equipment switched buildings from the Institute of Quantum Optics and Quantum Information (IQOQI) in Innsbruck to the Viktor-Franz-Hess building, first floor, University of Innsbruck (UIBK). Section 5.4 describes the development of the experimental setup over time and the move.

## 5.1. The MSquared SolsTiS and Equinox Lasers

The British company *MSquared Lasers* offers a cw titanium sapphire laser under the product name *SolsTiS* [73]. The *SolsTiS SA PSX R* model was chosen as the qubit laser. In Table 5.1, the laser’s output characteristics as stated by MSquared are shown. The laser’s free-running linewidth is given as 100 kHz over 100  $\mu$ s. To achieve a laser linewidth towards 1 Hz over 1 s, we frequency-stabilized the laser to an external reference cavity via the PDH technique. From now on, the laser system will be referred to as the “new Ti:Sa laser”.

MSquared Lasers also provides the 532 nm pump laser for the SolsTiS model, called the *Equinox*. This DPSS laser can produce up to 10 W of optical power at 532 nm. When ordering the SolsTiS and Equinox in combination, pump and Ti:Sa are delivered on one shared base plate. Two screws allow for alignment of the Equinox beam into the SolsTiS laser resonator. The new Ti:Sa laser was switched on for the first time in our laboratory in March of 2021. Unfortunately, there was a problem with a diode inside the delivered Equinox, and the pump laser started to spontaneously switch off during lasing operation, starting in August 2021. It was then not possible to switch the Equinox laser back on again without an MSquared employee remotely fixing the issue first. As a consequence, the entire laser system had to be returned to MSquared in September 2021 and arrived back at the laboratory again in December 2021 with the problem fixed.

The first subsection includes an overview on how to operate the SolsTiS and the Equinox. Then, a look into the SolsTiS laser resonator will be given.

### 5.1.1. Operating the SolsTiS and Equinox

Both the SolsTiS and the Equinox are connected to individual electronic control units, called the *ICE-BLOCs*, which are interconnected by a LAN cable. The lasers can be switched on and off directly at these control units with individual turn-keys. All connections between the lasers and their corresponding ICE-BLOCs can be found in detail in [73]. Both the SolsTiS and the Equinox are connected to one closed-loop water circuit for temperature

**Table 5.1.: Characteristics of the *SolsTiS SA PSX R* model as stated by MSquared.**

Model Name	SolsTiS SA PSX R
Output power	>2 W, >1.8 W @ 729 nm
Tuning range	725 nm - 875 nm
Linewidth	< 100 kHz @ 100 $\mu$ s
Amplitude noise	< 0.1% RMS
Spatial mode	TEM00
Polarization	horizontal
Beam radius	<0.4 mm @ $1/e^2$
Beam divergence	<1.5 mrad half angle

stabilization. The chiller used for water temperature regulation is a *SMC Thermo-Con HECR004*. The water temperature recommended by MSquared is 25 °C. The Equinox ICE-BLOC is connected to a laptop via a LAN cable from which both lasers can be controlled by searching for their IP address in a web browser. The Equinox laser can give pump laser light at a chosen power between 0 and 10 W. The SolsTiS’ lasing threshold is at approximately 4.3 W pump power and MSquared recommends to use 10 W whenever possible. It is not recommended to switch the pump laser off in order to conserve the pump laser diodes, so there is an “idle” option that puts the pump laser output down to  $\sim 0.1$  W. To completely block any laser light reaching the SolsTiS, a mechanical shutter can be manually closed. On the SolsTiS web page there are options to adjust the intracavity elements and thereby alter the output frequency. These elements will be investigated closer in the next subsection. It is possible to scan the laser frequency around a chosen value, which can be used e.g., to record a trace of the PDH error signal (Appendix Chapter B). It is recommended to put the Equinox out of idle mode and leave the whole system running for about 2 hours before it is used for any specific task, which gives the laser system enough time for thermalisation.

### 5.1.2. Elements in the SolsTiS bowtie

The SolsTiS laser resonator, gain medium and other elements are sealed in a metal box. Figure 5.1 shows a sketch of the elements inside the SolsTiS metal box in a so-called “bowtie” geometry. Together with the optical diode, this geometry prohibits the build-up of standing waves in the resonator that would lead to spectral hole burning and as a consequence to a strong unwanted fluctuation in laser output power [74].

Given the broad gain spectrum of the Ti:Sa crystal, it is possible for the laser to emit at several longitudinal modes at once. To get the laser to single-mode operation, three different elements are used in the resonator [73]. The birefringent filter (BRF) is responsible for a coarse frequency adjustment. This filter uses birefringence in combination with the Brewster angle to introduce a wavelength-dependent transmission in the beam path. Wavelength adjustments of 0.1 nm steps can be made through the birefringent filter. The etalon gives another wavelength-dependent transmission in the beam path and a frequency selectivity of  $\sim 100$  kHz, which allows for single longitudinal mode operation. It is additionally possible to lock the etalon to the nearest longitudinal mode so that the SolsTiS can emit light at the same longitudinal mode for several hours. As top-of-fringe locking is used in this servo, a dither is used at 18.8 kHz. If the top-of-fringe lock is engaged, a Piezo element inside the resonator is tuned, changing the resonator length and thus the resonance frequency. When

## 5. The Experimental Setup

tuning the Piezo element the etalon lock follows, which allows to tune the longitudinal mode output frequency.

Three actuators are used in the SolsTiS resonator to give feedback in the PDH lock. Two of them are Piezos in a dual-stack configuration, called the *slow* and the *fast Piezo*. The dual-stack Piezos can be found as “Piezo Actuators” in Figure 5.1. The slow Piezo was already introduced as it is also used for changing the resonator length when the etalon lock is engaged. The third actuator, an electro-optic modulator, the *intracavity EOM*, is used for the fastest possible feedback in the laser lock. It is described as “EOM” in Figure 5.1. An EOM uses the *Pockels effect* to create a voltage-dependent refractive index inside its crystal [48]. This change in refractive index changes the optical path length in the laser resonator and thus results in a different frequency of the longitudinal mode. In Table 5.2, the input voltages, frequency ranges and frequency response ranges are given for all three actuators.

**Table 5.2.: Specifications of the actuators inside the new Ti:Sa laser’s bowtie resonator.**

The location of these three elements in the laser resonator can be seen in Figure 5.1. The frequency range denotes how much the actuator can change the laser frequency when the maximum of 10 V are applied. The frequency response range tells what frequencies in the error signal can be corrected. The data was given to our research team via a private presentation by *MSquared Lasers*.

Actuator	Input voltage range	Laser frequency range	Frequency response range
Slow Piezo	$\pm 10$ V	$\pm 15$ GHz	0 Hz - 50 Hz
Fast Piezo	$\pm 10$ V	$\pm 40$ MHz	0 Hz - 100 kHz
EOM	$\pm 10$ V	$\pm 350$ kHz	0 Hz - 3 MHz

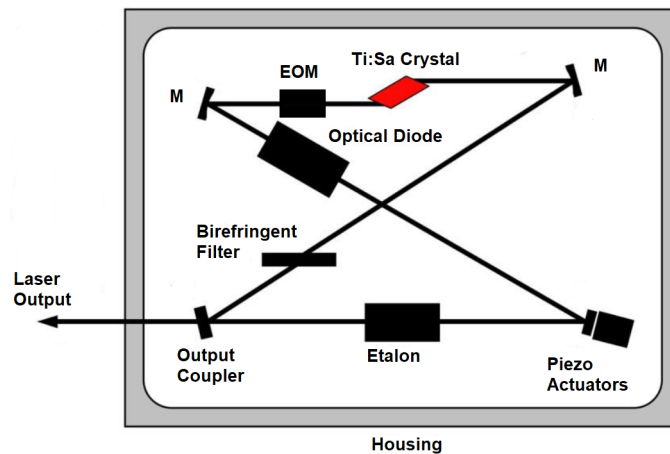


**Figure 5.1.: Elements inside the new Ti:Sa laser’s bowtie resonator.**

The geometry has its name from the apparent bowtie path followed by the laser beam. The bowtie geometry is used in combination with the optical diode to remove spectral hole burning. The Ti:Sa crystal is the gain medium and it is of the same material as the crystal shown in Figure 3.3a. The birefringent filter and the etalon are used to achieve single longitudinal mode lasing. The Piezo actuators and the EOM are the actuators in the PDH lock, their properties are listed in Table 5.2. M: mirror, EOM: electro-optic modulator.

## 5.2. Reference Cavity Characteristics

The reference cavity was set up and characterized by Helene Hainzer in 2017 [52]. Here the key results from that characterization are summarized. The reference cavity is made out of Ultra Low Expansion (ULE) glass and was delivered in parts by the company *Stable Laser Systems (SLS)*. Around the cavity is a sealed metal cylinder that is evacuated by an ion pump. The ion pump is controlled by a *Gamma Vacuum Digital SPC*. A photograph of the cavity inside the metal cylinder can be seen in [52]. The type of cavity is sometimes referred to as a *half-symmetric cavity* because it includes one planar/planar and one concave/planar mirror. The concave/planar mirror has a radius of curvature of  $R_1 = 0.5$  m. The mirror spacing is 0.1 m, so by Eq. (4.13), the free spectral range is  $\Delta\nu_{\text{FSR}} = 1.5$  GHz. The spacing between two TEM modes can be calculated to be  $\Delta\nu_{qmn} = 221$  MHz by using Eq. (4.21). SLS measured the mirror transmissions to be  $T = 8$  ppm at a wavelength of 728.9 nm, and Helene Hainzer measured a cavity Finesse of  $F = 1.61(2) \cdot 10^5$  at a wavelength of 728.9 nm. By using Eq. (4.22), the FWHM of the reference cavity linewidth can be calculated to be  $\delta\nu_c = 9.3(1)$  kHz. Further, the combined mirror losses can be calculated to be  $L_1 + L_2 \sim 25$  ppm via Eq. (4.23). In Table 5.3, the cavity parameters for 728.9 nm are listed. SLS measured the zero-crossing temperature, the temperature at which the length of the ULE cavity is minimally affected by temperature fluctuations, to be at  $32.7(1)$  °C. At the zero-crossing temperature, Helene Hainzer measured the cavity drift rate to be  $D = 202(1)$  mHz s<sup>-1</sup> using a frequency comb as a reference. The temperature stabilization is achieved via a *Wavelength Electronics LFI-3751* PID controller that manipulates heaters inside the vacuum chamber. The cavity rests inside its vacuum chamber on four black balls on top of a Zerodur block. This assembly is used to reduce vibrations and thermal heat conduction.

Two other lasers were stabilized to the reference cavity, at 786 nm and 806 nm respectively, as described in [52]. The 786 nm laser is called the Raman laser as it drives a Raman transition in the  $^{40}\text{Ca}^+$  ion. Raman transitions were briefly introduced in Subsection 2.2.2 in the context of describing the different transitions in trapped  $^{40}\text{Ca}^+$  relevant for our research team. A more detailed description of the process and applications can be read, amongst others, in [52]. The 806 nm laser is called the cavity laser as it is used in a *transfer lock*. A transfer lock is implemented when a cavity is stabilized via a laser to a reference cavity. Details about the transfer lock in our laboratory can be found in [52] and [75]. Together, these two lasers are used to stabilize the process through which single photons are generated from a  $^{40}\text{Ca}^+$  ion into an optical cavity. At the wavelengths of 786 nm and 806 nm, the reference cavity linewidths are about an order of magnitude larger than at 729 nm. The 729 laser needs to be able to be frequency-stabilized to the reference cavity at the same time as the 786 nm Raman and the 806 nm cavity lasers.

**Table 5.3.: Cavity characteristics at 728.9 nm.** Taken from [52].

Wavelength $\lambda$	728.9 nm
Transmission $T$	8 ppm
Mirror losses $L_1 + L_2$	$\sim 25$ ppm
Finesse $F$	$1.61(2) \cdot 10^5$
Cavity linewidth $\delta\nu_c$	9.3(1) kHz

### 5.3. The Experimental Setup at UIBK

In this section the final form of the experimental setup at UIBK is presented. All optical elements for frequency-stabilization of the new Ti:Sa laser are placed on two different optical breadboards: a *Thorlabs MB4590/M*, the so-called laser breadboard, and a *Thorlabs MB6090/M*, the cavity breadboard. As the names suggest, the new Ti:Sa laser is placed on the former, while the reference cavity is placed on the latter. An optical connection between the two breadboards is realized by one optical fiber of 5 m length. The contents of the rest of this section are now described. In Subsection 5.3.1, the laser stabilization setup that is distributed across these two breadboards is described. Subsections 5.3.2 and 5.3.3 go into more detail about the two additional feedback loops: the intensity stabilization of the 729 nm light arriving at the cavity breadboard and the fiber noise cancellation for the laser light that passes the 5 m long optical fiber. Afterwards, in Subsection 5.3.4, the design of the wooden shielding box is given. Finally, in Subsections 5.3.5 and 5.3.6 the beat measurement setups are explained. In Subsection 5.3.7, the distribution breadboard and connections from there to different setups are described.

#### 5.3.1. Overview of the experimental setup at UIBK

Figure 5.2 presents the experimental setup at UIBK including all elements used in the PDH lock for the new Ti:Sa laser (the figure can be found at the end of Chapter 5). The experimental setup includes the realized version of the minimal PDH lock setup that is depicted in Figure 4.4. Figure 5.2 also includes the parts of the setup that are used for intensity stabilization, fiber noise cancellation, monitoring of the laser light and a beat measurement. The optical and electronic elements and their functionalities, starting from the new Ti:Sa laser's output in Figure 5.2, are discussed in the following paragraphs.

#### Optical elements

On the laser breadboard, immediately in front of the new Ti:Sa laser head, a convex lens with a focal length of  $f = 250$  mm is installed to collimate the laser beam. The laser's full output power of 2.1(1) W (as measured in December of 2021, after the repaired SolsTiS and Equinox returned to UIBK) is not needed, so more than three quarters of laser power are first dumped. Removing this light is realized by a combination of a  $\lambda/2$ -plate and a polarizing beam splitter (PBS). The power is sent into a beam block. Next, another combination of a  $\lambda/2$ -plate and a PBS is used to split the remaining laser beam into two parts: one part is eventually sent to the distribution breadboard (Subsection 5.3.7). The second part is used for laser locking and monitoring. Following the beam path towards the reference cavity, still on the laser breadboard, a 10:90 splitter branches off light that is coupled into a single mode fiber and sent to a wavemeter, a *High Finesse WS-U*. With the help of this wavemeter, the laser frequency can be measured up to a precision of  $\pm 1$  MHz. Another 10% of the remaining laser power goes to a beat measurement setup, which will be further explained in Subsection 5.3.5. The laser light continuing towards the cavity passes two AOM setups in series: AOM1 and AOM2. First, the light passes AOM1, a *Brimrose TEF-270-100* that is operated in -1st order in a double-pass configuration with a single-pass frequency shift of 296 MHz. AOM2 is a *Gooch & Housego 3800-125* and has a multi-purpose use: First, as it is also used in -1st order, it downshifts the laser frequency by another 80 MHz. Additionally, AOM2 acts as the

## 5. The Experimental Setup

actuator in the intensity stabilization feedback loop and the fiber noise cancellation feedback loop. After AOM1 and AOM2, the laser light is coupled into a polarization-maintaining, 5 m long *Thorlabs P5-630PM-FC-5* single mode optical fiber and is sent inside the wooden shielding box containing the cavity breadboard.

The layout of the optical elements on the cavity breadboard is shown in Figure 5.2 inside the grey shaded area. The optical path of the 729 nm light on the cavity breadboard is now described. The new Ti:Sa laser light is first coupled from the fiber into freespace. Next, an optical isolator minimizes back reflections in the setup. Afterwards, a combination of a  $\lambda/2$ -plate and a Glan-Thompson polarizer only allows light of a specifically chosen polarization to be transmitted further. Next, sidebands at 11.0 MHz are modulated onto the light by an EOM (model *Qioptic PM-C-BB*). Before and after being reflected at the cavity, the light passes a  $\lambda/4$ -plate, so that the backreflected light can be reflected by a PBS onto the reflection photodiode (*Thorlabs PDA10A2*, “R-PD 729” in Figure 5.2). This photodiode is a crucial element in the PDH lock because it records the signal used to stabilize the laser frequency to the cavity. In transmission of the cavity, a dichroic filter and a 50:50 splitter put the transmitted light onto the transmission photodiode (*Thorlabs PDA36A2*, “T-PD 729” in Figure 5.2) at 40 dB gain and a *Caddx Turbo EOS2* CCD camera. Both are used for monitoring the locked 729 nm laser. The transmission signal recorded by the CCD is displayed on a screen outside of the wooden shielding box.

### Electronic elements

The electronic elements used in the experimental setup at UIBK are depicted in Figure 5.2. The electronic signal that is generated by the reflection photodiode is sent through a *Minicircuits ZFL1000+* amplifier and a *Minicircuits BBP-10.7+* bandpass filter. This amplified and filtered signal is then sent, together with the reference signal from the function generator (*Tektronix AFG 1062*), to the mixer (*Minicircuits ZAD-1-1+*). The function generator produces a modulation frequency of 11.0 MHz at a voltage of 0.7 V<sub>pp</sub>. It sends this signal to the mixer and to the EOM amplifier, a *Qioptic SIN-Amplifier*. The mixed down error signal is sent to two controllers, both model *Toptica FALC 110*. FALC1 is responsible for controlling the dual-stack Piezo actuators and FALC2 for controlling the intracavity EOM actuator. All three actuators are inside the bowtie cavity of the new Ti:Sa laser (Figure 5.1). The correction signals are sent from the FALCs back to the new Ti:Sa laser. Specifically, the signals for the dual-stacked Piezos are sent into the SolsTiS *IceBLOC*, while the signal for the intracavity EOM is given directly into the SolsTiS laser head. At this point, the feedback loop for laser stabilization is closed. In the next paragraph, the FALC in general and its use in the laser stabilization setup will be described in more detail. An oscilloscope, a *Keysight DSOX 1204 G*, was used to monitor relevant signals in the setup.

## 5. The Experimental Setup

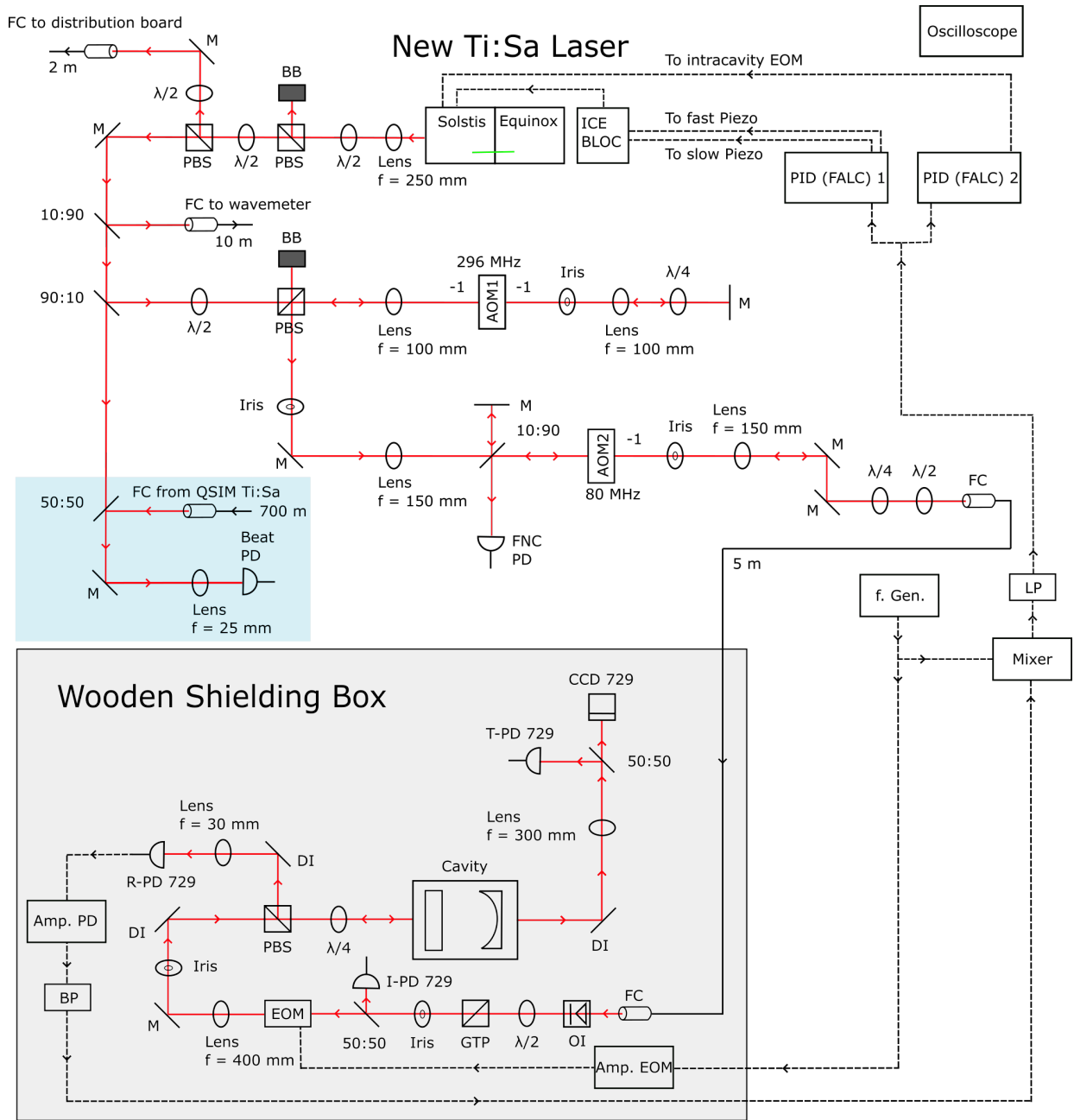


**Figure 5.2.: Sketch of the experimental setup at UIBK, Viktor-Franz-Hess building, first floor.** The main task is frequency stabilization of the new Ti:Sa laser via a PDH lock. The experimental setup also allows for: Intensity stabilization (Subsection 5.3.2), fiber noise cancellation (Subsection 5.3.3), a beat measurement with the QSIM Ti:Sa laser (Subsection 5.3.5), monitoring of the laser frequency via a connection to the wavemeter and sending light to the distribution board (Subsection 5.3.7). All optics on white background are on the laser breadboard, all optics on gray background are on the cavity breadboard, which is inside the wooden shielding box (Subsection 5.3.4). The setup for a beat with the QSIM Ti:Sa laser is on light blue background. Red lines indicate 729 nm laser light, black lines optical fibers, dashed black lines electrical connections. Arrows indicate the direction of light resp. electrical signal propagation.  $\lambda/2$  resp.  $\lambda/4$ : half-wave resp. quarter-wave plate, PBS: polarizing beam splitter, BB: beam block, M: mirror, FC: fiber coupler, AOM: acousto-optic modulator, EOM: electro-optic modulator, OI: optical isolator, GTP: Glan-Thompson polarizer, DI: dichroic mirror, CCD: charged coupled device, PD: photodiode, R-PD: reflection photodiode, T-PD: transmission photodiode, I-PD: intensity stabilization photodiode, Amp. PD: amplifier for the photodiode signal, Amp. EOM: EOM amplifier, BP: bandpass filter, LP: lowpass filter f. Gen: frequency generator.  $f$  beneath lens means the focal length, and a division of two numbers next to a splitter means reflection:transmission ratio for the incident laser light.

### The Fast Analog Linewidth Controller (FALC)

The model name *FALC* is an acronym for “*Fast Analog Linewidth Controller*” [76]. As the name suggests, the FALC is specifically designed to allow for feedback in laser stabilization applications. The device has two possible inputs for the error signal in the form of BNC connectors, the non-inverting and the inverting input. Whether the non-inverting or the inverting input has to be used is given by the polarity of the error signal, which is determined by the relative phase  $\phi$  in Eq. (4.28). Internally, after the input offset and gain can be adjusted, the signal is split into two circuit branches, the so-called *fast circuit branch* and the *slow circuit branch*. The fast circuit branch includes four different feedback elements in series, the extra slow limited integrator (XSLI), the slow limited integrator (SLI), the fast limited integrator (FLI) and the fast limited differentiator (FLD). For each element, capacitors can be chosen via dual in-line package (DIP) switch banks that allow for different amplifications at different feedback frequencies. After the four feedback elements in series, a knob allows to adjust the output main gain. The correction signal created by the fast circuit branch leaves the FALC through the main output BNC connector, while the monitor output allows for an observation of the correction signal when it is connected to e.g., an oscilloscope. Both the main and monitor output have an output voltage range of  $\pm 2$  V at  $50 \Omega$  load. The slow circuit branch includes adjustments for the unlimited integrator (ULI) that mainly corrects for frequency drifts in the time span of seconds to hours. The ULI speed selector includes a DIP switch bank where the user can vary between different resistors and capacitors. In this circuit branch, the output voltage range and the output polarity can also be adjusted. The FALC also includes a switch to manually disengage the ULI. The correction signal created by the slow circuit branch leaves the FALC through the unlimited integrator output BNC connector. The unlimited integrator output BNC connector has a maximum voltage output range of  $\pm 5$  V at a load of  $> 1 \text{ k}\Omega$ , however this output voltage range is reduced for a load of  $50 \Omega$ .

To stabilize the new Ti:Sa laser, the fast circuit branches of two different FALCs are used to give feedback to the fast Piezo (FALC1) and the intracavity EOM (FALC2), respectively. Additionally, FALC1 is used to give feedback to the slow Piezo via the slow circuit branch. The specific settings used for the new Ti:Sa frequency stabilization will be shown in the corresponding sections where the locking performance is discussed. The general idea behind the new Ti:Sa laser lock is as follows: The ULI gives feedback to the slow Piezo and corrects for frequency changes between 0 Hz and 50 Hz. The fast circuit branch for the fast Piezo corrects for frequency changes between 50 Hz and 100 kHz, the fast circuit branch for the EOM between 100 kHz and 3 MHz. However, these frequency limits are not rigid and there are transition zones at 50 Hz and 100 kHz where two different branches correct the error signal. Further, the Fast-Fourier transformation (FFT) of the error signal is viewed on an oscilloscope and the parameters at the FALCs are chosen so that the power spectral density becomes as low as possible. In Appendix Chapter B, the FFT of the error signal in our laboratory is presented. In Chapter C of the Appendix, a proposal is given for an approach to calculate optimal FALC parameters in the PDH lock.

#### 5.3.2. Intensity stabilization

Fluctuations in laser intensity change the reference cavity length through fluctuations in light pressure and temperature on the mirrors, as was briefly discussed in Subsection 4.3.2. Using the schematic of a feedback loop from Figure 4.1, the elements needed in a laser intensity stabilization circuit can be identified. In this subsection, a general instruction on how to

build an intensity stabilization setup will be described first. Then, the intensity stabilization setup as we assembled it for the master project will be described.

The goal of laser intensity stabilization is to remove deviations in laser power from a constant power value, so a constant voltage is chosen as the reference. The laser power is measured by the sensor, a photodiode, and compared to the constant reference signal. A PID controller is then used to create the correction signal from the difference of the photodiode signal and the constant reference. An AOM is chosen as the actuator as it allows to modify the power of the process, the laser light, by altering its diffraction efficiency.

In order to stabilize the intensity of the new Ti:Sa laser, AOM2 on the laser breadboard (Figure 5.2) was used as the actuator. The sensor to monitor the intensity is a *Thorlabs PDA36A2* photodiode at 40 dB gain, marked as “I-PD 729” in Figure 5.2 and is positioned to detect part of the laser light before the reference cavity. A university-built intensity stabilization module was used in the feedback loop that included a PID controller and an internal DC reference voltage. The chosen parameters for the controller were: P-part:  $R = 1 \text{ k}\Omega$ ; I-Part:  $R = 100 \text{ }\Omega$ ,  $C = 100 \text{ nF}$ ; no D-part. The optical and electrical elements and connections used for intensity stabilization can be seen in Figure 5.3. In the experimental setup, intensity stabilization and fiber noise cancellation are done on the same AOM2 as an actuator, so the elements of both feedback loops are inherently connected.

### 5.3.3. Fiber noise cancellation

In analogy to the previous subsection about intensity stabilization, the elements used in fiber noise cancellation can be identified by using Figure 4.1 as a reference. The reasons for fiber noise and the necessity of fiber noise cancellation (FNC) for a narrow linewidth was discussed in Subsection 3.1.3. In this subsection, a general instruction on how to build an FNC setup will be described first. Then, the FNC setup as we assembled it for the master project will be described.

In general, for fiber noise cancellation the laser light is sent through an AOM into the fiber, back reflected at the end of the fiber, sent back and again through the AOM. For an AOM with a modulation frequency  $\Omega$  the laser light and the back reflected laser light are creating a beat signal at  $2\Omega$  when being overlapped, the FNC beat, with phase noise  $2\phi_f$  modulated onto the light by fiber noise [57]. This beat is measured by the photodiode as the sensor and sent to the fiber noise module. The module receives a reference signal of  $2\Omega$  and compares it with the signal that was sent by the photodiode. A Voltage Controlled Oscillator generates a correction phase  $\phi_c$  depending on the difference between the reference and the photodiode signal. The correction signal is given back to the AOM that is acting as the actuator in the loop. The AOM then modulates the laser light so that  $\phi_c$  ideally cancels  $\phi_f$ .

Fiber noise cancellation was implemented in the new Ti:Sa laser setup for the 5 m long polarization-maintaining *Thorlabs P5-630PM-FC-5* fiber that connects the laser and cavity breadboards. For fiber noise cancellation, AOM2 on the laser breadboard with 80 MHz modulation frequency was used. A *Thorlabs PDA10A2* photodiode was used as the sensor (“FNC PD” in Figure 5.2), the beat signal was created by installing a 10:90 splitter into the beam path. The Voltage Controlled Oscillator is inside a university-built fiber noise module, and the reference signal of 160 MHz is created by a university-built Direct Digital Synthesizer (DDS). The combined setup of intensity stabilization and fiber noise cancellation with all relevant optics and electronics is depicted in Figure 5.3.

## 5. The Experimental Setup

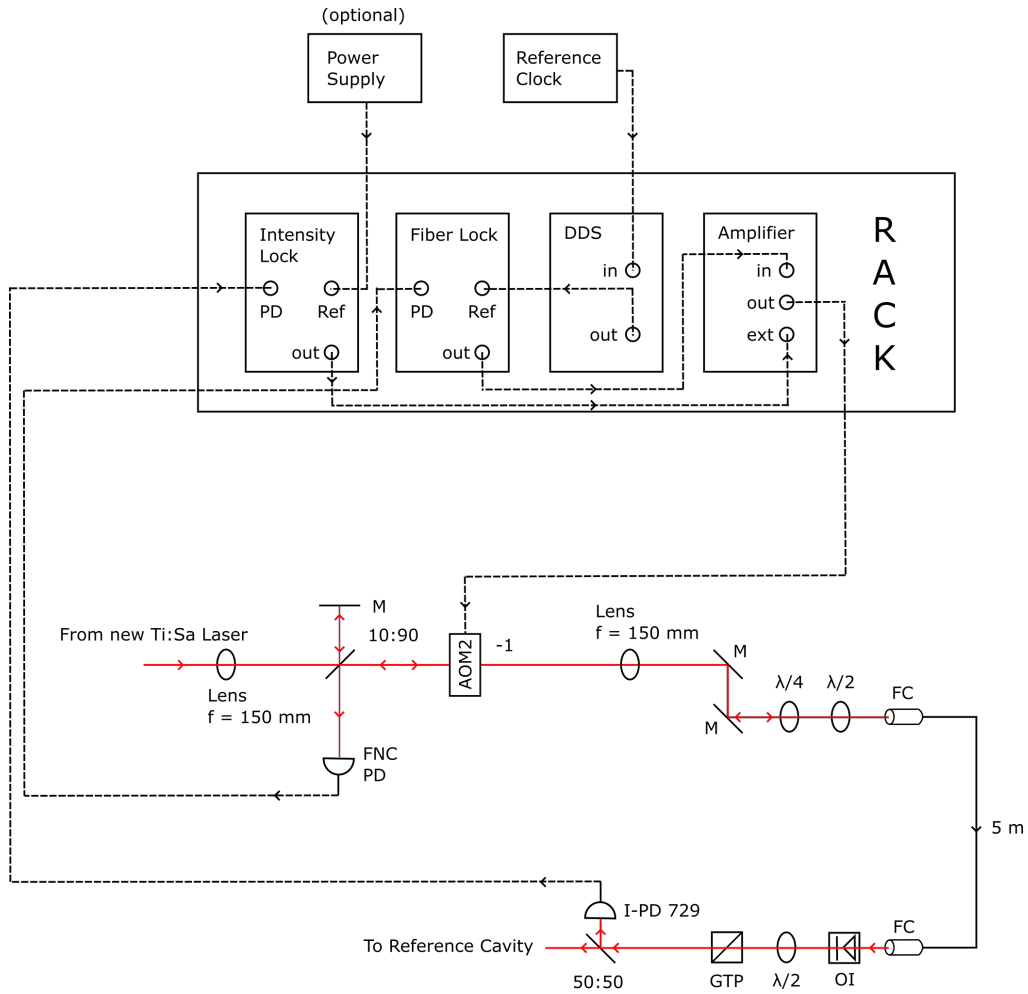


**Figure 5.3.: FNC and intensity stabilization setup for the new Ti:Sa laser with one AOM as actuator.** The intensity lock module, the fiber lock module, the DDS and the amplifier are in one rack. All the devices in the rack are university-built. Both servos can work with the same AOM (the same AOM2 as in Figure 5.2, a *Gooch & Housego 3800-125*) because the amplifier receives a corrected phase at *in* for FNC and a corrected signal that tells how much it should amplify at *ext* for intensity stabilization. A reference clock can be used to give a reference frequency to the DDS. The reference signal for the intensity lock module can be given internally, or a DC voltage can be given by a power supply externally. The FNC-PD is a *Thorlabs PDA10A2*, the I-PD 729 is a *Thorlabs PDA36A2*. Red lines indicate 729 nm laser light, black lines optical fibers, dashed black lines electrical connections. Arrows indicate the direction of light resp. electrical signal propagation.  $\lambda/2$  resp.  $\lambda/4$ : half-wave resp. quarter-wave plate, M: mirror, FC: fiber coupler, AOM: acousto-optic modulator, OI: optical isolator, GTP: Glan-Thompson polarizer, PD: photodiode, FNC PD: photodiode for fiber noise cancellation, I-PD: intensity stabilization photodiode.  $f$  beneath lens means the focal length, and a division of two numbers next to a splitter means reflection:transmission ratio for the incident laser light.

### 5.3.4. Wooden shielding box

A wooden shielding box was constructed with the intention of reducing acoustic noise affecting the reference cavity. Specifically, spruce wood of 27 mm thickness was used to build a box with a length of 145 cm, a width of 95 cm and a height of 65 cm. The box was filled 10 cm deep with sand and the walls were coated in 10 cm thick pyramid foam. The idea behind the sand is to damp mechanical vibrations, the idea behind the pyramid foam is to damp acoustic noise in the box. Three holes were cut into the box to allow for cables to pass through, one hole with a diameter of 10 cm on the top and two smaller holes on the side with a diameter of 3 cm each. The front side of the box consists of a lid that can be removed by opening four toggle latches and lifting it with two handles. The cavity breadboard was placed inside the box on the sand and cables and fibers were put through the holes in the walls and on the ceiling.

The wooden box was constructed in the IQOQI workshop and installed after the move to UIBK. A few months after the move, the sand was removed as its presence was not found to affect the achieved laser linewidth. An *Accurion Halcyonics\_Variobasic* vibration isolation board was then bought that was placed inside the wooden shielding box underneath a *Honeycomb SG breadboard* and the cavity breadboard. This was done in a new attempt to reduce mechanical vibrations affecting the reference cavity.

There were three things that hindered a quick construction of the box. First, the box was calculated to be built with a wood thickness of 30 mm, however the hardware store did not have this specific size. As a consequence, the entire box design had to be recalculated for 27 mm. Next, sticking pyramid foam onto spruce wood is not possible with average household glue. The glue that was used in the end is called *Pattex Kraftkleber Transparent*. Finally, the amount of screws actually needed and the amount of screws calculated beforehand differed greatly. It is recommended to buy more screws than initially thought.

### 5.3.5. Setup for an optical beat with the QSIM Ti:Sa laser at UIBK

For a beat measurement with the new Ti:Sa laser the choice fell on the Ti:Sa laser from the Quantum Simulation team (QSIM) at the IQOQI in Innsbruck. In this research team, Gerhard Kirchmair had set up a stabilized Ti:Sa laser system at 729 nm (henceforth named the “QSIM Ti:Sa laser”) in 2006 [74] with a laser linewidth of 1.7(1) Hz, as measured by a beat measurement with another frequency-stabilized Ti:Sa laser at UIBK over a measurement time of 2 s.

A beat setup requires a beamsplitter to overlap both laser beams and a photodiode, ideally with a convex lens in front for focusing purposes. The setup that was used to measure the beat between the new Ti:Sa laser and the QSIM Ti:Sa laser while at UIBK is depicted in Figure 5.2 inside the light blue zone. The photodiode, titled “Beat PD” in the figure, is a university-built photodiode with a bandwidth of 1 GHz. An *R&S FSV 3004* spectrum analyzer was used to process the photodiode signal. The QSIM laser system is located at IQOQI, which is situated in another building around 300 m beeline from the beat setup. The QSIM laser light is sent through approximately 510 m of a polarization-maintaining single-mode fiber to the ground floor of UIBK and then through approximately 140 m of a non-polarization-maintaining single-mode fiber to the UIBK first floor, where the new Ti:Sa laser is located. To overcome fiber noise that is collected through approximately 650 m of optical fiber, FNC is present on the QSIM site. As measured and presented by Roman Stricker in [59], fiber noise does not have a contribution to the laser linewidth above 31.2(15) mHz in the QSIM light that is sent from IQOQI to the ground floor of UIBK.

### 5.3.6. The three-cornered hat measurement setup at UIBK

Even though the QSIM Ti:Sa laser is expected to have a linewidth in the Hz regime, there is no way to distinguish between a broadening of the beat spectrum due to imperfections in the QSIM laser light arriving at the beat setup in our laboratory at UIBK first floor or due to imperfections in the new Ti:Sa laser. It is only possible to get an upper limit estimation for the laser linewidth of any one laser from a single beat measurement. In order to obtain a direct value for the new Ti:Sa laser linewidth, a three-cornered hat measurement was conducted. The idea and theory behind said measurement technique can be found in Subsection 3.2.

To realize the three-cornered hat measurement, a third frequency-stabilized laser has to be included. The decision fell on the Ti:Sa laser used in the Linear team at UIBK, a laser system that was stabilized by Roman Stricker in 2017 to a linewidth of 3.6(4) Hz over a measurement time of 4 s, as measured by a three-cornered hat measurement with the QSIM Ti:Sa laser and a diode laser at 729 nm [59]. The stabilized laser in question will from now on be called the “Linear Ti:Sa laser”. The Linear Ti:Sa laser is located at the UIBK ground floor and is separated from the new Ti:Sa laser at UIBK by approximately 140 m of a polarization-maintaining single-mode optical fiber, so FNC is mandatory for a beat measurement. In Figure 5.4, a sketch of the three-cornered hat setup is shown. Our research team is named “Quantum Frequency Conversion” (QFC). In analogy to QSIM and Linear this name shall be used in the future when denoting beat measurements between laser pairs. Light from the new Ti:Sa (QFC) laser is taken at the distribution board, sent through an FNC setup and then through approximately 140 m of a polarization-maintaining single-mode optical fiber to the UIBK ground floor where there is a second beat setup that is largely identical to the one in our laboratory on UIBK first floor (blue shaded area in Figure 5.2). The QSIM light is first sent to the Linear laboratory at UIBK ground floor before it arrives at our laboratory on UIBK first floor, so it is possible to branch off QSIM light there for a beat measurement with the Linear Ti:Sa laser. In comparison to Roman Stricker’s setup in [59], the setup in Figure 5.4 allows only to do one beat at a time and not all three of them simultaneously.

### 5.3.7. Connections to other setups at UIBK

Next to the new Ti:Sa laser at 729 nm, the Raman laser at 786 nm and the cavity laser at 806 nm are using the reference cavity inside the wooden box for stabilization purposes. A description of both lasers and their purposes can be found in Section 5.2 and references therein. In Figure 5.5, the optical setup inside the wooden shielding box is depicted. Blue lines for the 786 nm laser and green lines for the 806 nm laser are used in the drawing. The Raman and cavity lasers’ corresponding laser breadboards are shown in Figure 5.6. As part of this master project, I added intensity stabilization to these laser systems based on the schematic that is presented in Subsection 5.3.2. The AOMs in double-pass configuration in Figure 5.6 play the role as the actuators in the 786 nm and 806 nm intensity stabilization feedback loops. The sensors are the photodiodes “I-PD 786” and “I-PD 806” in Figure 5.5, *Thorlabs PDA36A2* photodiodes at 40 dB gain each.

In the top left corner in Figure 5.2, a fiber coupler is installed to steer light towards a distribution breadboard. From there, 729 nm laser light is sent to the ion trap that stands on the same optical table (a description of the ion trap can be found in [75]) and downstairs to a part of the three-cornered hat measurement setup (Subsection 5.3.6). Further, laser light is sent to the 2D Crystals team and will in the future be sent to the quantum molecules team. Both research teams are mentioned and referenced in the Introduction Chapter 1.

## 5. The Experimental Setup

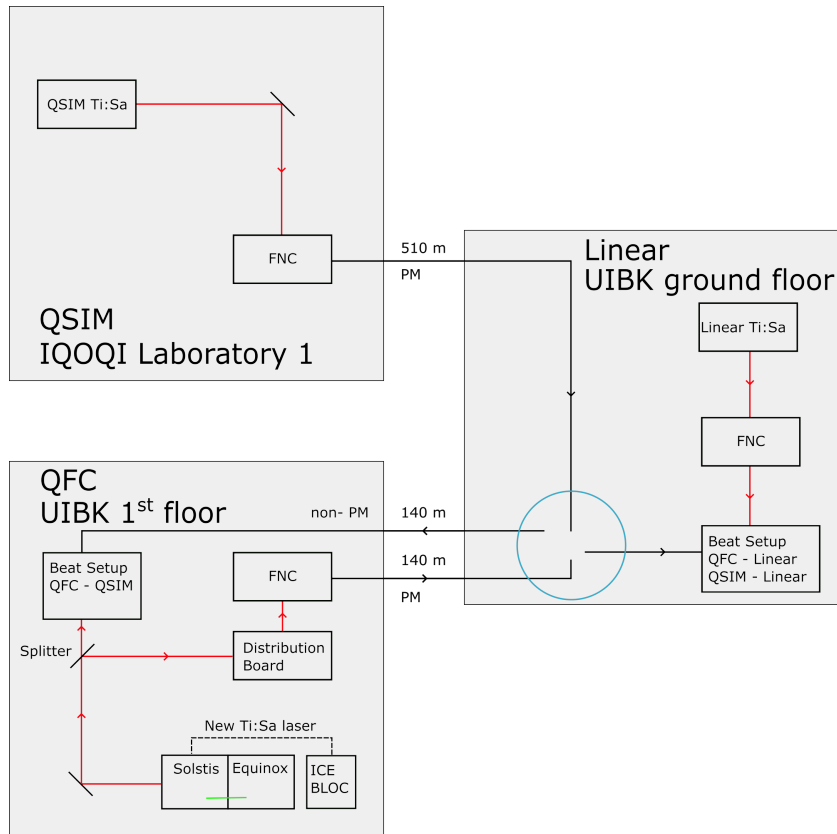


**Figure 5.4.: Sketch of the three-cornered hat measurement setup.** For the three-cornered hat measurement, beat measurements between three laser pairs are made. The involved lasers are the QSIM Ti:Sa laser [74], the Linear Ti:Sa laser [59] and the new Ti:Sa laser from our QFC team. The beat setup for the QFC-QSIM beat was performed at UIBK first floor, the QFC-Linear and QSIM-Linear beats at UIBK ground floor. Red lines indicate 729 nm laser light in free space, black lines indicate single mode optical fibers. The acronym PM next to the fibers means polarization-maintained, non-PM means non-polarization-maintained. Arrows indicate the direction of light propagation. The blue encircled area indicates where fibers can be joined so that all combinations of beat measurements can be performed. The grey zones indicate three different locations that are separated by several 100 m of optical fiber, so FNC is mandatory. A general description of an FNC setup is given in Subsection 5.3.3. The experimental setup at “QFC UIBK 1<sup>st</sup> floor” is described in detail in Subsection 5.3.1.

## 5. The Experimental Setup

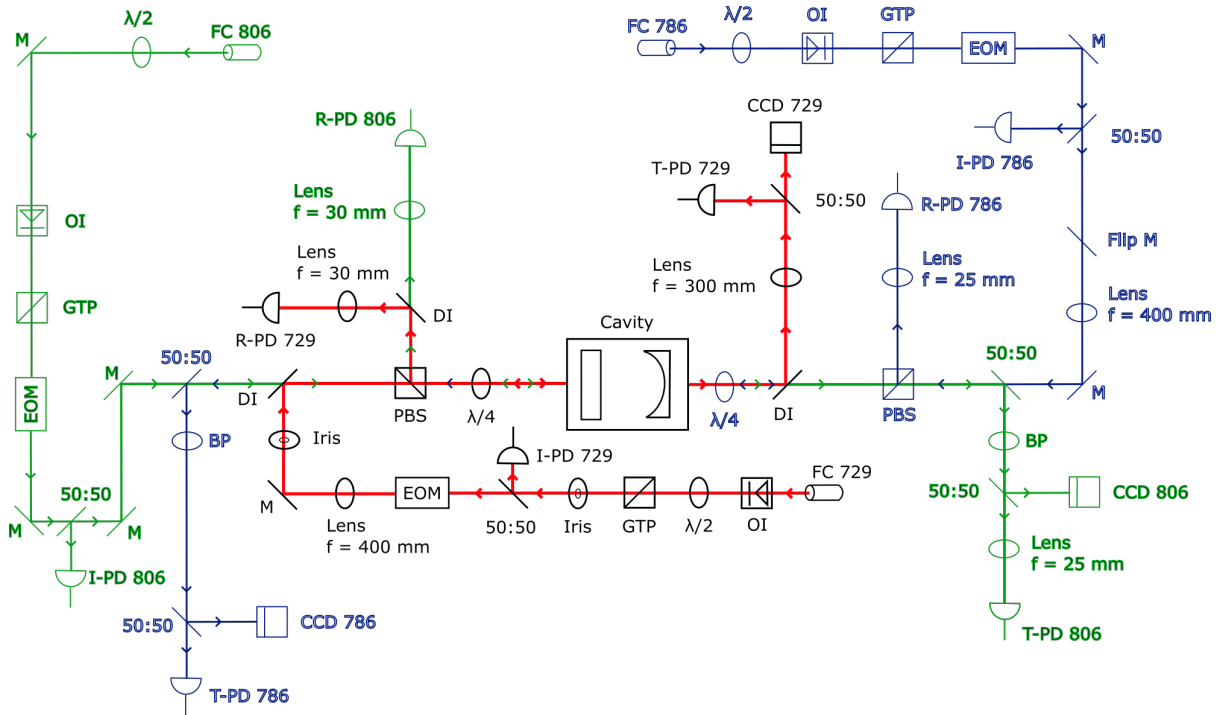


**Figure 5.5.: Optical elements on the cavity breadboard.**

Red lines indicate 729 nm laser light, blue lines indicate 786 nm light and green lines indicate 806 nm light. The optical elements that belong to the Raman laser PDH lock at 786 nm (blue) and cavity laser PDH lock at 806 nm (green) were assembled by Helene Hainzer in 2017 [52]. During this master project the optical elements for the new Ti:Sa laser PDH lock at 729 nm (black) were added. Arrows indicate the direction of light propagation.  $\lambda/2$  resp.  $\lambda/4$ : half-wave resp. quarter-wave plate, PBS: polarizing beam splitter, BP: bandpass filter, M: mirror, FC: fiber coupler, EOM: electro-optic modulator, OI: optical isolator, GTP: Glan-Thompson polarizer, DI: dichroic mirror, CCD: charged coupled device, PD: photodiode, R-PD: reflection photodiode, T-PD: transmission photodiode, I-PD: intensity stabilization photodiode.  $f$  beneath lens means the focal length, and a division of two numbers next to a splitter means reflection:transmission ratio for the incident laser light.

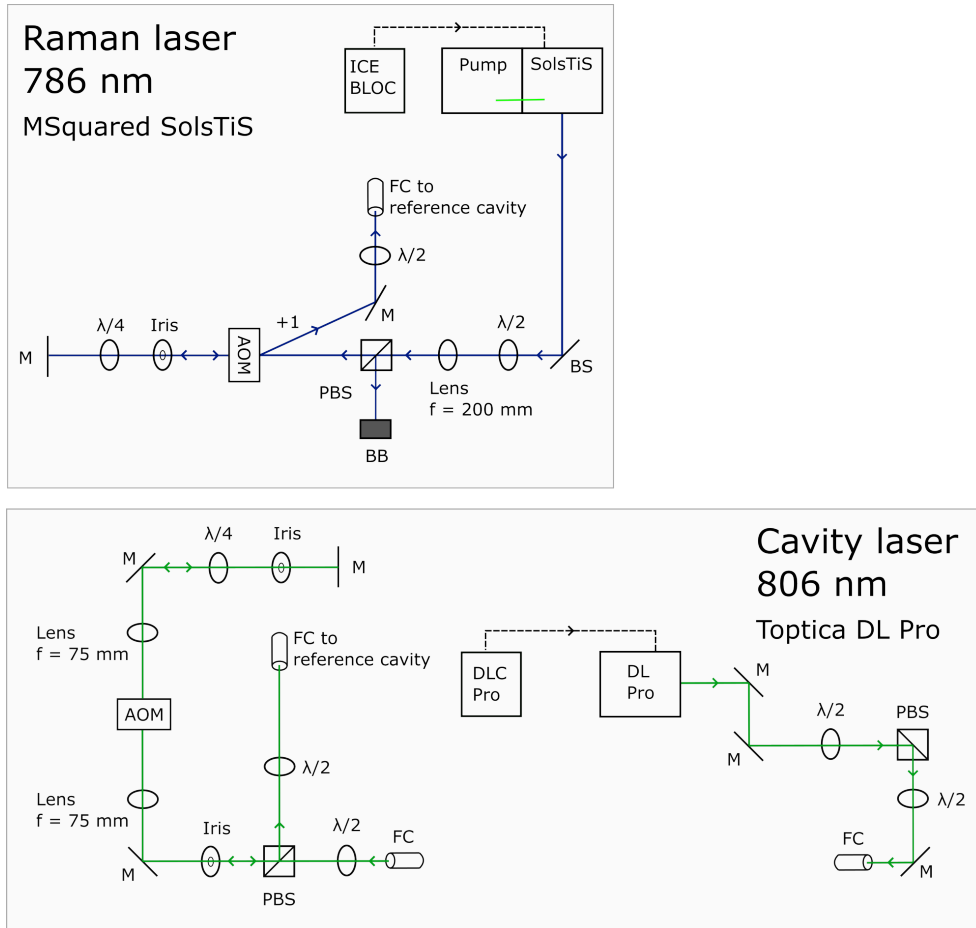


**Figure 5.6.: AOM setup of the 786 nm Raman laser and the 806 nm cavity laser.** The setup was assembled by Helene Hainzer in 2017 [52]. During this master project intensity stabilization was added to both lasers. Specifically, photodiode signals from the cavity breadboard (Figure 5.5) were stabilized by feeding back to the two double-pass AOMs that are shown in this figure. Blue lines indicate 786 nm light and green lines indicate 806 nm light. Arrows indicate the direction of light propagation.  $\lambda/2$  resp.  $\lambda/4$ : half-wave resp. quarter-wave plate, PBS: polarizing beam splitter, M: mirror, FC: fiber coupler, AOM: acousto-optic modulator, BB: beam block.  $f$  beneath lens means the focal length.

## 5.4. Historical Development of the Setup

Assembling the new Ti:Sa laser stabilization setup and taking measurements has taken place at two different locations. From March to September 2021, the new Ti:Sa laser and the PDH lock was assembled and developed at IQOQI Innsbruck, ICT building, and the first characterization and performance measurements were taken. During September and October of 2021 the entire laboratory equipment was moved to new laboratories at the University of Innsbruck (UIBK), Viktor-Franz-Hess Haus, first floor. From October 2021 to April 2022, developing the system and measuring was continued at UIBK. The experimental setup at IQOQI differs in many regards from the setup at UIBK. The final form of the new Ti:Sa frequency stabilization, achieved at UIBK in April 2022, was already presented in Section 5.3. Subsection 5.4.1 presents the differences in the setup at IQOQI. Subsection 5.4.2 describes the move from IQOQI to UIBK will be described. Moving laboratory equipment that has been established over years is a nontrivial task, so any reader that finds or will find himself in a similar situation may be interested in our approaches and tips.

### 5.4.1. Experimental setup at IQOQI Innsbruck

Both because of Covid-19 restrictions and limitations in available physical space, the laser stabilization setup at IQOQI Innsbruck was distributed across two rooms, laboratory 1 and laboratory 6. The two laboratories are connected via several 30 m long polarization-maintaining, single-mode optical fibers and electrical cables. In laboratory 1, the cavity breadboard together with the optics and electronics to lock the 786 nm Raman laser and the 806 nm cavity laser were already installed by Helene Hainzer back in 2018 [52]. Figure 5.7 presents a schematic of the experimental setup at IQOQI. If a comparison is made between the setup at IQOQI to the setup at UIBK (IQOQI: Figure 5.7 vs UIBK: Figure 5.2), a variety of differences can be seen. They are summarized in the following list.

- The wooden shielding box that is described in Subsection 5.3.4 was not installed after the move to UIBK and so the reference cavity was sitting directly on its breadboard on an optical table. Those were the conditions under which Helene Hainzer characterized the reference cavity and locked the 786 nm Raman and 806 nm cavity lasers to it, as described in [52].
- A *Minicircuits BLP-10.7* lowpass filter was used at IQOQI instead of the *Minicircuits BBP-10.7+* bandpass filter at UIBK.
- For the beat measurement with the QSIM Ti:Sa laser, about 10% of 729 nm laser power after the fiber coupler on the cavity breadboard was taken by a splitter. The QFC-QSIM beat was measured on the cavity breadboard and not on the laser breadboard as it is at UIBK.
- The part of the setup including AOM1 was not yet installed.
- The setup in laboratory 6 did include AOM2 changing the frequency by 80 MHz, but it was not used for intensity stabilization or fiber noise cancellation.
- The intracavity EOM was not yet engaged in the PDH lock, so FALC2 was not used.

The QSIM laser is located in laboratory 1 at IQOQI and the light was brought to the reference cavity table through a polarization-maintaining, single-mode 20 m long optical fiber without FNC. For the QFC-QSIM beat at IQOQI, the same university-built photodiode with a bandwidth of 1 GHz was used as it is used at UIBK. Next to the QFC-QSIM beat setup that is on red background in Figure 5.7, another measurement setup can be seen on green background. This setup works as an add-on to the beat measurement and allows us to quantify the beat center frequency drift. A function generator produces a sinusoidal signal that is similar in frequency to the beat frequency up to  $\sim$  kHz. A mixer mixes the signals down to the kHz regime and gives the output to a TTL converter. This device waits for two zero-crossings in signal voltage, indicating one period, and creates one signal pulse. The stream consisting of single pulses is sent to a *Swabian Time Tagger 20* that measures pulses per second. This way, the beat center frequency and especially its drift over time can be measured.

Laboratory 6 is separated from laboratory 1 via a hallway, and 30 m long optical fibers as well as electrical cables have to be routed from one laboratory to the other through holes in the wall and along the hallway ceiling. As mentioned in Subsection 5.3.1, the optical fiber used at UIBK is 5 m long, even though 2 m would be theoretically possible. No electrical cable at UIBK is longer than 3 m. Long distances between laser and reference cavity should be avoided in a PDH lock, firstly because the finite speed of light limits the maximum possible frequency that the controller can correct for, and secondly the longer the fiber the more fiber noise is modulated onto the laser light. To sum up the situation at IQOQI, it was possible to lock the laser and do a beat measurement. However, no FNC was installed for neither

the new Ti:Sa laser or the QSIM Ti:Sa laser that were involved in the beat measurement. Additionally, no intensity stabilization feedback loop was engaged. Nevertheless, the IQOQI setup allowed for critical measurements that will be presented in the following Chapter 6.

### 5.4.2. Moving the setup to UIBK

The distance between the old laboratories at IQOQI and the new laboratories at UIBK is about 300 m beeline, however by car the distance is about half a kilometer. The move from IQOQI to UIBK started on September 13th, 2021. The MSquared laser system started to malfunction already in August and despite some remote fixing attempts by the company it still remained in its state of sporadically switching off in September. As a consequence, by September 13th, the laser system had already been packed up one week prior and sent back to MSquared. Transporting the laser breadboard to UIBK without the laser on it was an unproblematic straightforward delivery by car. The cavity breadboard, however, had to be treated much more carefully. If the cavity experiences mechanical shocks or too strong tilting it can fall off the four black balls on which it rests inside the vacuum chamber. If this happened, it would mean that either laser light cannot be coupled into the cavity anymore or at least that the cavity would experience enhanced vibrations on the cavity mirrors through direct contact with the base beneath. To avoid this happening, measures were taken during transport. First, a level was put onto the breadboard and constantly monitored, so that the cavity was never tilted more than 2-3° while lifting. In laboratory 1, the breadboard was lifted onto a small trolley by three people and then slowly rolled to the car. Four handles, one on each side, were screwed onto the breadboard so that it could be lifted and carried. On the way to the car, small metal ramps and carpets were put on every sharp irregularity on the floor to mitigate mechanical shocks. An electric car was chosen so that no strong vibrations from the motor had to be expected. After slowly driving over to UIBK, the breadboard was put again on a trolley and escorted to the new laboratory. Here, three people lifted the breadboard inside the wooden shielding box that was already assembled, onto the sand. All optical fibers and electronic devices were reconnected, and when the SolsTiS returned from MSquared by December 20th, the laser could be relocked.

## 5. The Experimental Setup

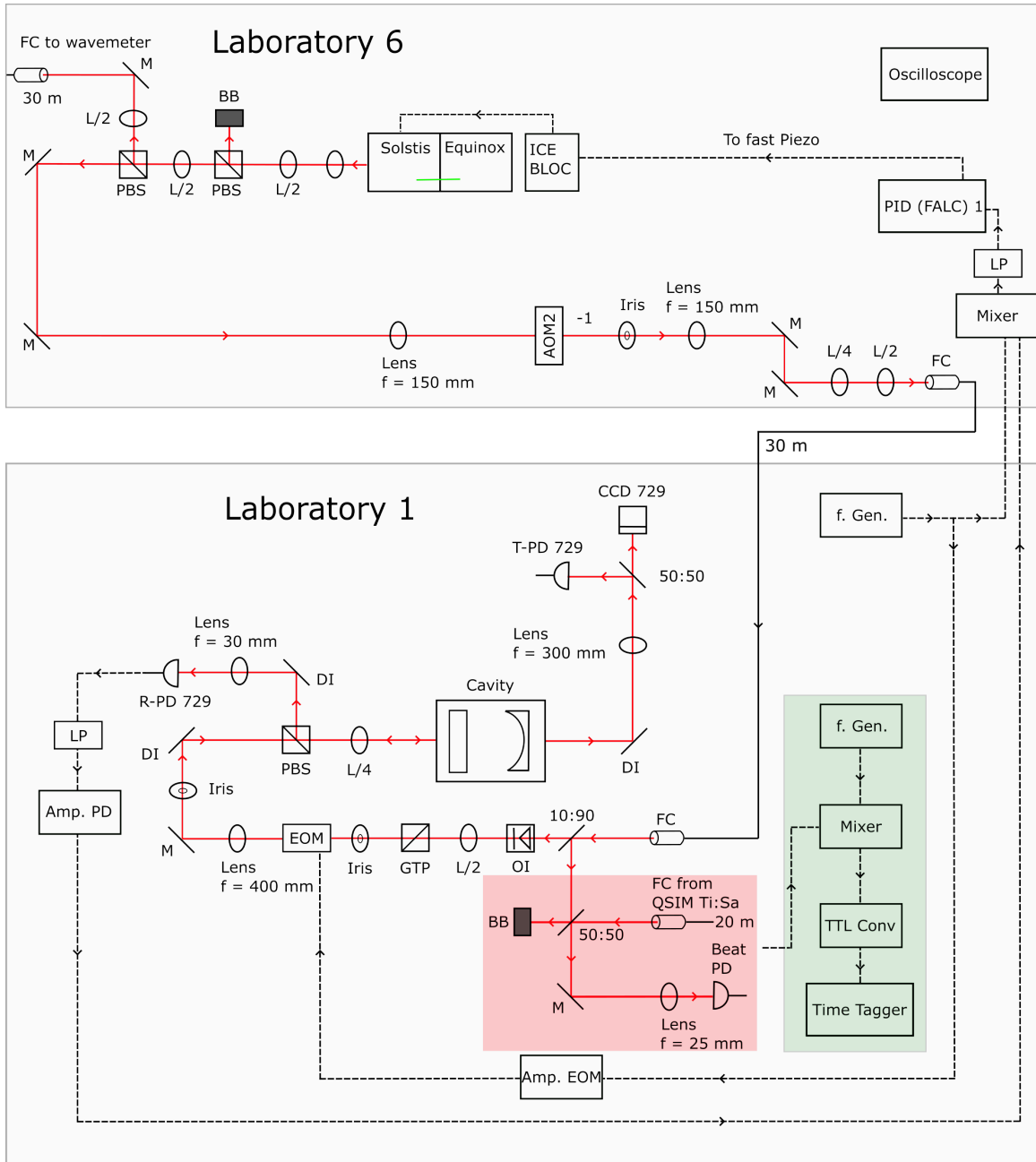


**Figure 5.7.:** Sketch of the experimental setup at IQOQI Innsbruck, laboratory 1 and laboratory 6. The main task is frequency stabilization of the new Ti:Sa laser via a PDH lock. The experimental setup also allows for: A beat measurement with the QSIM Ti:Sa laser, a measurement of the beat center frequency drift and monitoring of the laser frequency via a connection to the wavemeter. The beat setup is on red background. The setup for the beat center frequency measurement that can be added to the “Beat PD” is on green background. The “Beat PD” is the same university-built photodiode with 1 GHz bandwidth as in the beat setup at UIBK. Changes in the setup at IQOQI compared to UIBK are listed in Subsection 5.4.1. Red lines indicate 729 nm laser light, black lines optical fibers, dashed black lines electrical connections. Arrows indicate the direction of light resp. electrical signal propagation.  $\lambda/2$  resp.  $\lambda/4$ : half-wave resp. quarter-wave plate, PBS: polarizing beam splitter, BB: beam block, M: mirror, FC: fiber coupler, AOM: acousto-optic modulator, EOM: electro-optic modulator, OI: optical isolator, GTP: Glan-Thompson polarizer, DI: dichroic mirror, CCD: charged coupled device, PD: photodiode, R-PD: reflection photodiode, T-PD: transmission photodiode, I-PD: intensity stabilization photodiode, Amp. PD: amplifier for the photodiode signal, Amp. EOM: EOM amplifier, LP: lowpass filter  $f$ . Gen: frequency generator, TTL Conv: TTL converter.  $f$  beneath lens means the focal length, and a division of two numbers next to a splitter means reflection:transmission ratio for the incident laser light.

## 6. Results at IQOQI

The main task at IQOQI was to estimate the linewidth of the locked new Ti:Sa laser at a wavelength of 729 nm. For that, a beat measurement with the QSIM Ti:Sa laser was conducted. The experimental setup of the new Ti:Sa laser at IQOQI is presented in Figure 5.7 and discussed in Section 5.4.1. Section 6.1 presents the FALC settings for the new Ti:Sa laser lock, the QFC-QSIM beat measurement results and a discussion about the beat linewidth limitations. Another issue that was investigated at IQOQI were intensity fluctuations of the three lasers that can be locked to the reference cavity and introduce frequency fluctuations to the locked new Ti:Sa laser. Intensity fluctuations of laser fields inside a reference cavity can cause its resonance frequency to change. The theory behind this effect is explained in Subsection 4.3.2. In Section 6.2 of this chapter, a characterization of the intensity fluctuations of three lasers fields inside the reference cavity are presented as well as predictions of their influence on the locked new Ti:Sa laser’s linewidth.

### 6.1. Laser Linewidth Measurement at IQOQI

#### 6.1.1. Beat measurement with QSIM at IQOQI

The parameters of the two FALCs that were used for frequency-stabilization of the new Ti:Sa laser at IQOQI are shown in Table 6.1. The different constituents of a FALC are described in Subsection 5.3.1. For laser stabilization at IQOQI neither FALC2 nor the ULI of FALC1 were engaged as we did not fully understand how to include the slow Piezo and the intracavity EOM into a stable laser lock at the time. This means that only FALC1 was effectively used and only the fast Piezo element was involved as an actuator. The fast Piezo cannot correct for frequencies above 100 kHz, as Table 5.2 shows. As a consequence, the FLD did not contribute to the laser lock, and the laser was effectively stabilized by three integrators, the SLI, the FLI and the XSLI. The ineffectiveness of the FLD at these settings was only realized months later, after the move. The place of FALC1 in the experimental setup at IQOQI can be seen in Figure 5.7. One realization was that the new Ti:Sa laser can be locked over a timespan of  $\sim$  hours with only the SLI, FLI, XSLI and only the fast Piezo correcting. However, compared to after the move to UIBK, when every actuator was engaged, the laser lock was significantly more unstable at IQOQI, falling out of lock much easier and at shorter intervals.

The setup for the first QFC-QSIM beat measurement taken at IQOQI is now presented. During this measurement, only the new Ti:Sa at 729 nm was locked to the reference cavity, the 786 nm Raman laser and the 806 nm cavity laser were blocked from entering the reference cavity. The QFC-QSIM beat setup is depicted in the part of Figure 5.7 with a red background. The photodiode that was used in the beat measurement, a university-built photodiode with a bandwidth of 1 GHz, is named “Beat PD” in the figure. The photodiode signal was analyzed by a *Rohde and Schwarz FSP* spectrum analyzer. The frequency resolution of the *Rohde and Schwarz FSP* spectrum analyzer is 0.01 Hz according to the data sheet, so error bars cannot be visible along the frequency axis in the following figures. The

## 6. Results at IQOQI

maximum uncertainty of level measurement is 0.07 dB ( $1 \sigma$ ), so error bars are of the size of the data points and cannot be visible along the power spectral density axis in the following figures.

For each of a total of ten scans performed by the spectrum analyzer, the used settings were: Resolution bandwidth 100 Hz, video bandwidth 10 Hz, sweep time 4 s, frequency span 2 kHz. Figure 6.1 presents the spectrum of one of ten beat measurements taken. An  $R^2$  test yielded a coefficient of determination of 0.96 for a Gaussian fit compared to 0.95 for a Lorentzian fit, hence the Gaussian fit was chosen. The Gaussian fit for the power spectral density  $S(\nu)$  as a function of frequency was modeled after the theory curve Eq. (3.19) with an additional offset parameter  $d$ ,

$$S(\nu) = \frac{a}{c} \cdot \exp\left(\frac{(\nu - b)^2}{2 \cdot c^2}\right) + d. \quad (6.1)$$

The FWHM of the laser linewidth is connected to the fit parameter  $c$  via  $\Delta\nu = \sqrt{8 \ln(2)} \cdot c$ , as can be seen in Subsection 3.2.1. To obtain an upper limit for the new Ti:Sa's linewidth, an average of the ten consecutive beat measurements was created. Specifically, for a total of  $N = 10$  measurements the average linewidth was calculated via

$$\Delta\nu = \frac{\sum_{i=1}^N \Delta\nu_i}{N}, \quad (6.2)$$

and for the error the standard deviation was taken. The average over ten consecutive beat measurements yielded the linewidth (FWHM) of

$$\Delta\nu = 174(12) \text{ Hz}. \quad (6.3)$$

**Table 6.1.: FALC parameters of the new Ti:Sa laser used for the beat measurement with the QSIM Ti:Sa laser at IQOQI.** FALC1 drives the fast Piezo actuator and the slow Piezo actuator, FALC2 drives the intracavity EOM. The location of the three actuators inside the laser cavity are shown in Figure 5.1. The slow Piezo is only driven by the ULI. Neither the ULI of FALC1 nor FALC2 were engaged. The fast Piezo cannot correct at frequencies  $> 100$  kHz, so the laser was effectively stabilized by the three integrators SLI, FLI and XSLI. The FALC-specific acronyms are explained in Subsection 5.3.1. The place of FALC1 in the experimental setup at IQOQI can be seen in Figure 5.7.

Element	FALC1	Frequency range	FALC2	Frequency range
SLI	5	240 Hz - 14 kHz	-	-
FLI	9	3 kHz - 37 kHz	-	-
FLD	6	420 kHz - 2.3 MHz	-	-
XSLI	1	90 Hz - 2 kHz	-	-
ULI settings	-		-	
ULI range	-		-	
MG	1.5		-	

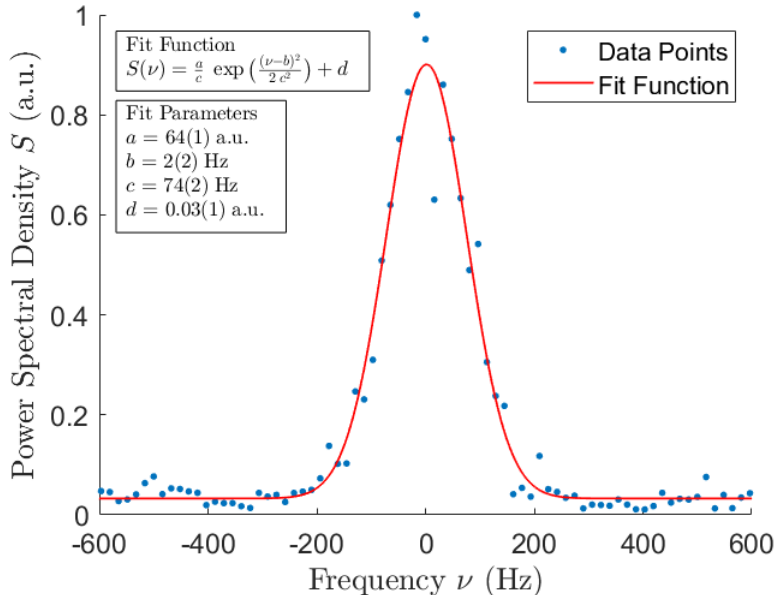


**Figure 6.1.: QFC-QSIM beat at 729 nm at IQOQI.** This is one representative of the ten beats that were used to get the value for the beat linewidth in Eq. (6.3). The data points are fitted by a Gaussian model. The beat center frequency was set to 0 and the power spectral density was normalized to 1. The data was taken by a *Rohde and Schwarz FSP* spectrum analyzer, settings: Resolution bandwidth 100 Hz, video bandwidth 10 Hz, sweep time 4 s, frequency span 2 kHz. The linewidth (FWHM) of this example beat is  $\Delta\nu_{\text{ex}} = \sqrt{8 \ln(2)} \cdot c = 174(5)$  Hz. Uncertainties of the parameters are with respect to the 67% ( $\pm 1\sigma$ ) confidence level.

### 6.1.2. Discussion of the beat result at IQOQI

A first step in discussing the beat result is to compare the linewidth obtained in the previous subsection to the two fundamental limits: The Schawlow-Townes linewidth (Eq. (3.14)) that is valid for any laser system; and the shot noise limit (Eq. (4.33)) that appears as a consequence of the PDH technique.

A value for the cavity linewidth of the new Ti:Sa laser can be calculated by estimating the finesse of the laser resonator to be  $F = 100$  and the path length in the laser resonator to be  $L = 0.2$  m (assuming air,  $n \sim 1$ ), yielding a cavity linewidth of  $\delta\nu_c = 7.5$  MHz. The new Ti:Sa's output power is  $P = 2$  W (Chapter 5). For the laser emitting light at 729 nm, approximately 411 THz in frequency  $\nu$ , the Schawlow-Townes linewidth can then be calculated to be approximately

$$\Delta\nu = \frac{\pi h \nu (\delta\nu_c)^2}{P} = 25 \mu\text{Hz}. \quad (6.4)$$

Given the measured linewidth of 174(5) Hz, the Schawlow-Townes limit of the new Ti:Sa laser is clearly not relevant.

The responsivity  $R$  of the *Thorlabs PDA10A2* photodiode used in the PDH lock is given as 0.44 at 730 nm, which allows the quantum efficiency to be calculated to  $\eta = 0.47$  using Eq. (4.34). In Chapter 5, the mirror transmission of both the reference cavity's mirrors is stated to be  $T = 8$  ppm, and the reflection amplitude squared is  $r^2 = 1 - T$ . The average cavity-incident laser power used for the linewidth measurement at IQOQI was around  $P_0 = 50 \mu\text{W}$ . For a measurement time of  $\tau = 4$  s, the linewidth limitation due to shot noise is therefore

$$\delta\nu(\tau) = \delta\nu_c \sqrt{\frac{h\nu}{\tau P_0(1-r^2)\eta}} = 18 \text{ mHz}. \quad (6.5)$$

The shot noise limit is about four orders of magnitude below the measured beat linewidth. We therefore conclude that the new Ti:Sa's PDH lock performance was not fundamentally limited by shot noise. Further, the goal of a SolsTiS linewidth stabilization to 1 Hz, where the full 1 s lifetime in  $^{40}\text{Ca}^+$  can be used for quantum information science experiments, is not a fundamentally unobtainable goal with our experimental parameters.

Given the laser linewidth of the QSIM Ti:Sa laser of 1.7(1) Hz as measured in 2006 and presented in [74], we assume that the QSIM Ti:Sa laser's linewidth at its point of origin after the laser head does not have a dominant contribution to the measured linewidth. This assumption is further supported by the fact that the QSIM team performs Ramsey experiments using the QSIM Ti:Sa laser on a daily basis and would notice if the linewidth significantly broadens beyond a few Hz.

We expect that the beat linewidth of 174(12) Hz measured at IQOQI was likely fiber noise limited. The 30 m long fiber from laboratory 6 to laboratory 1 and the 20 m long fiber from the QSIM Ti:Sa laser to the beat setup were both not fiber noise canceled. As a consequence, fiber noise cancellation was installed and engaged after the move to UIBK for both the connection fiber between the laser and cavity breadboards and the fiber from the QSIM Ti:Sa laser to the beat setup at UIBK. Next to fiber noise, fluctuations of laser intensity inside the reference cavity are another possible source of linewidth broadening. The effect from intensity fluctuations on the beat linewidth was further investigated at IQOQI and the results are reported in the next section.

## 6.2. Laser Linewidth Broadening from Intensity Fluctuations

The new Ti:Sa laser at 729 nm, the Raman laser at 786 nm and the cavity laser at 806 nm can, and for our scientific applications [52, 75] should, be locked to the same reference cavity. The data in this section was taken under the conditions that all three lasers were locked to the reference cavity. The mean cavity-incident powers were approximately 40 mW for the 729 nm laser, 15 mW for the 786 nm laser and 225 nW for the 806 nm laser. All three lasers are prone to intensity fluctuations that alter the reference cavity length and thus the reference frequency, as described in Subsection 4.3.2. We wanted to learn how the intensity fluctuations of each of these locked lasers broaden the linewidth of the locked new Ti:Sa laser at 729 nm. We did this via a two-step process. First, frequency jumps in the QFC-QSIM 729 nm beat center frequency due to a controlled intensity change in one of the three reference cavity light fields at a time were measured. For the measurement of the beat center frequency, the greenish-shaded time tagger setup in Figure 5.7 was used to analyze the beat photodiode signal. As a second step, the naturally occurring intensity fluctuations in the laser beams in the input path of the cavity were measured using an optical power meter. The predicted frequency change of the locked new Ti:Sa laser due to these fluctuations was then calculated by using the frequency jumps from the previous measurements as a reference. In the following two subsections, first the controlled frequency jump measurements and then the fluctuation measurements are presented.

### 6.2.1. Controlled intensity changes in the reference cavity light field

#### Beat Frequency Shift due to controlled changes in the 786 nm and 806 nm light fields

Locking a laser to a cavity increases the light field inside the cavity. Using the Time Tagger (greenish-shaded time tagger setup in Figure 5.7), we measured the change of the 729 nm QFC-QSIM beat center frequency when locking and unlocking the 786 nm laser and the 806 nm laser to the reference cavity. Unlocking means that the relevant laser linewidth controller is switched off. The linewidth controllers for the new Ti:Sa laser at 729 nm and the 786 nm laser are FALCs, for the 806 nm laser the controller is a *Toptica DigiLock 110* [52]. Switching off these controllers means that due to natural frequency fluctuations and drifts of the free-standing laser, the frequency is not on resonance with the cavity anymore. In Figure 6.2, the observed frequency jumps of the QFC-QSIM beat center frequency can be seen.

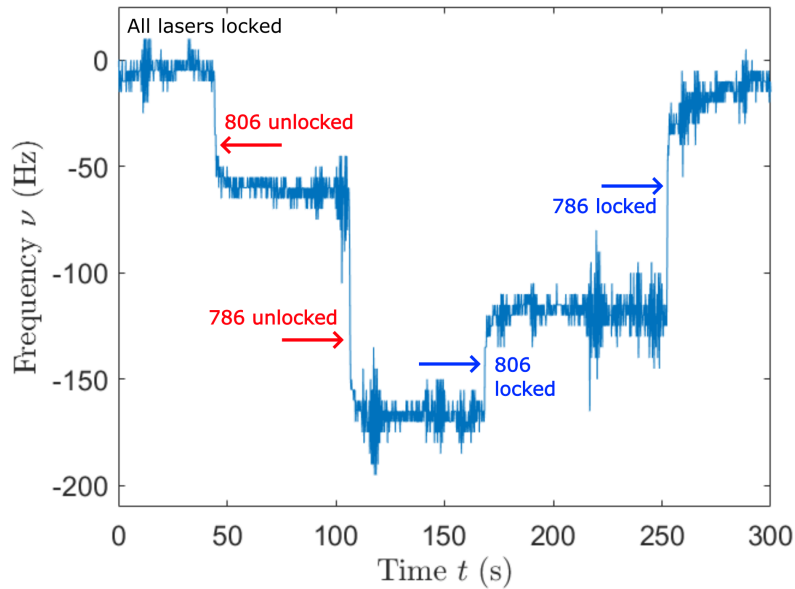


**Figure 6.2.: Frequency jumps due to locking and unlocking the Raman laser at 786 nm and the cavity laser at 806 nm.**

The figure shows the center frequency of the QFC-QSIM 729 nm beat at IQOQI as a function of time. The beat center frequency was set to 0 at  $t = 0$ . At the beginning of the measurement, three lasers are locked to the cavity: the new Ti:Sa laser at 729 nm, the Raman laser at 786 nm and the cavity laser at 806 nm. The arrows point to frequency jumps that occur when locking and unlocking the 786 nm and 806 nm lasers. The average frequency jump caused by locking/unlocking of each laser is shown in Equation Array (6.6). One measurement point was taken every 200 ms.

The method to extract estimates for the beat center frequency changes when locking/unlocking each laser is now explained. First, constant functions were fitted through the individual frequency plateaus in Figure 6.2, giving an average value for each plateau. Then, the frequency jumps  $\nu_{j,\lambda}$  due to locking and unlocking of the 786 nm and 806 nm lasers were calculated by subtracting the constant values above and below the jump. Finally, an average was taken between locking and unlocking for each laser. There is no statistically significant difference in the frequency jump between locking and unlocking in each case. The average frequency for each plateau is given in Table 6.2. The analysis showed that locking and unlocking of the

786 nm and 806 nm lasers lead to QFC-QSIM beat center frequency jumps  $\nu_{j,\lambda}$  (the index  $\lambda$  indicates the laser wavelength) and thus estimated locked new Ti:Sa frequency jumps of

$$\begin{aligned}\nu_{j,786} &= 105(2) \text{ Hz} \\ \nu_{j,806} &= 53(2) \text{ Hz}.\end{aligned}\tag{6.6}$$

We expect that the majority of frequency change comes from the change in radiation pressure as described in [71], however heating or cooling of the cavity mirrors due to the laser power change may contribute to the round edges after each frequency jump.

**Table 6.2.: Frequency plateaus between frequency jumps.** Estimates for the average frequencies during the plateaus in Figure 6.2, obtained by fitting a constant function through the plateaus.

Time Range (s)	Average Frequency (Hz)
0 - 40	-4.6(8)
50 - 100	-60.7(6)
110 - 160	-167(1)
180 - 250	-118(1)
260 - 300	-15(1)

### Beat frequency shift due to a controlled change in the 729 nm light field

It was examined how much the QFC-QSIM beat center frequency shifts if the new Ti:Sa laser itself changes in intensity. For that, the  $\lambda/2$  plate in front of the EOM in Figure 5.7 was rotated so that the cavity-incident 729 nm laser power was increased by  $P_{j,729} = 30(2) \mu\text{W}$ , from approximately  $40 \mu\text{W}$  to approximately  $70 \mu\text{W}$ . In Figure 6.3, the influence of this power increase on the beat center frequency is shown. Due to manual rotation of the  $\lambda/2$  plate, a fluctuation in beat center frequency happened before the jump. The approach to extract the jump value was therefore to fit a linear function through the data points before the jump and extrapolate the frequency value to the time of jump which is estimated to be at  $t = 111$  s. To find the frequency after the jump, a constant function was fitted from  $t = 117$  s to  $t = 150$  s. By subtracting the frequencies before and after the jump the absolute frequency shift could be calculated to be  $\nu_{j,729} = 335(6)$  Hz.

At this point we have estimates for how much the QFC-QSIM 729 nm beat is shifted due to power changes in each of the three laser fields inside the cavity. We can now use that information to make predictions about how intensity fluctuations in those laser fields will translate into broadening of the locked new Ti:Sa laser frequency. Specifically, radiation pressure on the cavity mirrors (Eq. (3.12)) is directly proportional to laser intensity and thus power  $P$ . It follows from this consideration that when a frequency jump  $\nu_{j,\lambda}$  can be related to a power jump  $P_{j,\lambda}$ , a frequency fluctuation  $\Delta\nu$  is related to a power fluctuation  $\Delta P$  via

$$\frac{\Delta P}{P_{j,\lambda}} = \frac{\Delta\nu}{\nu_{j,\lambda}}.\tag{6.7}$$

The power jump  $P_{j,\lambda}$  and the subsequent frequency jump of the center of the locked laser  $\nu_{j,\lambda}$  are the reference values. The expected frequency fluctuations  $\Delta\nu$  in the QFC-QSIM beat can then be calculated by measuring the power fluctuations  $\Delta P$  of the individual lasers as done in the next section.

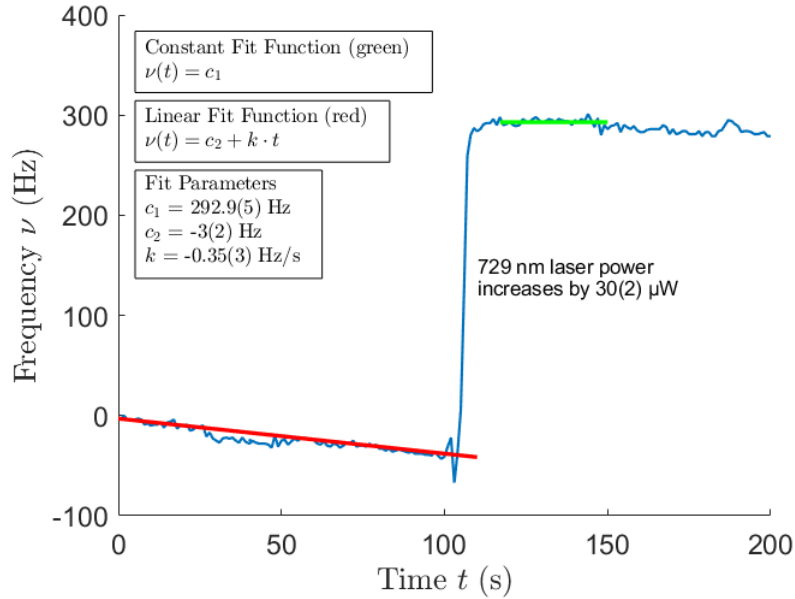


**Figure 6.3.: Frequency jump due to a change in the new Ti:Sa laser intensity at 729 nm.** The figure shows the center frequency of the QFC-QSIM 729 nm beat as a function of time. The frequency jump at around 110 s happened because the new Ti:Sa’s laser cavity-incident power increased by  $30(2) \mu\text{W}$ . The beat center frequency was set to 0 at  $t = 0$ . One measurement point was taken every 1 s, the data points are depicted in blue. In order to calculate the frequency jump the beat center frequency values before and after the jump were subtracted. For that a linear (red) and a constant (green) fit function was used. The linear function was chosen so that the frequency before the jump could be extrapolated to  $t = 111$  s. Uncertainties of the parameters are with respect to the 67% ( $\pm 1\sigma$ ) confidence level.

### 6.2.2. Intensity fluctuations of the three lasers

In Figure 6.4, the measured cavity-incident powers of the 729 nm new Ti:Sa laser, the 786 nm Raman laser and the 806 nm cavity laser are shown as a function of time, using a *Thorlabs S130C* power meter. For the 729 nm laser the measurement time was 21.6 min, for the 786 nm and 806 nm lasers the measurement time was 15 min. A power measurement of the locked lasers in transmission is not presented as the laser power in transmission of the cavity was so low for each laser that the power meter signal seemed to be dominated by background light noise. In Table 6.3, the power jumps  $P_{j,\lambda}$ , frequency jumps  $\nu_{j,\lambda}$  and by using Eq. (6.7) the anticipated locked new Ti:Sa laser’s frequency fluctuations per  $\mu\text{W}$  of power fluctuations are collected for each laser. As previously stated, when a laser is locked, the light field inside the reference cavity jumps from zero to a finite power that is determined by the power of the cavity-incident light. As a consequence, the mean values of the 786 nm and the 806 nm laser cavity-incident powers were used as the power jumps  $P_{j,786}$  and  $P_{j,806}$ .

Using the linear relation between frequency and power in Eq. (6.7) and the frequency fluctuations per  $\mu\text{W}$  of power fluctuations in Table 6.3, it is possible to determine the predicted

change of the new Ti:Sa laser frequency had it been locked over the course of the power measurements. The predicted frequency fluctuations of the new Ti:Sa laser frequency due to the inter-cavity intensity fluctuations in the 729 nm, the 786 nm and the 806 nm lasers is depicted in Figure 6.5. The red lines indicate a change in new Ti:Sa laser frequency by  $\pm 1$  Hz. If the fluctuations in any one plot go beyond the red lines, then they will cause the 729 nm new Ti:Sa laser to fluctuate by more than  $\pm 1$  Hz.

The conclusion is that the intensities of the lasers need to be stabilized in order to achieve a new Ti:Sa laser's linewidth of 1 Hz or below in the long term. Ideally, the lasers should be intensity stabilized so that the new Ti:Sa laser frequency changes much less than  $\pm 1$  Hz over the course of several minutes or even longer. Using the values from Table 6.3, this stabilization can be achieved if the power fluctuations are in the regime of below  $\sim 100$  nW. Given the mean powers of tens of  $\mu\text{W}$ , this corresponds to a fractional intensity stabilization at the level of 0.01 — 0.001.

**Table 6.3.: Predicted frequency fluctuations of the locked new Ti:Sa laser frequency due to laser intensity fluctuations in the reference cavity.** The first line shows the power jumps  $P_{j,\lambda}$  of the three different lasers that can be locked to the reference cavity. For the new Ti:Sa laser at 729 nm the power jump is obtained by rotating a  $\lambda/2$ -plate, for the Raman laser at 786 nm and the cavity laser at 806 nm the power jumps are the mean cavity-incident powers. The table also gives the jumps in the QFC-QSIM beat center frequency. These frequency jumps can be seen in Figure 6.2 due to the Raman laser at 786 nm and the cavity laser at 806 nm and in Figure 6.3 due to the new Ti:Sa laser at 729 nm. Using Eq. (6.7), the locked new Ti:Sa laser's frequency change per 1  $\mu\text{W}$  of power change are calculated. The calculated values are stated in the third line.

Lasers	729 nm	786 nm	806 nm
Power Jump $P_{j,\lambda}$ ( $\mu\text{W}$ )	30(2)	14.5(9)	225(2)
Frequency Jump of QFC-QSIM beat $\nu_{j,\lambda}$ (Hz)	335(6)	105(2)	53(2)
Predicted new Ti:Sa Frequency Fluctuations (Hz/ $\mu\text{W}$ )	11.1(9)	7.2(6)	0.24(1)

## 6. Results at IQOQI

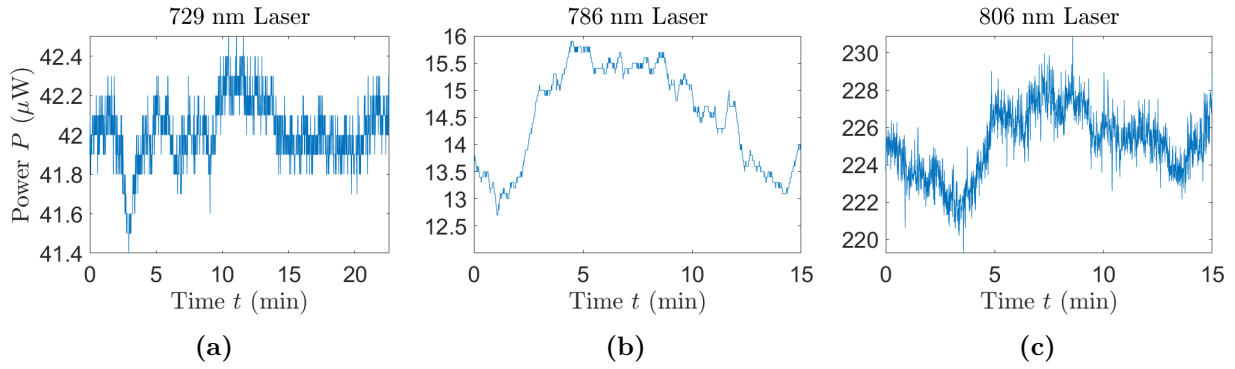


**Figure 6.4.: Power fluctuations of three laser fields without intensity stabilization.** Recorded power of the (a) new Ti:Sa laser at 729 nm, the (b) Raman laser at 786 nm and the (c) cavity laser at 806 nm in front of the reference cavity of Figure 5.7. A *Thorlabs S130C* power meter was used and one data point was taken every 500 ms.

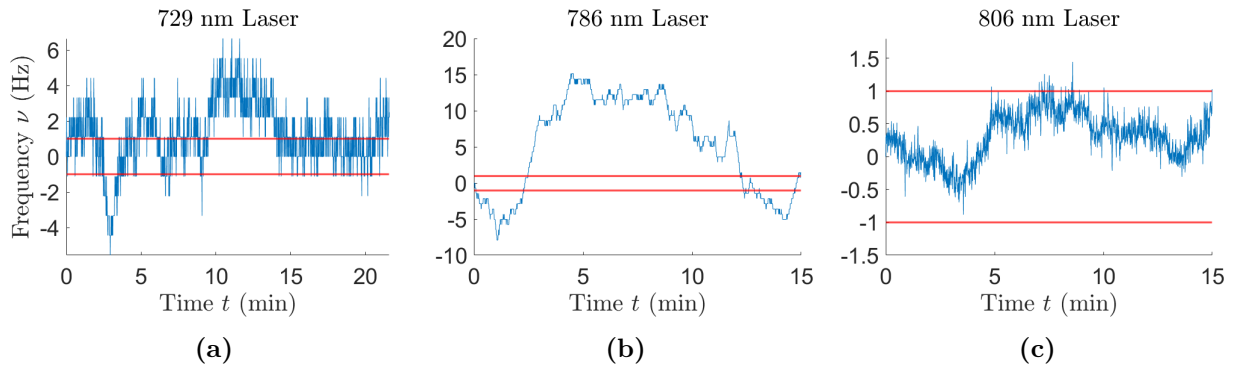


**Figure 6.5.: Predicted change in the new Ti:Sa laser frequency at 729 nm due to measured power fluctuations in three different laser fields.** By using Eq. (6.7) and the data from Table 6.3, the change of the new Ti:Sa laser frequency at 729 nm due to intensity fluctuations of the locked (a) new Ti:Sa laser at 729 nm, the (b) Raman laser at 786 nm and the (c) cavity laser at 806 nm can be calculated from the data in Figure 6.4. The two red lines in each figure indicate the limits above and below which the new Ti:Sa laser frequency is predicted to change by  $\pm 1$  Hz. The new Ti:Sa laser frequency was set to 0 at  $t = 0$  and one data point is shown every 500 ms.

## 7. Results at UIBK

After the move of our laboratory to UIBK, the experimental setup of the new Ti:Sa laser was developed into the one presented schematically in Figure 5.2. The first step was to implement intensity stabilization for all three lasers that should be locked to the reference cavity, that is the new Ti:Sa laser at 729 nm, the Raman laser at 786 nm and the cavity laser at 806 nm. The second step was the installation of a fiber noise cancellation (FNC) setup for the 5 m long fiber that connects the laser breadboard and the cavity breadboard. In Section 7.1, the effect of the intensity stabilization feedback loop on the three laser powers is presented. In Section 7.2, the performance of the FNC feedback loop and the consequences for the new Ti:Sa's laser linewidth are presented. After engaging intensity stabilization and FNC, the frequency stability of the new Ti:Sa laser was measured. Specifically in Section 7.3, a beat measurement with fiber-noise-canceled QSIM light and a three-cornered hat measurement involving both the QSIM and Linear lasers are presented. Next, Ramsey experiments on a single  $^{40}\text{Ca}^+$  ion were conducted at UIBK using the new Ti:Sa laser, providing an alternative characterization of the laser linewidth. The results of the Ramsey experiments are summarized in Section 3.2.2. None of the linewidth measurements up to this point revealed a sub-10 Hz linewidth. Section 7.5 reports on our efforts that finally led to a linewidth for the new Ti:Sa laser below 10 Hz.

### 7.1. Intensity Stabilization Performance

Three intensity stabilization systems were installed and characterized, one for the new Ti:Sa laser at 729 nm, one for the Raman laser at 786 nm and one for the cavity laser at 806 nm. All three systems stabilized the intensity measured by a photodiode on the cavity breadboard, close to the reference cavity on the side from which each laser enters. The photodiodes in question, all *Thorlabs PDA36A2*, are denoted “I-PD 729”, “I-PD 786” and “I-PD 806” in Figure 5.5. The intensity stabilization circuit for the new Ti:Sa laser is described in Figure 5.3. The circuits for the 786 nm and 806 nm lasers are similar but lack the additional FNC feedback loop.

In analogy to the measurements that are presented in Figure 6.4, the stabilized powers of the 729 nm, 786 nm and 806 nm lasers were measured again in front of the reference cavity, and the results are shown in Figure 7.1. In analogy to the approach in Subsection 6.2.2, by using the linear relation between frequency jumps and power jumps in Eq. (6.7) and the frequency fluctuations per  $\mu\text{W}$  of power fluctuation in Table 6.3, it is possible to calculate the predicted change of the new Ti:Sa laser's frequency due to the power fluctuations remaining in the laser fields over the course of the power measurement. These predicted changes to the new Ti:Sa laser frequency are shown in Figure 7.2. The red lines indicate a change in frequency by  $\pm 1$  Hz. The data reveals that the intensity stabilized lasers are predicted to lead to frequency changes of the new Ti:Sa laser frequency that are well below  $\pm 1$  Hz, as is required.

The laser powers in Figure 7.1 still show drifts in the regime of  $\sim 100$  nW over tens of minutes. We are not sure where these power drifts in the intensity-stabilized lasers come from. One

## 7. Results at UIBK

possible explanation could be that the reference voltage of the intensity stabilization modules slowly drifts over time. Since the effect of slowly drifting powers presents no significant barrier to obtain a sub-1 Hz linewidth for the new Ti:Sa laser, this was not investigated further.

Comparing the power values in Figure 6.4 with the power values in Figure 7.1 shows that the mean values of the cavity-incident laser powers used at IQOQI and UIBK are not the same. The changes in those powers were not made for any particular reason. As far as we know, the lasers lock equally as well for the different mean power values.

Another convenient side effect of the laser intensity stabilization circuit is that the laser power reaching the cavity can be easily changed. By changing the reference value  $Ref$  of the Intensity Lock module that is shown in Figure 5.3, the laser power that is diffracted by the AOM changes accordingly. Therefore, the intensity stabilization circuit can be used as a regulator and also as a servo for the cavity-incident laser power.

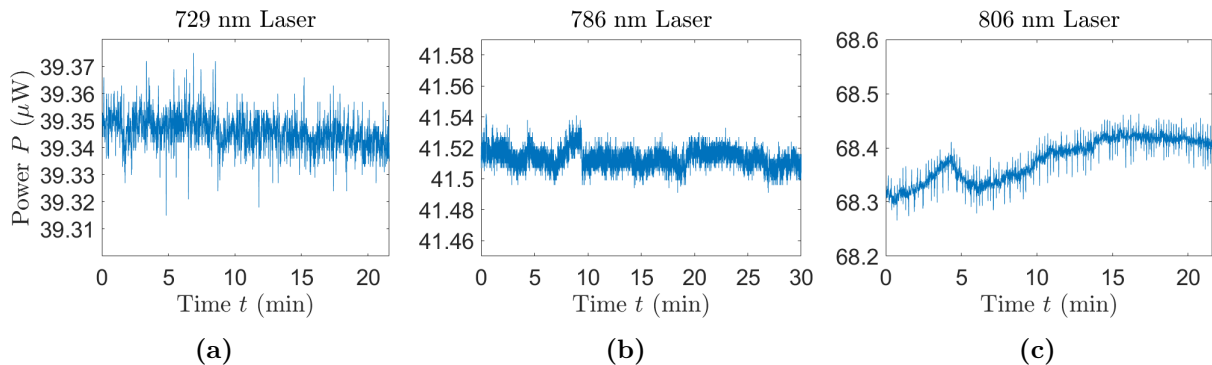


**Figure 7.1.: Power fluctuations of three intensity-stabilized lasers.** Recorded power of the (a) new Ti:Sa laser at 729 nm, the (b) Raman laser at 786 nm and the (c) cavity laser at 806 nm in front of the reference cavity when the lasers are intensity stabilized. A *Thorlabs S130VC* power meter was used. For the 729 nm laser and the 806 nm laser one data point was taken every 500 ms, for the 786 nm laser one data point was taken every 100 ms.

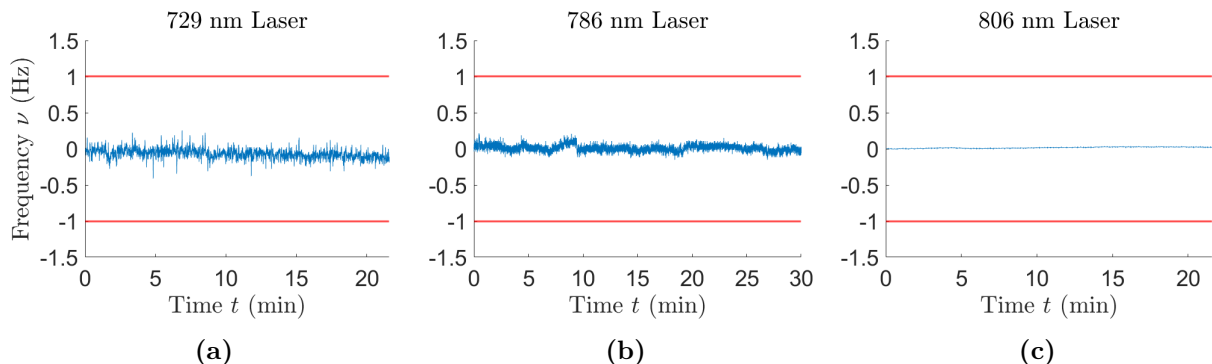


**Figure 7.2.: Predicted change in the new Ti:Sa laser frequency at 729 nm due to cavity power fluctuations due to three different intensity-stabilized laser fields.** By using Eq. (6.7) and the data from Table 6.3 the change of the new Ti:Sa laser frequency at 729 nm due to intensity fluctuations of the locked (a) new Ti:Sa laser at 729 nm, the (b) Raman laser at 786 nm and the (c) cavity laser at 806 nm lasers can be calculated from the data in Figure 7.1 when the lasers are intensity stabilized. The two red lines in each figure indicate the limits above and below which the beat center frequency has changed by  $\pm 1$  Hz. The laser frequency was set to 0 at  $t = 0$ . For the 729 nm laser and 806 nm laser one data point is shown every 500 ms, for the 786 nm laser one data point is shown every 100 ms.

## 7.2. Fiber Noise Cancellation Performance

Fiber noise cancellation (FNC) for the 5 m long *Thorlabs P5-630PM-FC-5* fiber that connects the laser breadboard and the cavity breadboard was installed (Figure 5.2). The FNC setup was built as depicted in Figure 5.3. In Figure 7.3, the FNC beat is shown in logarithmic scale. The center peak in Figure 7.3 is about 50 dBm higher than any other data point in the spectrum. The spectrum looks qualitatively comparable to the one presented in [57]. The bumps left and right of the center with the maximum at around  $\pm 70$ -80 kHz are likely *servo bumps* that are created when the feedback loop is applying positive rather than negative feedback in a certain frequency zone. The peaks at approximately  $\pm 140$  kHz are likely either due to radio frequency pick-up or due to a resonance in the actuator, the AOM. To obtain the linewidth of the center peak, a new beat measurement was taken with the spectrum analyzer. The measured beat is shown in linear scale in Figure 7.4. A Gaussian fit function of the type Eq. (6.1), but without the offset  $d$ , was chosen because an  $R^2$  test gave a coefficient of determination of  $R^2 = 1$  for a Gaussian. The FWHM of the Gaussian curve and thus the linewidth of the beat signal can be calculated from the standard deviation (parameter  $c$  of the fit function) to be

$$\Delta\nu_{\text{FNC}} = 0.9919(2) \text{ Hz.} \quad (7.1)$$

The  $R^2$  value and the linewidth suggest that the beat signal is resolution limited by the spectrum analyzer, and the linewidth of the actual FNC beat is likely  $< 1$  Hz. We therefore conclude that the FNC feedback loop removes phase noise so that the laser light does not have a contribution to its linewidth  $> 1$  Hz due to fiber noise.

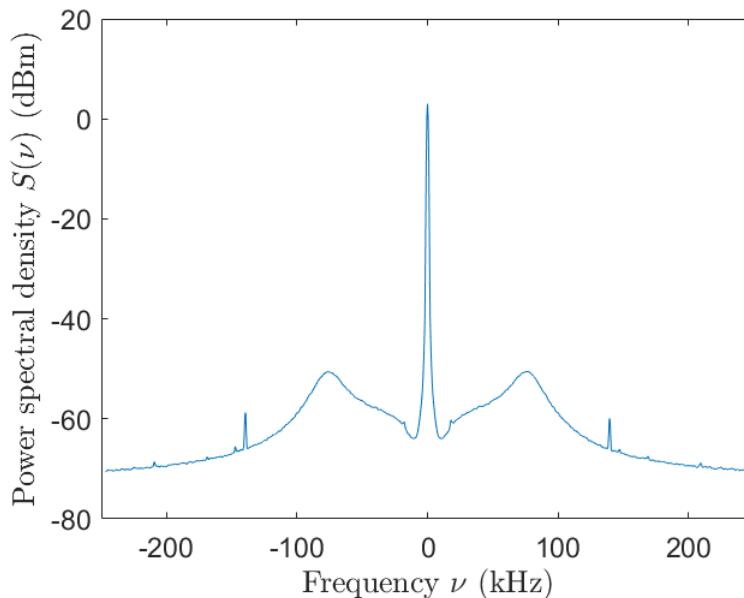


**Figure 7.3.:** Spectrum of the new Ti:Sa laser's FNC beat displayed in a logarithmic scale. The beat signal was detected by a *Thorlabs PDA10A2* photodiode. The data was taken by a *R&S FSV 3004* spectrum analyzer, settings: Resolution bandwidth 1 kHz, video bandwidth 1 kHz, sweep time 2.11 s, frequency span 500 kHz.

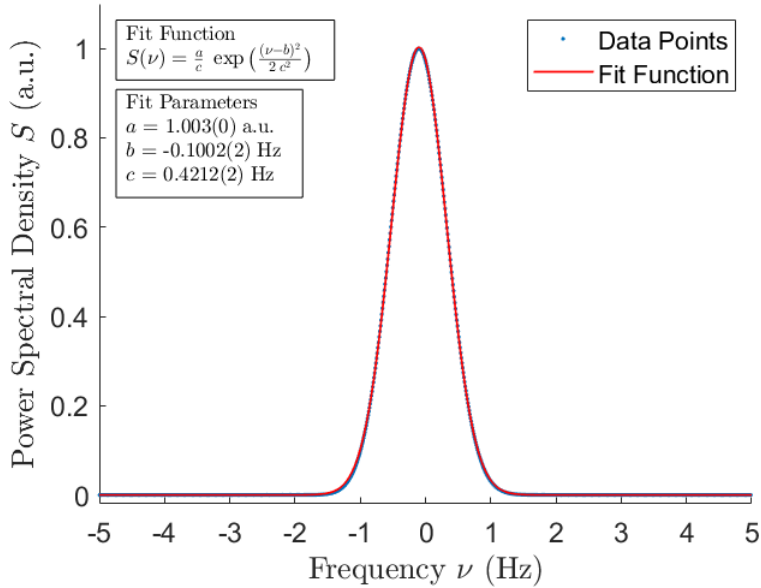


**Figure 7.4.:** Spectrum of the new Ti:Sa laser’s FNC beat displayed in linear scale. The beat signal was detected by a *Thorlabs PDA10A2* photodiode as depicted in Figure 5.3. The data was taken by an *R&S FSV 3004* spectrum analyzer, settings: Resolution bandwidth 1 Hz, video bandwidth 1 Hz, sweep time 2.11 s, frequency span 10 Hz. A resolution and video bandwidth of 1 Hz is the minimum value that can be chosen on this spectrum analyzer model. The data points are fitted by a Gaussian model. Uncertainties of the parameters are with respect to the 67% ( $\pm 1\sigma$ ) confidence level.

### A comment on spectrum analysis and the *R&S FSV 3004* spectrum analyzer

To explain the distribution of data points in the beat measurement in Figure 7.4 and the following beat measurements, a comment on spectrum analysis in general and specifically the *R&S FSV 3004* spectrum analyzer is now given. First, the two concepts of *resolution bandwidth* and *video bandwidth* are paraphrased from [77]: The resolution bandwidth (RBW) is the frequency span of the filter that is applied to the input signal by the spectrum analyzer. A smaller resolution bandwidth provides a finer frequency resolution. Another factor that affects the displayed trace is the video bandwidth (VBW). Video filtering is mathematically equivalent to averaging neighboring data points, so basically a mean is calculated from several data points. The main effect of the VBW filter is to smooth the trace.

For every beat trace that was recorded in the master project, the *R&S FSV 3004* spectrum analyzer had 1000 points along the frequency axis at its disposal, independent of the frequency span. If the frequency span is  $S$ , the frequency spacing between two points is  $\Delta = S/1000$ . However, if  $\text{VBW} > \Delta$ , there are not enough data points for the 1000 available points the spectrum analyzer wants to display. So, the spectrum analyzer interpolates between the data points to use all 1000 available points. This interpolation can be seen in Figure 7.4: With a span of 10 Hz and a video bandwidth of 1 Hz, only 10 data points can represent the photodiode signal. However, as the spectrum analyzer wants to display 1000 points, 990 points are used for interpolation. After the interpolation, the spectrum analyzer acts as if the trace includes 1000 data points, when in fact it does not. Unfortunately we only discovered the inner workings of the *R&S FSV 3004* months after data acquisition. In the case of Figure 7.4, the interpolated points were kept for two reasons. First, the beat demonstrates what this comment on the spectrum analyzer wants to convey about interpo-

lation. Second, for the FNC beat it is sufficient to have an indication that the beat linewidth is below 1 Hz. It seems that the interpolation of data does not change the validity of the statement that the FNC feedback loop removes phase noise so that the laser light does not have a contribution to its linewidth  $> 1$  Hz due to fiber noise. In all other beat measurements that were taken by the *R&S FSV 3004* and used in this thesis, the points that were used for interpolation are removed.

Diametrically, a problem arises when the video bandwidth is chosen too low for the feature that should have been resolved, for example, a peak. In this case, the smoothing of the trace for which the VBW is responsible for does not work, and the acquired data is rugged. In the case of a rugged beat due to a low video bandwidth, we post-processed the data by binning several data points into one point, which effectively increases the video bandwidth. It turned out that the optimal settings would be  $\text{VBW} = \Delta$  at the spectrum analyzer, so that no interpolation happens, and then the ratio  $\text{VBW}/\Delta$  is increased post-measurement to a value between 1 and 10 through binning, depending on the feature in the spectrum that should be resolved.

The frequency resolution of the *Rohde and Schwarz FSV 3004* spectrum analyzer is 0.01 Hz according to the data sheet, so error bars cannot be visible along the frequency axis in the following figures. The maximum uncertainty of level measurement is 0.07 dB ( $1 \sigma$ ), so error bars are of the size of the data points and cannot be visible along the power spectral density axis in the following figures.

### 7.3. Frequency Stability of the new Ti:Sa laser at UIBK

The measurements in the previous two sections show that because of stabilization, intensity noise and fiber noise contribute to the new Ti:Sa laser's linewidth at a level below 1 Hz. A beat measurement with fiber-noise canceled light from the QSIM laser (now several hundred meters away) was conducted to obtain an updated upper limit for the new Ti:Sa linewidth at UIBK. Afterwards, a three-cornered hat measurement was performed using the QSIM and Linear lasers to obtain the linewidth of the new Ti:Sa laser and additionally a value for the new Ti:Sa laser's absolute frequency drift over time. Experimental details and results are presented in this section.

#### FALC settings at UIBK

All three actuators, the slow Piezo, the fast Piezo and the intracavity EOM were engaged to frequency-stabilize the new Ti:Sa laser at UIBK. A description of the three actuators and the different constituents of a FALC can be found in Subsection 5.3.1. FALC1 gives feedback to the fast Piezo and the slow Piezo elements, FALC2 gives feedback to the intracavity EOM. The chosen locking parameters at FALC1 and FALC2 are shown in Table 7.1. The place of FALC1 and FALC2 in the experimental setup at UIBK can be seen in Figure 5.2.

In comparison to the controller settings that were used in IQOQI (Table 6.1) the frequency ranges of the SLI and FLI at FALC1 were reduced by a factor of 2-3, while the frequency range of the FLD was reduced by a factor of 10. As the fast Piezo actuator can respond to frequencies in the correction signal of up to 100 kHz, the FLD was contributing to the laser lock at UIBK, one improvement over the situation at IQOQI. The XSLI was switched off as *Toptica* suggests to disengage it when the ULI is switched on. The ULI speed was set by choosing the resistor  $R1$  and the capacitor  $C4$ . This setting showed the best trade-off

between a quick yet not too overshooting response of the unlimited integrator. The trade-off was assessed by looking at the output signal of the ULI on an oscilloscope. Further, the full response range of  $\pm 5$  V (which can be realized with a load of  $> 1$  k $\Omega$ ) was chosen for the ULI.

At FALC2, only the FLI and FLD were used to correct for the error signal. The FLD of FALC1 and the FLI of FALC2 thereby fulfill the purpose of what was discussed at the end of subsection 5.3.1: A transition zone in frequency response was established around 100 kHz where two actuators correct for the frequency components in the error signal. The FLD of FALC2 was chosen to correct in a regime up to the maximum frequency of the intracavity EOM, which is at 3 MHz. This choice means that the differentiator can quickly respond to high frequency noise that might e.g., arise from a metal-on-metal clinking sound. The most stable feedback loop was obtained when the main gain MG of both FALC1 and FALC2 was set to 5. In this configuration it is possible to lock the new Ti:Sa laser to a TEM00 mode of the reference cavity for several days. Talking and working next to the setup in Figure 5.2 does not unlock the laser if the optical table on which the setup rests is not directly touched with metallic objects.

**Table 7.1.: FALC parameters of the new Ti:Sa laser at UIBK.** FALC1 drives the fast Piezo actuator and the slow Piezo actuator, FALC2 drives the intracavity EOM. The slow Piezo is only driven by the ULI. The FALC-specific acronyms are explained in Subsection 5.3.1. The place of FALC1 and FALC2 in the experimental setup at UIBK can be seen in Figure 5.2.

Element	FALC1	Frequency range	FALC2	Frequency range
SLI	6	110 Hz - 6.5 kHz	10	-
FLI	10	1.4 kHz - 10 kHz	6	30 kHz - 370 kHz
FLD	9	42 kHz - 230 kHz	5	900 kHz - 4.8 MHz
XSLI	6	-	6	-
ULI settings	R1/C4		-	
ULI range	$\pm 5$ V		-	
MG	5		5	

### 7.3.1. Beat measurement with QSIM at UIBK

After engaging FNC and intensity stabilization, QFC-QSIM beats were conducted on the laser breadboard in UIBK. The beat setup is depicted in Figure 5.2 in the blue shaded area. The QSIM light was transported from IQOQI via a 510 m long polarization-maintaining (PM)-fiber to the ground floor of Viktor-Franz-Hess building at UIBK and from there to the first floor via a 140 m long non-PM-fiber. FNC is implemented on the combined 650 m long fiber, with the feedback being implemented at IQOQI, laboratory 1.

The signal from the QFC-QSIM beat photodiode on UIBK first floor was analyzed by an *R&S FSV 3004* spectrum analyzer. In total, three traces were taken in series by the spectrum analyzer. For each beat, the resolution bandwidth was 1 Hz, the video bandwidth was 1 Hz, the sweep time was 5 s and the frequency span was 1 kHz. To reduce the ruggedness of the beat trace, 10 neighboring data points were binned into one, yielding a spectral resolution of 10 Hz and so effectively increasing the video bandwidth to 10 Hz. Figure 7.5 presents one of the QFC-QSIM beats as a representative. A Gaussian curve of the form Eq. (6.1), but without the offset  $d$ , was used for every beat and the average linewidth of the three curves

was calculated using Eq. (6.2). An  $R^2$  test of the data in Figure 7.5 yielded a value of 0.94 for both a Gaussian curve and a Lorentzian curve. A Gaussian curve was chosen so that a more intuitive comparison to the QFC-QSIM beat that was taken at IQOQI is possible. For the representative beat shown in Figure 7.5 the linewidth is  $\Delta\nu_1 = 214(5)$  Hz. The other two linewidths read  $\Delta\nu_2 = 235(7)$  Hz and  $\Delta\nu_3 = 271(7)$  Hz, yielding an average linewidth of

$$\Delta\nu = 240(29) \text{ Hz.} \quad (7.2)$$

The three linewidths are not consistent within their uncertainties, and the beat linewidth seemed to fluctuate on the timescale of seconds. The uncertainty in Eq. (7.2) is calculated as half the range of the beat linewidths. Using the standard deviation of the individual beat linewidths would give an uncertainty of 28 Hz for the average beat. The obtained beat linewidth is larger than the one measured at IQOQI (Eq. (6.3), 174(12) Hz). As fiber and intensity noise could be ruled out as the culprits that increase the linewidth significantly above 1 Hz, something else had to be responsible for the linewidth broadening.

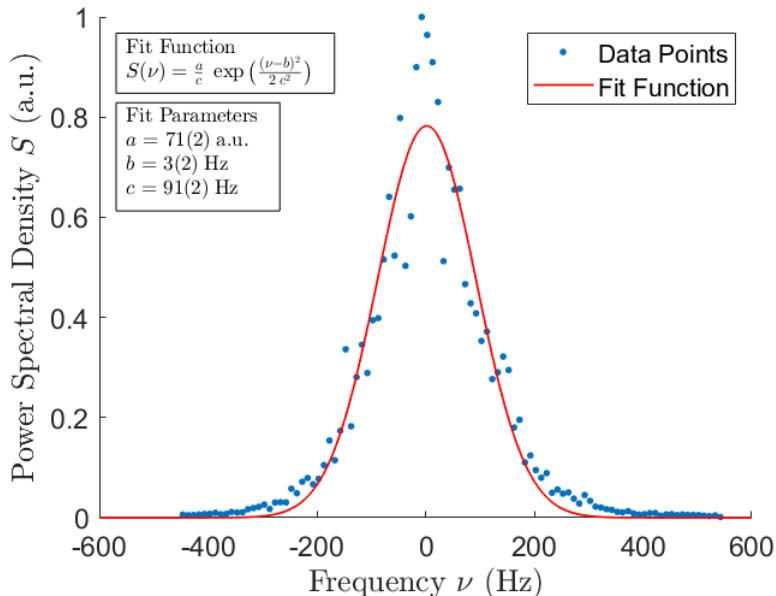


**Figure 7.5.: QFC-QSIM beat at 729 nm at UIBK.** This is one representative of the three beats that were used to get the value for the beat linewidth in Eq. (7.2). The beat center frequency is set to 0 and the power spectral density is normalized to 1. The data points are fitted by a Gaussian model. The data was taken by an *R&S FSV 3004* spectrum analyzer, settings: Resolution bandwidth 1 Hz, video bandwidth 1 Hz, sweep time 5 s, frequency Span 1 kHz. Ten neighboring data points were binned into one post-measurement to reduce fluctuations in the plot, so effectively the video bandwidth is 10 Hz. The linewidth (FWHM) of this example beat calculates to  $\Delta\nu_1 = \sqrt{8 \ln(2)} \cdot c = 214(5)$  Hz. Uncertainties of the parameters are with respect to the 67% ( $\pm 1\sigma$ ) confidence level.

### 7.3.2. Subsequent changes to the experimental setup

The QFC-QSIM beat presented in the previous subsection (Figure 7.5) was measured on Thursday, March 3rd 2022 and the three-cornered hat measurement was taken around one month later. Between the QFC-QSIM beat and the three-cornered hat measurement, the following changes were made to the laser and the PDH lock setup:

## 7. Results at UIBK

- For the PDH technique, the EOM should only modulate the light’s phase, not the amplitude. The *residual amplitude modulation* introduced into the 729 nm laser light by the EOM in Figure 5.2 was minimized. The concept of residual amplitude modulation that leads to light amplitude modulation because of an EOM is explained in [78, 79]. A general explanation on how an EOM can modulate the amplitude of light is given in [80].
- The *Minicircuits BLP-10.7* low-pass filter in front of the RF amplifier (Amp. PD in Figure 5.2) that amplifies the photodiode signal in the PDH lock was changed to a *Minicircuits BBP-10.7+* band-pass filter after the amplifier. The idea was to reduce low frequency electronic noise that arrives at the FALCs with this change.
- The PDH error signal was optimized by adjusting the relative phase  $\phi$  between the signal from the reflection photodiode and the local oscillator signal. The relative phase was adjusted changing the cable length from the function generator to the EOM.
- Every electronic device that is used in the new Ti:Sa laser lock setup was replugged to one socket that is used for nothing else. The idea behind this effort was to remove ground loops that create  $n \cdot 50$  Hz ( $n \in \mathbb{N}$ ) noise.
- Electronic devices in the rack shown in Figure 5.3 that were not used for FNC or intensity stabilization were removed. The idea was to reduce electronic noise at  $n \cdot 50$  Hz.
- The *Thorlabs LDS 1212* power supplies for the reflection, transmission and intensity stabilization photodiodes (“R-PD”, “T-PD” and “I-PD” in Figure 5.5) were removed. Power supplies for photodiodes are known to introduce  $n \cdot 50$  Hz noise into the environment [81]. An *EA-PS 3016-10 B* laboratory power supply was then used to give 12 V of constant voltage to the photodiodes.
- It was discovered that the *Thorlabs P5-630PM-FC-5* fiber that connects the laser and cavity breadboards was introducing noise into the error signal when it was jiggled by hand, even when FNC was engaged. The assumption was that the fiber is broken, and it was replaced by a fiber of the same model. The new fiber introduced less noise upon jiggling.

After these changes, the time trace of the error signal showed a lower peak-to-peak amplitude, which can be interpreted as a reduction in frequency fluctuations around the resonance frequency when looking at Figure 4.5. However, repeating the QFC-QSIM beat showed that the linewidth was only slightly below the one that was initially measured at UIBK (Eq. 7.2). Additionally to the permanent changes listed above, the following temporary changes were made between March and April 2022:

- A range of different FALC parameters were explored.
- The reference clock in Figure 5.3 was changed.
- The DDS frequency in Figure 5.3 was changed. We suspected that certain DDS frequencies lead to amplitude modulation on the 729 nm laser light through AOM1 and AOM2. This culminated in the temporary removal of AOM1 from the optical path.
- The function generator’s output voltage in Figure 5.2 was changed, changing the peak-to-peak amplitude of the error signal time trace. The role of the function generator output voltage in the PDH error signal can be found in the Appendix chapter A.

All of these temporary changes were taken back as no difference could be made out in the QFC-QSIM beat linewidth.

### 7.3.3. Three-cornered hat measurement

The QSIM laser is reported to show a sub-10 Hz linewidth [74]. However, to beat with the new Ti:Sa laser, the QSIM light was transported over several hundred meters of optical fiber from IQOQI to the beat setup at UIBK, so one reason for beat linewidth broadening to the  $\sim 100$  Hz regime could have been a faulty fiber noise cancellation setup at the QSIM side. In order to get an absolute measurement of the new Ti:Sa laser’s linewidth, a three-cornered hat measurement was conducted involving a third laser at 729 nm: The “Linear” laser that is stationed on the UIBK ground floor [59], 140 m away by a PM optical fiber. The theory behind the three-cornered hat measurement is given in Subsection 3.2 and our setup for it is depicted in Figure 5.4. The laser pairs were QFC-QSIM, QFC-Linear and QSIM-Linear. With our setup only one beat measurement could be performed at a time.

For all three beat measurements that make up the three-cornered hat measurement, the spectrogram option of the *R&S FSV 3004* spectrum analyzer was used. Here, one beat measurement is taken over the course of the set sweep time, and then another beat measurement immediately follows. The spectrogram option allows both the beat linewidth as well as the drift of the center beat frequency to be extracted from the data. The spectrogram that shows the power spectral density as a function of frequency and time is displayed for the QFC-QSIM beat measurement in Figure 7.6a, for QFC-Linear in Figure 7.7a and for QSIM-Linear in 7.8a. The spectral resolution and thus the effective video bandwidth of each spectrogram was adjusted post-measurement due to the reasons that are given in the comment in Section 7.2. For each spectrogram, different settings on the spectrum analyzer were used, and so different postprocessing had to be done to allow for a proper comparison and analysis of the data.

In Figure 7.6a, the amplitude of the spectrum is strongly fluctuating over time. This is because the QSIM light’s polarization at UIBK first floor fluctuated. The cause for this polarization fluctuation is that the light was transported through a non-PM fiber. Perpendicularly polarized light cannot interfere, and so a beat that includes a laser that is fluctuating in polarization shows fluctuating intensity over time.

Each spectrogram consists of hundreds of beat traces. To extract a linewidth out of each spectrogram, the approach was as follows: First, for a chosen time, ten consecutive beat traces are added up to accumulate data. Gaussian curves of the form Eq. (6.1), but without the offset  $d$ , were used to fit this sum of ten traces. One representative of ten summed up beat traces is shown for the QFC-QSIM beat in Figure 7.6c, for QFC-Linear in Figure 7.7c and for QSIM-Linear in 7.8c. Then, this process is repeated for each laser pair for ten different times equally spread out over the spectrogram, obtaining ten linewidths per laser pair. The average linewidths for each laser pair were calculated by Eq. (6.2). The standard deviation of the individual beat linewidths was taken as the linewidth uncertainty.

The average linewidths for each laser pair are collected in Table 7.2, together with the start times of the spectrogram recordings. Both beats with the new Ti:Sa system involved have a linewidth in the  $\sim 100$  Hz regime, while the QSIM-Linear beat has a  $\sim 10$  Hz linewidth. The individual lasers’ linewidths are calculated using Eq. (3.27) under the assumption of Gaussian statistics. The calculation leads to a complex and thus unphysical linewidth for the Linear laser. We have two possible explanations for this inconsistency. One possible explanation is that even though FNC reduces fiber noise to a sub-1 Hz linewidth on the QSIM laser light through the 510 m of optical fiber to UIBK ground floor, it does not achieve this narrow linewidth over 650 m to UIBK first floor. The second possible reason is that the linewidth of the new Ti:Sa laser fluctuates significantly between the measurements, which are several hours apart as described in Table 7.2, by more than tens of Hz. As a consequence

of this unphysical inconsistency, we refused to further use the calculated linewidths for either the new Ti:Sa laser or the QSIM Ti:Sa laser. The only hesitantly extracted information about the new Ti:Sa laser is that because the QSIM-Linear beat is upper-bounded by 15 Hz and the FNC from UIBK first floor to the QFC-Linear beat was confirmed to work within within  $\sim$  Hz beat linewidth, the new Ti:Sa laser linewidth was in the regime of  $\sim$  100 Hz during these measurements. To learn more about the new Ti:Sa laser’s linewidth, we turned to performing Ramsey experiments with a single  $^{40}\text{Ca}^+$  ion.

**Table 7.2.: Measured beat linewidths for each laser pair in the three-cornered hat measurement.** For each laser pair, 100 beat traces were considered to calculate the average linewidths given in this table, taken from the spectrograms. The spectrograms for laser pairs QFC-QSIM, QFC-Linear and QSIM-Linear are shown in Figure 7.7a, Figure 7.7a and Figure 7.8a respectively. The third column includes the start times of the spectrogram recordings for each laser pair. The experimental setup that allowed for the three-cornered hat measurement is shown in Figure 5.4. The setup for the three-cornered hat measurement does not allow for a simultaneous measurement of all three spectrograms, and all three spectrograms were performed over the course of  $\sim$  24 h. On April 6th, there was no fiber-noise cancelled QSIM light available.

Laser Pair	$\Delta\nu$ (Hz)	Start Time of Spectrogram Recording
QFC - Linear	158(5)	April 6th 2022, 16:00
QFC - QSIM	217(31)	April 7th 2022, 13:30
QSIM - Linear	11(4)	April 7th 2022, 18:15

### 7.3.4. Frequency drift of the new Ti:Sa laser

The drift of each laser pair’s beat center frequency was extracted from the spectrogram by taking the maximum power spectral density value in the spectrum at each point in time. Then, a linear function  $S(\nu) = a + b \cdot \nu$  was fitted to the temporal vector of center frequencies,  $a$  and  $b$  being fit parameters. The drift of the beat center frequency over time and the linear fit can be seen for QFC-QSIM in Figure 7.6b, for QFC-Linear in Figure 7.7b and for QSIM-Linear in Figure 7.8b. The laser pairs’ linear drifts are collected in Table 7.3. The assumption now made, even though the three spectrograms were not taken simultaneously (Table 7.2), was that the linear drifts of the lasers did not change over the course of the three-cornered hat measurement, which is approximately 24 h. Using Eq. (3.28), the *absolute* laser frequency drifts were calculated under this assumption and they are also stated in Table 7.3.

The Linear laser shows no frequency drift within one standard deviation, and it was reported to be stabilized in frequency to a  $^{40}\text{Ca}^+$  ion during the course of the three-cornered hat measurement. By comparing the value of the QSIM Ti:Sa laser drift to the drift of 76 mHz/s reported in [39] in 2012 and taking into account that cavities slow down in expansion as time progresses, the two values are not inconsistent. The new Ti:Sa (QFC) laser shows the strongest frequency drift of -371(3) mHz/s. The drift is also larger than the 202(1) mHz/s (stated with a positive sign) measured by Helene Hainzer in 2017 [52] for the same reference cavity. By investigating the reference cavity’s temperature controller, we found out that the cavity temperature (the  $y(t)$ , speaking in control theory jargon) was drifting in the range of 0.1 K over the course of minutes to hours. A further examination will show whether this drift in temperature is responsible for the new Ti:Sa laser’s increased frequency drift compared to the 2017 drift value.

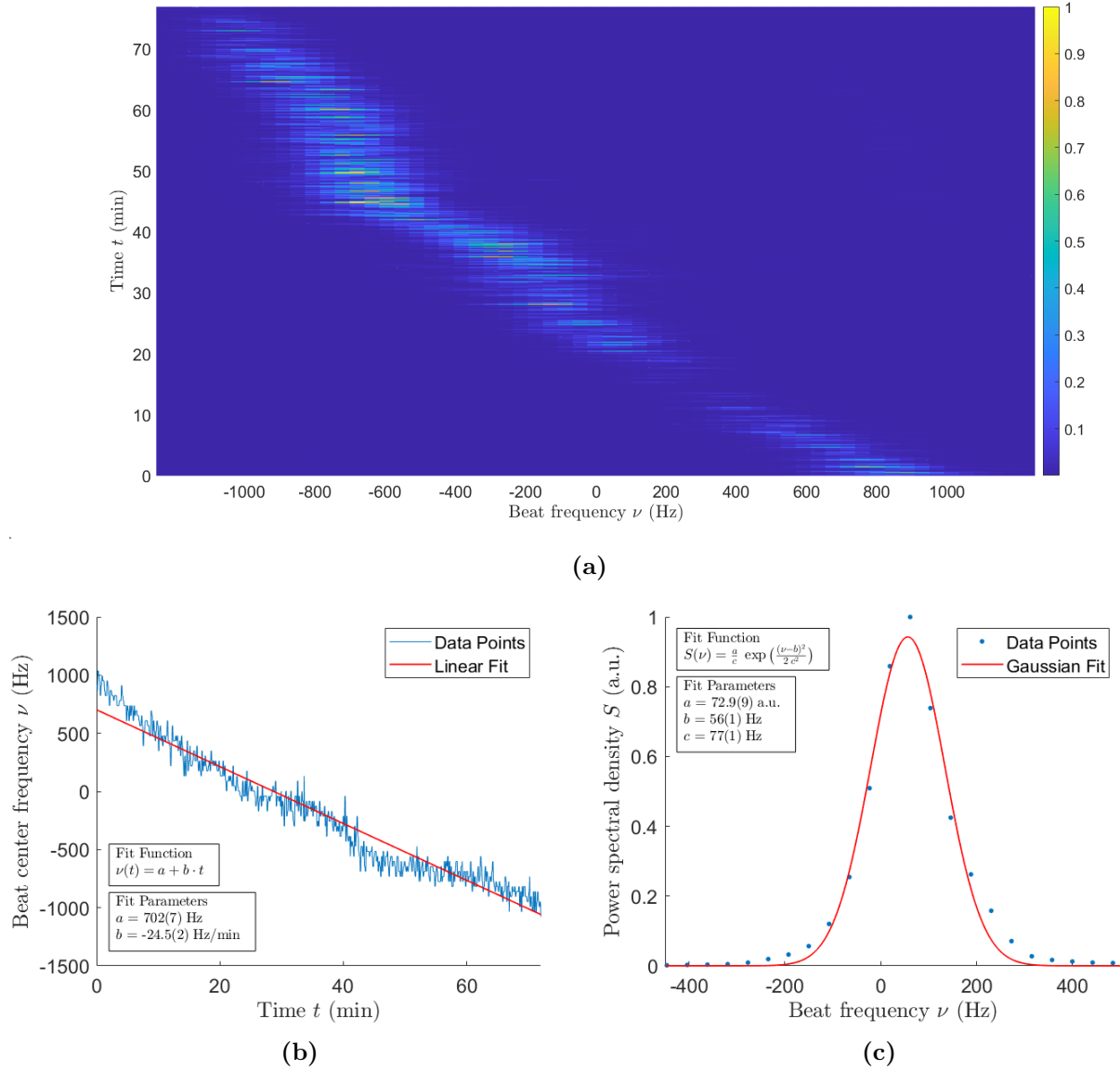


**Figure 7.6.: Results from the three-cornered hat measurement, laser pair QFC-QSIM.** (a) Spectrogram measurement of the QFC-QSIM beat using the *R&S FSV 3004* spectrum analyzer. The spectrogram shows the power spectral density as a function of frequency and time. The bar on the right shows the color for each value of the normalized power spectral density in arbitrary units. The chosen settings on the spectrum analyzer are: Resolution bandwidth 10 Hz, video bandwidth 100 Hz, sweep time 4 s, frequency span 5 kHz. As the spectrum analyzer would interpolate data at a video bandwidth of 100 Hz, only every tenth point was kept. The change in power spectral density over time comes most likely from polarization fluctuations in the QSIM light. (b) Drift of the QFC-QSIM beat center frequency over time. The data is created by plotting the maximum frequency per line in (a) as a function of time. The data is fitted by a linear function and fit parameter  $b$ , the frequency drift, is collected in Table 7.3 (given in mHz/s). (c) This is one of the ten representative beats that were used to get the value for the beat linewidth in Table 7.2. Uncertainties of the parameters are with respect to the 67% ( $\pm 1\sigma$ ) confidence level.

## 7. Results at UIBK

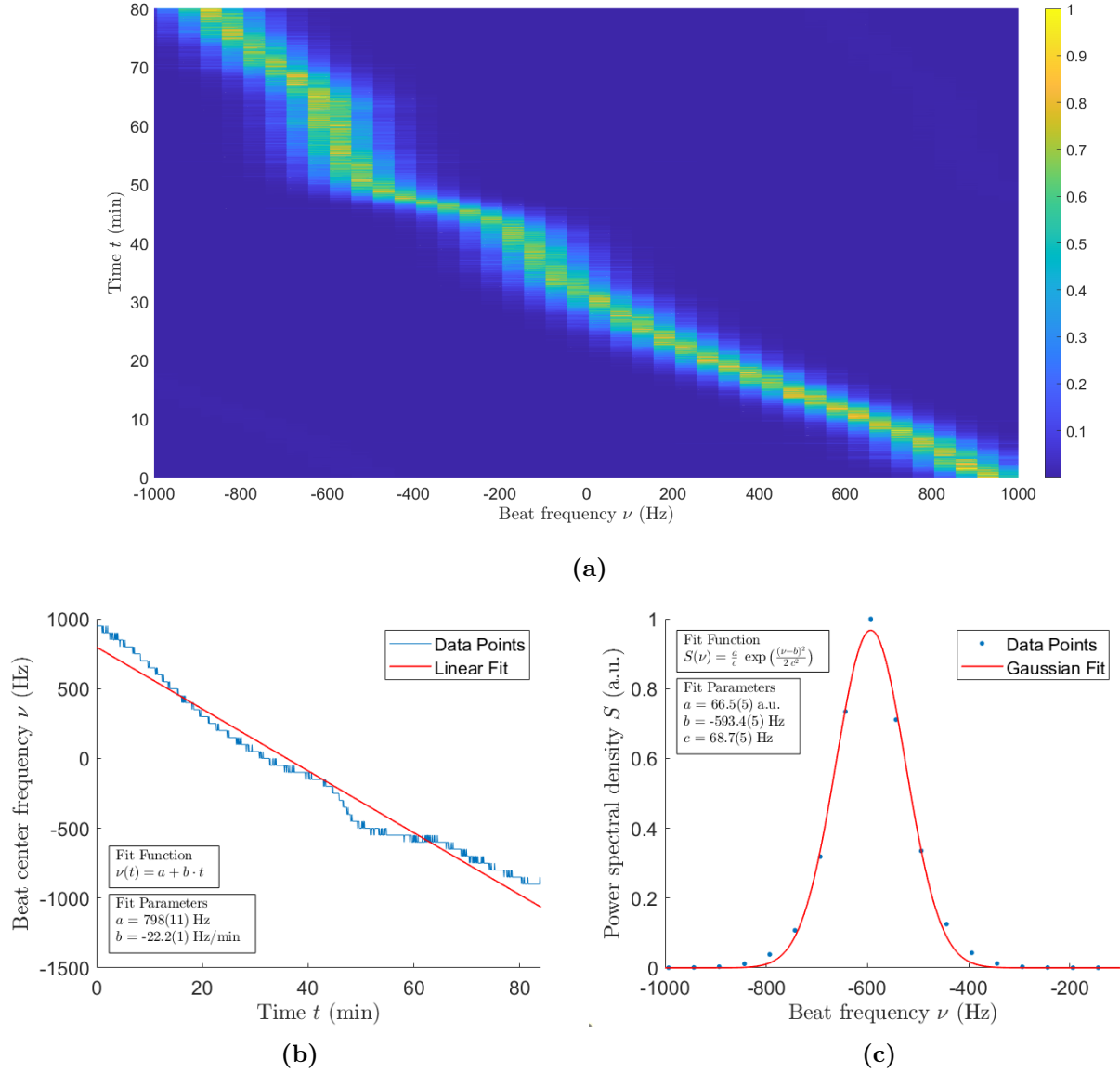


**Figure 7.7.: Results from the three-cornered hat measurement, laser pair QFC-Linear.** (a) Spectrogram measurement of the QFC-Linear beat using the *R&S FSV 3004* spectrum analyzer. The spectrogram shows the power spectral density as a function of frequency and time. The bar on the right shows the color for each value of the normalized power spectral density in arbitrary units. The chosen settings on the spectrum analyzer are: Resolution bandwidth 3 Hz, video bandwidth 3 Hz (10 data points were binned into one post-measurement, so effectively the video bandwidth is 30 Hz), sweep time 4 s, frequency span 5 kHz. (b) Drift of the QFC-Linear beat center frequency over time. The data is created by plotting the maximum frequency per line in (a) as a function of time. The data is fitted by a linear function and fit parameter  $b$ , the frequency drift, is collected in Table 7.3 (given in mHz/s). (c) This is one of the ten representative beats that were used to get the value for the beat linewidth in Table 7.2. Uncertainties of the parameters are with respect to the 67% ( $\pm 1\sigma$ ) confidence level.

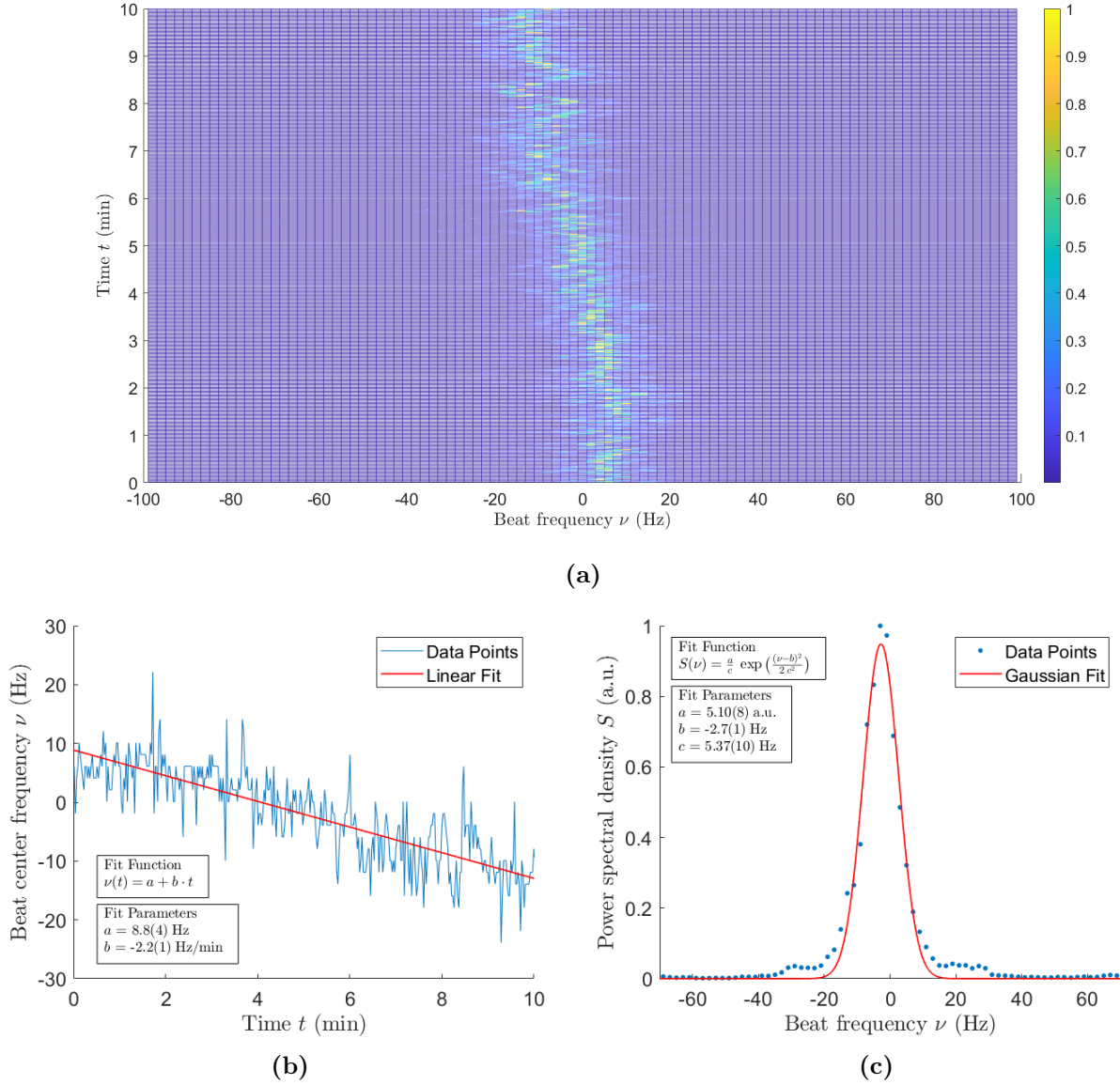


**Figure 7.8.:** Results from the three-cornered hat measurement, laser pair QSIM-Linear. (a) Spectrogram measurement of the QSIM-Linear beat using the *R&S FSV 3004* spectrum analyzer. The spectrogram shows the power spectral density as a function of frequency and time. The bar on the right shows the color for each value of the normalized power spectral density in arbitrary units. The chosen settings on the spectrum analyzer are: Resolution bandwidth 3 Hz, video bandwidth 3 Hz, sweep time 1.4 s, frequency span 200 Hz. As the spectrum analyzer would interpolate data at a video bandwidth of 3 Hz, only every fifth point was kept. (b) Drift of the QSIM-Linear beat center frequency over time. The data is created by plotting the maximum frequency per line in (a) as a function of time. The data is fitted by a linear function and fit parameter  $b$ , the frequency drift, is collected in Table 7.3 (given in mHz/s). (c) This is one of the ten representative beats that were used to get the value for the beat linewidth in Table 7.2. The plateaus between  $\pm 30$  to  $\pm 20$  are most likely servo bumps, although we do not know the origin. Uncertainties of the parameters are with respect to the 67% ( $\pm 1\sigma$ ) confidence level.

**Table 7.3.: Frequency drifts of the laser pairs and lasers involved in the three-cornered hat measurement.** The first three lines of data show the beat center frequency drift of the spectrograms that were recorded for the three-cornered hat measurement. In Figure 7.6 the spectrogram and the beat drift is shown for the QFC-QSIM beat, in Figure 7.7 for the QFC-Linear beat and in Figure 7.8 for the QSIM-Linear beat. The next three lines of data show the absolute frequency drifts for each involved laser, calculated by Eq. (3.28), under the assumption that the linear drifts of the three involved lasers stay the same over the course of  $\sim 24$  h.

Laser Pair	Frequency drift $D$ (mHz/s)
QFC - QSIM	-408(3)
QFC - Linear	-370(2)
QSIM - Linear	-37(2)
Laser	Frequency drift $D$ (mHz/s)
QFC	-371(3)
QSIM	-38(3)
Linear	-1(3)

## 7.4. Ramsey Experiments on a Single Ion

Ramsey experiments (Subsection 3.2.2) were conducted to obtain a value for the new Ti:Sa laser's linewidth. To do so, 729 nm laser light from the new Ti:Sa laser was sent through the distribution board to the ion trap and onto a single trapped  $^{40}\text{Ca}^+$  ion that was prepared in the  $4^2S_{1/2, m_j=-1/2}$  ground state. In order to remove magnetic field fluctuations from the subsequent calculation of the laser linewidth (Eq. (3.37)), two different qubit transitions were driven. The chosen transitions were  $4^2S_{1/2, m_j=-1/2} \rightarrow 3^2D_{5/2, m_j=-3/2}$  and  $4^2S_{1/2, m_j=-1/2} \rightarrow 3^2D_{5/2, m_j=+3/2}$ .

For each transition, nine different Ramsey contrast measurements for waiting times  $\tau$  between 0 ms and 4 ms were taken. In Figure 7.9 the results of the Ramsey contrast measurements are shown for the  $4^2S_{1/2, m_j=-1/2} \rightarrow 3^2D_{5/2, m_j=-3/2}$  transition for waiting times of 0 ms, 2 ms and 3.5 ms. For each waiting time, functions of the type

$$p_1(\phi_1) = a \cdot \cos^2(b \cdot \phi_1 + c) + d \quad (7.3)$$

were used to fit the data, following the theoretical prediction from Eq. (3.32), where  $a$  is the contrast. The offset parameter  $d$  additionally takes oscillation damping into account. The Ramsey contrast measurement results for the other transitions are not shown directly, but their contrasts were obtained in the same way. The measured contrasts for both transitions as a function of the waiting time is shown in Figure 7.10. Here, Gaussian functions of the type

$$C(\tau) = a \cdot \exp(-b \cdot \tau^2) \quad (7.4)$$

were used to fit the data. This Gaussian fit follows from the theory of Ramsey experiments presented in [58], but includes a prefactor  $a$ . This prefactor takes into account that even at a waiting time of 0 ms the contrast does not have to be 1, for example because of imperfect  $\hat{R}_{x,y}(\pi/2, \phi_1)$  gates. Considering Eq. (3.34), the frequency  $\nu_a$  can be extracted from the fit parameter  $b$  in Eq. (7.4). The frequency  $\nu_a$  includes the laser linewidth and an effective

## 7. Results at UIBK

additional laser linewidth broadening due to magnetic field noise on the ion, as can be seen in Eq. (3.35). In general, the frequency  $\nu_a$  is given by

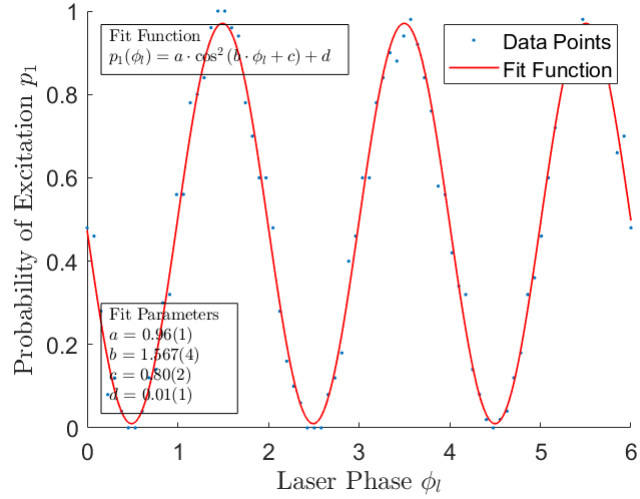
$$\nu_a = \frac{2}{\pi} \sqrt{\ln(2)b}. \quad (7.5)$$

Specifically, the frequency for the  $4^2S_{1/2, m_j=-1/2} \rightarrow 3^2D_{5/2, m_j=-3/2}$  transition calculates to  $\nu_{a,1} = 184(8)$  Hz and the for the  $4^2S_{1/2, m_j=-1/2} \rightarrow 3^2D_{5/2, m_j=+3/2}$  transition to  $\nu_{a,2} = 243(6)$  Hz. The sensitivities of the two transitions with regard to magnetic field fluctuations (Eq. (3.36)) are  $\kappa_1 = 11.2$  GHz/T for  $-1/2 \rightarrow -3/2$  and  $\kappa_2 = 39.2$  GHz/T for  $-1/2 \rightarrow +3/2$ . Combining these values in Eq. (3.37) gives

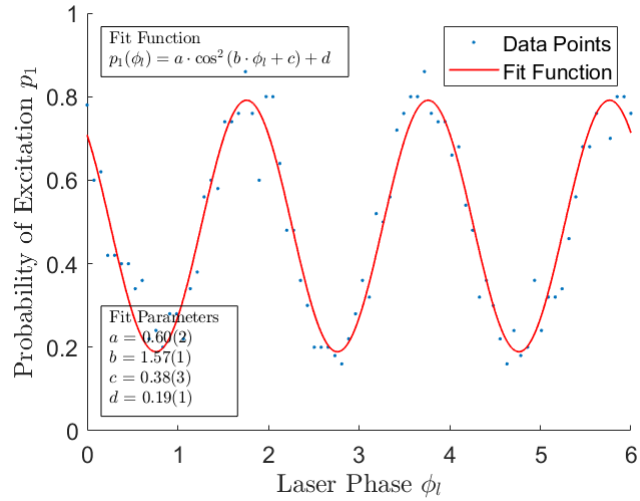
$$\Delta\nu = 178(10) \text{ Hz} \quad (7.6)$$

for the Ti:Sa laser linewidth (FWHM) from Ramsey experiments.

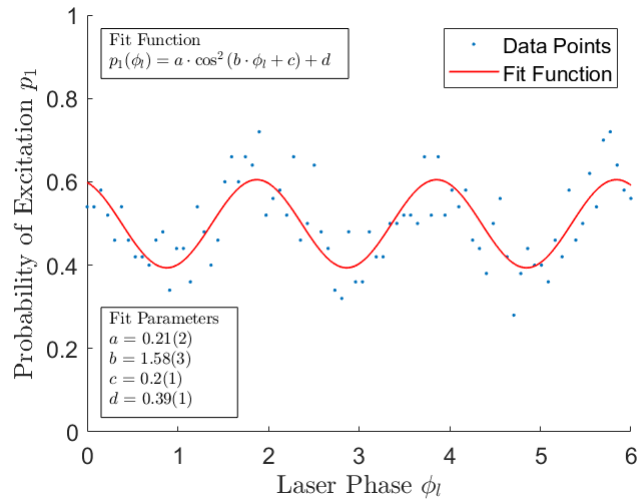
## 7. Results at UIBK



(a) Wait time of 0 ms.



(b) Wait time of 2 ms.



(c) Wait time of 3.5 ms.

**Figure 7.9.:** Excitation of the  $4^2S_{1/2}, m_j = -1/2 \rightarrow 3^2D_{5/2}, m_j = -3/2$  transition when the laser phase is scanned after different wait times. (a) Wait time of 0 ms, (b) wait time of 2 ms, (c) wait time of 3.5 ms. The contrast  $C$  is the fit parameter  $a$ . Uncertainties of the parameters are with respect to the 67% ( $\pm 1\sigma$ ) confidence level.

## 7. Results at UIBK

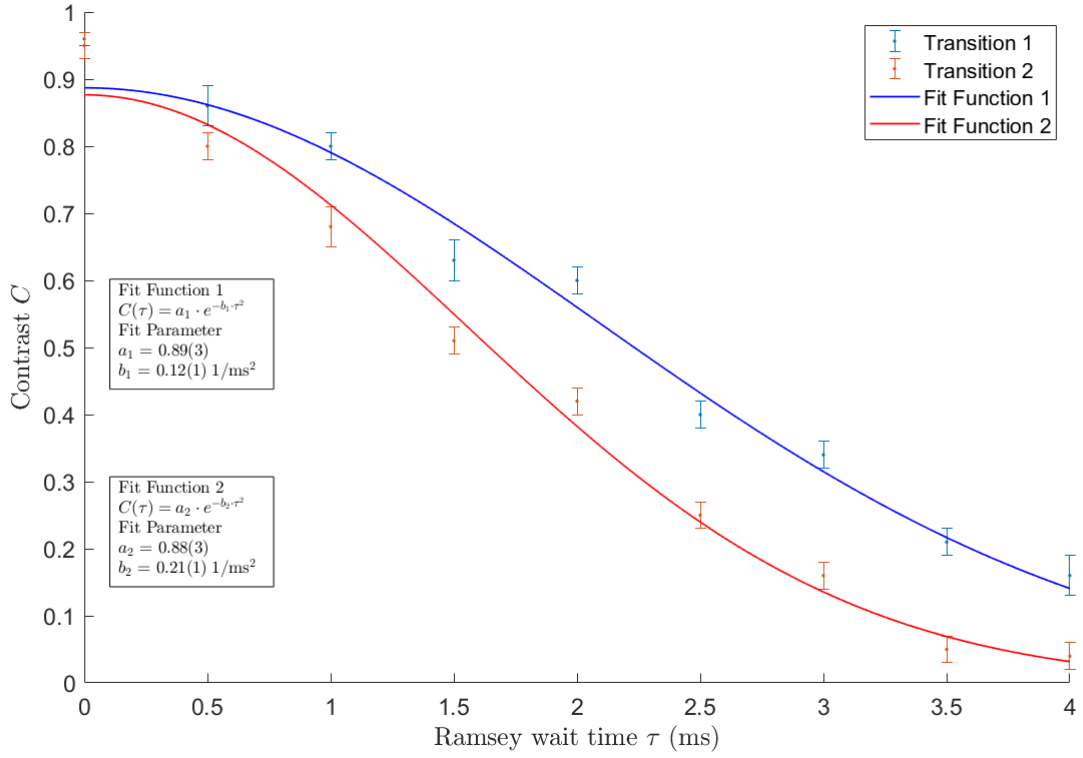


**Figure 7.10.: Ramsey contrast of two different transitions as a function of wait time.** Transition 1 is  $4^2S_{1/2}, m_j = -1/2 \rightarrow 3^2D_{5/2}, m_j = -3/2$  and transition 2 is  $4^2S_{1/2}, m_j = -1/2 \rightarrow 3^2D_{5/2}, m_j = +3/2$ . The fit is modeled according to the theory presented in [58]. Uncertainties of the parameters are with respect to the 67% ( $\pm 1\sigma$ ) confidence level.

## 7.5. Towards a sub-10 Hz Linewidth

After collecting unequivocal evidence that the Ti:Sa laser linewidth was  $> 100$  Hz, the goal was to find reasons for that and reduce the linewidth to  $< 10$  Hz, ideally towards 1 Hz. Helene Hainzer reports in her thesis a linewidth of  $26.7(2)$  Hz for the Raman laser emitting light at 729 nm when locked to the reference cavity in Figure 5.2 that is also used to lock the new Ti:Sa laser [52]. We attempted to reproduce this sub-100 Hz linewidth by locking the Raman laser again at 729 nm to this reference cavity. However, when repeating this measurement, the results showed a Raman-QSIM beat at 729 nm with a linewidth in the  $\sim 100$  Hz regime, similar to all the beat linewidths that we observed using the new Ti:Sa laser. To exclude any electronic devices in the vicinity from being the culprit for a broadened beat linewidth, we switched off the ICE-BLOCs and the chiller of the new Ti:Sa laser as well as the temperature controller and the ion pump of the reference cavity. None of these attempts showed a change in the Raman-QSIM beat linewidth at 729 nm.

These results, involving the Raman laser, provide evidence that the new Ti:Sa laser itself is not responsible for the unsatisfactory linewidth obtained when locking it to the reference cavity. A possible cause of the problem therefore is the reference cavity itself, mechanically vibrating and changing length, as was described in Subsection 4.3.2. Further evidence for this is provided by the observation that reductions in the amplitude of the error signal made by the list of changes in Subsection 7.3.2 were not found to make any significant change in the beat linewidth. That is, improving the PDH lock of the new Ti:Sa laser to the cavity was not reflected in a narrower beat linewidth.

Separately, we identified that the air conditioning (AC) system of UIBK first floor causes mechanical vibrations in the laboratory. The new Ti:Sa laser is located in one of three laboratories at UIBK first floor and each laboratory has an adjacent AC system. After arranging a date with the responsible company, the AC for our laboratory was switched off first, followed by the AC of the other two laboratories. Continuous QFC-QSIM beat measurements were taken during the whole process. In Figure 7.11a, a beat measurement with the QSIM Ti:Sa laser is shown when all AC systems were still on that day. In Figure 7.11b a beat is shown when the AC system of our QFC team was switched off. Finally, Figure 7.11c presents a beat measurement where all AC systems on the floor were switched off. The first beat shows a linewidth of  $\Delta\nu = 165(2)$  Hz. The second beat with our QFC AC switched off gives a linewidth of  $\Delta\nu = 42(2)$  Hz. The third beat measurement with every AC switched off yields a linewidth of  $\Delta\nu = 4.6(1)$  Hz. While a Gaussian fit of the type Eq. (6.1) (without offset  $d$ ) suited the data in Figure 7.11a best, Lorentzian fits

$$S(\nu) = \frac{a \cdot c}{(\nu - b)^2 + (\frac{c}{2})^2} \quad (7.7)$$

had to be used for Figure 7.11b and 7.11c after using an  $R^2$  test to compare the models. Comparing this insight about the lineshapes to the theory in Subsection 3.1.3 suggests that low-frequency noise contributions to the beat linewidth were reduced by switching the AC systems off. The distribution of data points in Figure 7.11c cannot be explained by a Lorentzian as well as the distribution can for Figure 7.11b. The distribution of data points in Figure 7.11c is to some extent comparable to the frequency plateaus that can be seen in Figure 7.8c, so it might be a feature of the QSIM laser that becomes visible when the beat linewidth is narrowed down enough. Only further investigation into the QSIM lineshape can confirm this claim. In the case of a Lorentzian lineshape, the FWHM of the laser linewidth is connected to the fit parameter  $c$  via  $\Delta\nu = c$ , as can be seen in Subsection 3.2.1.

We have two possible explanations for the linewidth narrowing when the AC systems were

## 7. Results at UIBK

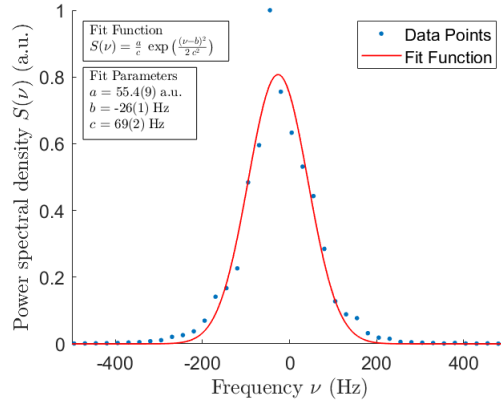
switched off. The first is that mechanical vibrations on the reference cavity were mitigated. The second is that fiber noise in the 140 m long fiber that brings QSIM light from the UIBK ground floor to the UIBK first floor was reduced. However, recalling the QFC-Linear beat linewidth of 158(5) Hz from the three-cornered hat measurement in Table 7.2, which employs a separate FNC setup and a separate 140 m long PM fiber, we have strong evidence that not only fiber noise on the QSIM light is responsible for the broad QFC-QSIM beat linewidth. So our best guess is that by switching off the AC systems, both mechanical vibrations on the reference cavity and fiber noise on the QSIM light were mitigated.

Until this point, as described in Chapter 5, the reference cavity is sitting on a 12.7 mm thick *Thorlabs MB6090/M* aluminium breadboard, the cavity breadboard. The cavity breadboard is on top of a 10 cm thick layer of sand, which in turn lies in the wooden shielding box. The box sits on a floated optical table. As a consequence of our experimental results that are presented in this Section, we removed the sand and bought a *Accurion Halcyonics\_Variobasic* vibration isolation board that was placed inside the wooden shielding box underneath a 5.8 cm thick *Honeycomb SG breadboard* with the cavity breadboard on top. The vibrational platform therefore serves to decouple the cavity breadboard from both the optical table and the wooden box. With all AC systems switched on again, a QFC-Linear beat measurement was repeated. An average linewidth was created from five beats that were fitted with a Lorentzian curve. One of the five beats is shown in Figure 7.12 as a representative. The average linewidth is

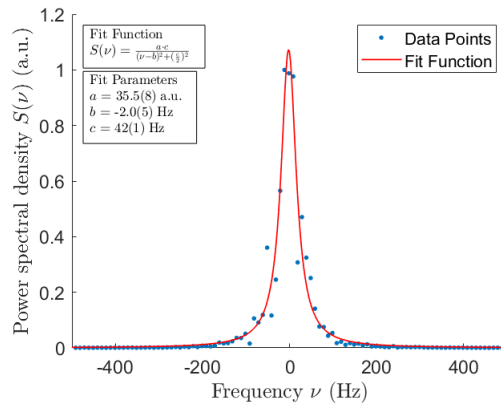
$$\Delta\nu = 4.2(17) \text{ Hz} \tag{7.8}$$

using Eq. (6.2), representing an upper limit for the Titanium:Sapphire laser linewidth. The standard deviation of the individual beat linewidths was taken as the linewidth uncertainty. As the QFC-Linear beat was conducted with the vibration isolation board installed but the AC systems on, we have collected corroborating evidence that mechanical vibrations on the reference cavity were responsible for the new Ti:Sa laser linewidth in the  $\sim 100$  Hz regime.

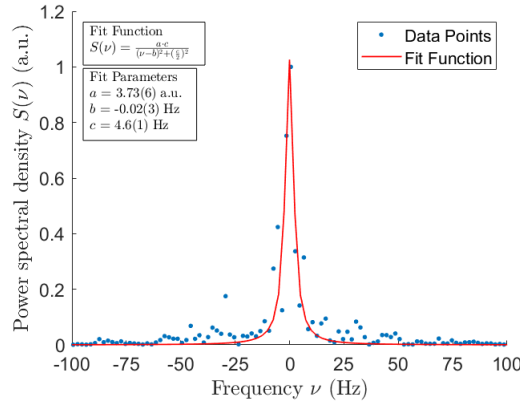
## 7. Results at UIBK



(a) Measurement settings: Resolution bandwidth 1 Hz, video bandwidth 1 Hz (5 data points were binned into one post-measurement, so effectively the video bandwidth is 5 Hz), sweep time 1 s, frequency Span 5 kHz. The linewidth calculates to  $\Delta\nu = \sqrt{8 \ln(2)} \cdot c = 162(5)$  Hz.



(b) Measurement settings: Resolution bandwidth 1 Hz, video bandwidth 1 Hz, sweep time 1 s, frequency Span 2 kHz. The linewidth calculates to  $\Delta\nu = c = 42(1)$  Hz.



(c) Measurement settings: Resolution bandwidth 1 Hz, video bandwidth 1 Hz, sweep time 2 s, frequency Span 2 kHz. The linewidth calculates to  $\Delta\nu = c = 4.6(1)$  Hz.

**Figure 7.11.: QFC-QSIM beat at 729 nm at UIBK when the AC is switched off.** (a) The AC on first floor at UIBK is on, (b) the AC is switched off only for the QFC lab and (c) the AC is switched off. The beat center frequency was set to 0 and the power spectral density was normalized to 1. The data points are fitted by a Gaussian model for (a) and by a Lorentzian fit model for (b) and (c). The data was taken by a *R&S FSV 3004* spectrum analyzer. Uncertainties of the parameters are with respect to the 67% ( $\pm 1\sigma$ ) confidence level.

## 7. Results at UIBK

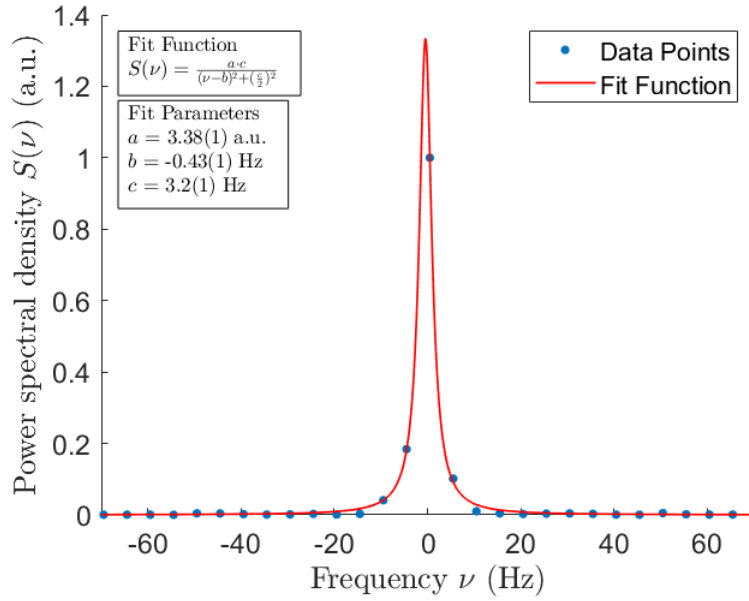


**Figure 7.12.: QFC-Linear beat at 729 nm at UIBK after installing the vibration isolation board.** This is one representative of the five beats that were used to get the value for the beat linewidth in Eq. (7.8). The beat center frequency was set to 0 and the power spectral density was normalized to 1. The data points are fitted by a Lorentzian model. The data was taken by a *R&S FSV 3004* spectrum analyzer, settings: Resolution bandwidth 1 Hz, video bandwidth 1 Hz, sweep time 1 s, frequency Span 5 kHz. The linewidth (FWHM) of this example beat calculates to  $\Delta\nu_{\text{ex}} = c = 3.2(1)$  Hz. Uncertainties of the parameters are with respect to the 67% ( $\pm 1\sigma$ ) confidence level.

The frequency resolution of the *Rohde and Schwarz FSV 3004* spectrum analyzer is 0.01 Hz according to the data sheet, so error bars cannot be visible along the frequency axis. The maximum uncertainty of level measurement is 0.07 dB ( $1\sigma$ ), so error bars are of the size of the data points and cannot be visible along the power spectral density axis.

## 8. Conclusion and Outlook

The goal of this master project was to frequency-stabilize the new Ti:Sa laser at a wavelength of 729 nm to a linewidth on the order of 1 Hz. An additional requirement was that the laser has to stay locked for several days. Both requirements were fulfilled.

The master thesis gave an introduction to quantum mechanics and qubits in the first theory chapter. The ion species  $^{40}\text{Ca}^+$  was introduced as a platform into which qubits can be encoded. The chapter concluded with a description of how to perform a universal gate set using a  $^{40}\text{Ca}^+$  ion, which makes it possible to use this ion in quantum information science experiments. The realization was that a laser at a wavelength of 729 nm is needed so that a universal gate set can be performed. The second theory chapter first treated lasers in general and then more specifically the concept of the laser linewidth. The chapter finished with a generic description of the Titanium-doped Sapphire laser, which is a prime candidate for a 729 nm laser. The third theory chapter dealt with control theory and especially the concept of PID control. After presenting how a cavity can be used as a frequency reference, the Pound-Drever-Hall (PDH) locking technique for lasers was presented. The experimental setup that was realized during the master project was then described in the next chapter.

Our results that showed the path towards a sub-10 Hz linewidth were given in the following two chapters. Several techniques were implemented and necessary to obtain the final result. First, the PDH technique was used to lock the new Ti:Sa laser to an external reference cavity. A first beat with the QSIM Ti:Sa laser at IQOQI gave an estimate for the new Ti:Sa laser's linewidth in the regime of  $\sim 100$  Hz. Second, fiber noise cancellation for the fiber that connects the laser and the cavity breadboards was installed after the move to UIBK. Third, intensity stabilization was engaged at UIBK for all three lasers that need to be simultaneously locked to the reference cavity. All stabilization feedback loops were examined and the conclusion was that after stabilization, neither fiber nor intensity noise are responsible for a laser linewidth broadening  $> 1$  Hz. The two lists in Subsection 7.3.2 show several permanent changes to the experimental setup, as well as temporary investigations, to reduce the laser linewidth below 10 Hz at UIBK. However, a beat measurement with the QSIM Ti:Sa laser, a three-cornered hat measurement with the QSIM and Linear Ti:Sa lasers as well as Ramsey experiments on a single trapped ion did not show a linewidth below 100 Hz for the new Ti:Sa laser. Only when mechanical vibrations were mitigated by either switching off the air conditioning system on the entire floor or installing a vibration isolation board beneath the cavity breadboard, a sub-10 Hz linewidth was finally achieved. That behavior was unexpected since the wooden shielding box, in which the reference cavity was sitting on sand, is sat on a state-of-the-art floated optical table.

Several other obstacles had to be overcome in the master project. First, due to space and COVID-19 restrictions, the new Ti:Sa laser and the reference cavity had to be placed in two different laboratories at IQOQI. This required fiber and cable connections of 30 m length along the IQOQI ceiling. Fiber noise in these long fibers likely limited the obtained beat linewidth in those preliminary beat measurements at IQOQI. A second obstacle was that a few months after starting laser operation, the *MSquared SolsTiS* new Ti:Sa laser was malfunctioning as it was spontaneously switching off. These events happened for as long as a month, and eventually the laser had to be sent back to the factory for more than three

## 8. Conclusion and Outlook

months. During this time period between September and December 2021, no beat measurements could be performed and no progress in laser frequency stabilization could be made. However, the time was used to deepen theoretical knowledge behind the Pound-Drever-Hall locking technique and to prepare the experimental setup for the time when the SolsTiS laser returned. The third obstacle was the move to the new laboratory, which meant setting up the laser system and the laser frequency stabilization in an unknown new environment. Eventually, this new environment is assumed to be the main cause for a broad laser linewidth above 100 Hz in the form of unknown mechanical vibrations on the reference cavity. Figuring out what caused this broad laser linewidth was an endeavor that went on for several months. It takes both time and experience to get to know the different devices that are used in the experimental setup, which is reflected in the oddly chosen FALC parameters at IQOQI or the sometimes suboptimal settings of the spectrum analyzer for the beat measurements.

The narrowest measured beat linewidth, as presented in Section 7.5, is 4.2(17) Hz (FWHM), representing an upper limit for the new Ti:Sa laser's linewidth. This value for the beat linewidth was obtained by taking an average of five beat measurements when the vibration-isolation board was installed and all AC systems were switched on at UIBK first floor. We will continue to take beat measurements with the QSIM Ti:Sa laser and the Linear Ti:Sa laser to assure ourselves that the new Ti:Sa laser linewidth stays in the regime of sub-10 Hz. We are also planning to increase the stability of the PDH lock further by programming an auto-lock that brings the laser frequency back on resonance with the reference cavity in case the laser unlocks spontaneously. We assume that we may be able to further reduce the new Ti:Sa laser linewidth in the future. This could be achieved by switching to a new reference cavity with a higher finesse, by further shielding the reference cavity from noise from the environment or by finding better FALC parameters using the proposal that is presented in Appendix Chapter C.

The drift of the new Ti:Sa laser is -371(3) mHz/s. This value was calculated from the spectrograms shown in Chapter 7 that were recorded as part of the three-cornered hat measurement, under the assumption that the linear drifts of the three involved lasers stay the same over the course of  $\sim 24$  h. In the future, we aspire to reduce the drift by finding better PID parameters for the reference cavity temperature controller.

In the future, the stabilized new Ti:Sa laser will be used for quantum information science experiments in our QFC team. Future experiments in our team where the new Ti:Sa laser will be involved include the creation of a photonic link between multiple ion traps, while the individual ion traps are scaled to operate with up to 10 ions. Further, multipartite entanglement and quantum metrology are areas of research in our team that require frequency-stabilized 729 nm laser light. The stabilized new Ti:Sa laser is also regularly used by the 2D crystals team, led by Christian Roos. The first paper of this team, which gives an insight into the experimental setup and the experiments to come, is already put on the arXiv [82]. The quantum molecules team, led by Philipp Schindler, will also perform experiments in the future that require the stabilized new Ti:Sa laser, but their laboratory construction is just now (mid-2022) beginning. One more application is that if another research team or group sets up a new laser system at 729 nm, the new Ti:Sa laser can act as a reference laser in a beat measurement or a three-cornered hat measurement. Finally, there is the option to give stabilized laser light at 729 nm through the distribution board to the experiments on the ground floor of UIBK as a backup. This would happen under the condition that the Linear laser fails, an eventuality that has to be considered as we know from our own experience. The 729 nm qubit laser is the workhorse for quantum information science experiments with trapped  $^{40}\text{Ca}^+$  ions. Whenever qubit manipulation over a coherence time of up to a few hundred milliseconds is needed, the new Ti:Sa laser can do the job.

# A. Step-by-step Derivation of the PDH Error Signal

This appendix chapter is meant to derive the PDH error signal  $e(\nu)$  that was presented as a result in Eq. (4.28) step-by-step. The chapter is devoted to the reader who wants to deal with the PDH technique extensively and who is interested in a mathematical derivation of the PDH error signal on a level of detail I was not able to find in any available text. The starting point is the expression for the phase-modulated cavity-incident electric field in Eq. (4.24),

$$E_i = E_0 e^{i(2\pi\nu t + \beta \sin(2\pi\Omega t))}. \quad (\text{A.1})$$

In this equation,  $E_0$  is the electric field amplitude,  $\nu$  is the laser frequency,  $t$  time and  $\Omega$  is the modulation frequency. The modulation index  $\beta$  tells how much the modulated variable of the signal, the phase, varies around its unmodulated level. The sin function in the exponent varies between  $\pm 1$  over time, and so the modulation index  $\beta$  is a multiplication factor that increases or decreases this range.

## Expansion of the cavity-incident electric field in Bessel functions

This part of the appendix chapter was mostly written by the help of [70]. Bessel functions  $J_n(z)$  are the solutions of the differential equation

$$\frac{d^2}{dz^2} J_n(z) + \frac{1}{z} \frac{d}{dz} J_n(z) + \left(1 - \frac{n^2}{z^2}\right) J_n(z) = 0 \quad (\text{A.2})$$

with  $n \in \mathbb{N}$ . One way to express the solution of the above differential equation is

$$J_n(z) = \frac{1}{2\pi i} \oint u^{-n-1} e^{\frac{1}{2} z(u^2-1)/u} du \quad (\text{A.3})$$

where the contour is a circle around the origin  $u = 0$ . The function  $e^{\frac{1}{2} z(u^2-1)/u}$  has an *essential singularity* at  $u = 0$ , one that is neither a pole nor a removable singularity. A function  $f(z)$  can be expanded at a point  $h$  around an essential singularity  $a$  using a *Laurent series*,

$$f(a+h) = \sum_{n=-\infty}^{\infty} a_n h^n \quad (\text{A.4})$$

with

$$a_n = \frac{1}{2\pi i} \oint \frac{f(z)}{(z-a)^{n+1}} dz. \quad (\text{A.5})$$

### A. Step-by-step Derivation of the PDH Error Signal

For  $f(z) = e^{\frac{1}{2} z(u^2-1)/u}$ , the coefficients  $a_n$  of a Laurent series around  $u = 0$  are exactly  $J_n(z)$ ,

$$e^{\frac{1}{2} z(u^2-1)/u} = \sum_{n=-\infty}^{\infty} u^n J_n(z). \quad (\text{A.6})$$

This result can now be used for an expansion of Eq. (A.1). For  $u = e^{2\pi i \Omega t}$  and  $z = \beta$ , the Laurent series of the function reads

$$e^{i\beta \sin(2\pi \Omega t)} = \sum_{n=-\infty}^{\infty} e^{2\pi i n \Omega t} J_n(\beta). \quad (\text{A.7})$$

It is now the role of the modulation index  $\beta$  to determine the value of the Bessel functions for each  $n$ . Plotting  $J_n(\beta)$  for different values of  $\beta$  shows that for  $\beta < 1$  or close to 1, the Bessel functions with  $n = 0$  and  $n = \pm 1$  are much larger than the Bessel functions of  $n = \pm 2$  or  $n$  greater/smaller. It is therefore possible to approximate Eq. (A.7) to

$$e^{i\beta \sin(2\pi \Omega t)} \stackrel{\beta < 1}{\approx} e^{-2\pi i \Omega t} J_{-1}(\beta) + J_0(\beta) + e^{2\pi i \Omega t} J_1(\beta). \quad (\text{A.8})$$

This regime for the modulation index is the desired regime for the PDH technique. The PDH technique needs a carrier ( $n = 0$ ) and one pair of sidebands ( $n = \pm 1$ ), while all the other sidebands are ideally suppressed. By further using the identity  $J_{-n}(z) = -J_n(z)$ , the result from Eq. (A.8) is now plugged into Eq. (A.1) to yield the approximate cavity-incident electric field expanded in Bessel functions,

$$E_i = E_0 e^{i(2\pi \nu t + \beta \sin(2\pi \Omega t))} \stackrel{\beta < 1}{\approx} E_0 e^{2\pi i \nu t} \cdot (J_0(\beta) + J_1(\beta) e^{2\pi i \Omega t} - J_1(\beta) e^{-2\pi i \Omega t}). \quad (\text{A.9})$$

#### The power signal

The cavity-incident electric field of Eq. (A.9) can be thought to be separated into three fields, one oscillating at  $\nu$ , one at  $\nu + \Omega$  and one at  $\nu - \Omega$ . The reflected electric field is given as in Eq. (4.16). Each cavity-incident field in Eq. (A.9) has its own reflection signal, so

$$E_r = E_0 e^{2\pi i \nu t} (\mathcal{R}(\nu) J_0(\beta) + \mathcal{R}(\nu + \Omega) J_1(\beta) e^{2\pi i \Omega t} - \mathcal{R}(\nu - \Omega) J_1(\beta) e^{-2\pi i \Omega t}). \quad (\text{A.10})$$

This reflected electric field is incident on the photodiode that measures the field's power and converts it into an electric current. The different devices that are mentioned in this chapter are depicted in Figure 4.4. The power of an electric field is calculated according to Eq. (3.13), so that the power of the photodiode-incident field is

$$P_r = \int_A \frac{1}{2} \epsilon_0 c |E_r|^2 dA \quad (\text{A.11})$$

where  $\epsilon_0$  is the electric field constant,  $c$  the speed of light in vacuum and  $A$  the surface area. For the electric field  $E_r$  with a uniform field amplitude  $E_0$ , the integration over the area yields a constant factor  $A$ . The measured power then is

### A. Step-by-step Derivation of the PDH Error Signal

$$\begin{aligned}
P_r &= \frac{1}{2}\epsilon_0 c A |E_r|^2 = \frac{1}{2}\epsilon_0 c A E_0^2 \cdot \left( |\mathcal{R}(\nu)|^2 J_0^2(\beta) + |\mathcal{R}(\nu + \Omega)|^2 J_1^2(\beta) + |\mathcal{R}(\nu - \Omega)|^2 J_1^2(\beta) \right. \\
&\quad + 2J_0(\beta) J_1(\beta) \left( \operatorname{Re} \left\{ \mathcal{R}(\nu) \mathcal{R}^*(\nu + \Omega) - \mathcal{R}^*(\nu) \mathcal{R}(\nu - \Omega) \right\} \cos(2\pi\Omega t) \right. \\
&\quad \left. - \operatorname{Im} \left\{ \mathcal{R}(\nu) \mathcal{R}^*(\nu + \Omega) - \mathcal{R}^*(\nu) \mathcal{R}(\nu - \Omega) \right\} \sin(2\pi\Omega t) \right) \\
&\quad \left. + \mathcal{R}(\nu + \Omega) \mathcal{R}^*(\nu - \Omega) J_1^2(\beta) e^{4\pi i \Omega t} - \mathcal{R}^*(\nu - \Omega) \mathcal{R}(\nu + \Omega) J_1^2(\beta) e^{-4\pi i \Omega t} \right)
\end{aligned} \tag{A.12}$$

In order to obtain this equation, the identity

$$r e^{ix} + r^* e^{-ix} = 2 \operatorname{Re}\{r\} \cos(x) - 2 \operatorname{Im}\{r\} \sin(x) \tag{A.13}$$

where  $r \in \mathbb{C}$  and  $x \in \mathbb{R}$  was used. Now, the carrier power  $P_C = \frac{1}{2}\epsilon_0 c A E_0^2 J_0^2(\beta)$  and the sideband power  $P_S = \frac{1}{2}\epsilon_0 c A E_0^2 J_1^2(\beta)$  are introduced. The Bessel functions indicate how much power is in the carrier and how much power is in the sidebands. The terms oscillating at  $\Omega$  are created through interference between the carrier and the sidebands, while the terms oscillating at  $2\Omega$  arise from interference of the sidebands [69]. The last two terms in Eq. (A.12) can be ignored, as the first low-pass filter in the PDH lock setup removes the power components oscillating at  $2\Omega$ . After including these changes, the photodiode-incident power reads

$$\begin{aligned}
P_r &= P_C |\mathcal{R}(\nu)|^2 + P_S |\mathcal{R}(\nu + \Omega)|^2 + P_S |\mathcal{R}(\nu - \Omega)|^2 \\
&\quad + 2\sqrt{P_C P_S} \left( \operatorname{Re} \left\{ \mathcal{R}(\nu) \mathcal{R}^*(\nu + \Omega) - \mathcal{R}^*(\nu) \mathcal{R}(\nu - \Omega) \right\} \cos(2\pi\Omega t) \right. \\
&\quad \left. - \operatorname{Im} \left\{ \mathcal{R}(\nu) \mathcal{R}^*(\nu + \Omega) - \mathcal{R}^*(\nu) \mathcal{R}(\nu - \Omega) \right\} \sin(2\pi\Omega t) \right).
\end{aligned} \tag{A.14}$$

### The error signal

As previously stated, the terms in the power signal oscillating at  $\Omega$  are created through interference between the carrier and the sidebands. Information about the carrier frequency is conveyed through the sidebands: While  $\mathcal{R}(\nu)$  is symmetric in frequency around  $\Delta\nu_{\text{FSR}}$ , the real and imaginary parts of  $\mathcal{R}(\nu) \mathcal{R}^*(\nu + \Omega) - \mathcal{R}^*(\nu) \mathcal{R}(\nu - \Omega)$  are not. This is where the asymmetry can be found that is needed for control theory: A nonzero amplitude of the power component oscillating at  $\Omega$  shows that the laser frequency is not on resonance with the cavity, and through the asymmetry it is known whether the frequency is below or above resonance.

The modulation frequency  $\Omega$  is chosen so high in comparison to the cavity linewidth that the sidebands are assumed to be completely reflected, rendering  $\mathcal{R}(\nu + \Omega) = \mathcal{R}(\nu - \Omega) = -1$ , and the expression

$$\mathcal{R}(\nu) \mathcal{R}^*(\nu + \Omega) - \mathcal{R}^*(\nu) \mathcal{R}(\nu - \Omega) = -2i \operatorname{Im} \left\{ \mathcal{R}(\nu) \right\} \tag{A.15}$$

turns entirely imaginary. This sets the real part in Eq. (A.14) to 0, and only the power term with  $\sin(2\pi\Omega t)$  remains. A mixer now multiplies a sinusoidal function at frequency  $\Omega'$  with the signal that is recorded by the photodiode. A multiplication of two sinusoidal functions at different frequencies  $\Omega$  and  $\Omega'$  can be rewritten as

$$\sin(2\pi\Omega t + \phi) \cdot \sin(2\pi\Omega' t) = \frac{1}{2} \left( \cos(2\pi(\Omega - \Omega')t + \phi) - \cos(2\pi(\Omega + \Omega')t + \phi) \right). \tag{A.16}$$

### A. Step-by-step Derivation of the PDH Error Signal

An emphasis on the relative phase  $\phi$  and the importance of its value in the PDH technique was already given in Subsection 4.3.2. The function generator signal can be written as

$$V_f = V_{f,0} \cdot \sin(2\pi\Omega't) \quad (\text{A.17})$$

where  $V_{f,0}$  is the output voltage amplitude of the function generator that can be manually chosen. The photodiode creates a current  $I_{\text{ph}}$  that is proportional to the photodiode-incident power  $P_r$  according to Eq. (4.34). The current  $I_{\text{ph}}$  induces a voltage  $V_r$  in the mixer through inductive coupling. The two voltages are multiplied by the mixer, yielding a signal  $V_{\text{mix}}$  that is proportional to

$$V_{\text{mix}} \propto V_f V_r \propto -2V_{f,0} \sqrt{P_C P_S} \text{Im} \left\{ \mathcal{R}(\nu) \mathcal{R}^*(\nu + \Omega) - \mathcal{R}^*(\nu) \mathcal{R}(\nu - \Omega) \right\} \cdot \frac{1}{2} \left( \cos(2\pi(\Omega - \Omega')t + \phi) - \cos(2\pi(\Omega + \Omega')t + \phi) \right). \quad (\text{A.18})$$

In the PDH technique, the modulation frequencies  $\Omega$  and  $\Omega'$  are generated by the same frequency generator, so both frequencies are the same and  $\Omega - \Omega' = 0$ . The second low-pass filter in the PDH lock setup removes the voltage component at  $\Omega + \Omega'$ , so that the voltage for the error signal is proportional to

$$V_{\text{err}} \propto -V_{f,0} \sqrt{P_C P_S} \text{Im} \left\{ \mathcal{R}(\nu) \mathcal{R}^*(\nu + \Omega) - \mathcal{R}^*(\nu) \mathcal{R}(\nu - \Omega) \right\} \cdot \cos(\phi). \quad (\text{A.19})$$

The asymmetry of the imaginary part has remained up until this point, and this frequency-dependent voltage is finally given to the controller. Usually, the error signal is written as

$$e(\nu) = -\sqrt{P_C P_S} \text{Im} \left\{ \mathcal{R}(\nu) \mathcal{R}^*(\nu + \Omega) - \mathcal{R}^*(\nu) \mathcal{R}(\nu - \Omega) \right\} \cdot \cos(\phi) \quad (\text{A.20})$$

as it was in Eq. (4.28). However, Eq. (A.19) shows that also the chosen voltage  $V_{f,0}$  at the frequency generator changes the amplitude of the error signal. Changing the function generator voltage was one of the attempts to lower the laser linewidth and is included in the list in Subsection 7.3.2.

The analytical expression for the imaginary part that introduces the frequency-asymmetry into the error signal is

$$\begin{aligned} & \text{Im} \left\{ \mathcal{R}(\nu) \mathcal{R}^*(\nu + \Omega) - \mathcal{R}^*(\nu) \mathcal{R}(\nu - \Omega) \right\} \\ &= \frac{-2r^2 \sin\left(\frac{2\pi\Omega}{\Delta\nu_{\text{FSR}}}\right) + 2r^4 \sin\left(\frac{2\pi\Omega}{\Delta\nu_{\text{FSR}}}\right) + (r - r^5) \cdot \left( \sin\left(\frac{2\pi\nu}{\Delta\nu_{\text{FSR}}}\right) - \sin\left(\frac{2\pi(\nu+\Omega)}{\Delta\nu_{\text{FSR}}}\right) \right)}{1 - 2r^2 \left( \cos\left(\frac{2\pi\nu}{\Delta\nu_{\text{FSR}}}\right) + \cos\left(\frac{2\pi(\nu+\Omega)}{\Delta\nu_{\text{FSR}}}\right) \right) + 2r^4 \left( 1 + \cos\left(\frac{2\pi(2\nu+\Omega)}{\Delta\nu_{\text{FSR}}}\right) + \cos\left(\frac{2\pi\Omega}{\Delta\nu_{\text{FSR}}}\right) \right) - 2r^6 \left( \cos\left(\frac{2\pi\nu}{\Delta\nu_{\text{FSR}}}\right) + \cos\left(\frac{2\pi(\nu+\Omega)}{\Delta\nu_{\text{FSR}}}\right) \right) + r^8} \\ &- \frac{-2r^2 \sin\left(\frac{2\pi\Omega}{\Delta\nu_{\text{FSR}}}\right) + 2r^4 \sin\left(\frac{2\pi\Omega}{\Delta\nu_{\text{FSR}}}\right) - (r - r^5) \cdot \left( \sin\left(\frac{2\pi\nu}{\Delta\nu_{\text{FSR}}}\right) - \sin\left(\frac{2\pi(\nu-\Omega)}{\Delta\nu_{\text{FSR}}}\right) \right)}{1 - 2r^2 \left( \cos\left(\frac{2\pi\nu}{\Delta\nu_{\text{FSR}}}\right) + \cos\left(\frac{2\pi(\nu-\Omega)}{\Delta\nu_{\text{FSR}}}\right) \right) + 2r^4 \left( 1 + \cos\left(\frac{2\pi(2\nu-\Omega)}{\Delta\nu_{\text{FSR}}}\right) + \cos\left(\frac{2\pi\Omega}{\Delta\nu_{\text{FSR}}}\right) \right) - 2r^6 \left( \cos\left(\frac{2\pi\nu}{\Delta\nu_{\text{FSR}}}\right) + \cos\left(\frac{2\pi(\nu-\Omega)}{\Delta\nu_{\text{FSR}}}\right) \right) + r^8}. \end{aligned} \quad (\text{A.21})$$

It can be seen from this expression that the PDH error signal is dependent on the cavity mirrors reflection amplitude  $r$ , so via Eq. (4.22) on the finesse  $F$ , the modulation frequency  $\Omega$ , the free spectral range  $\Delta\nu_{\text{FSR}}$  and the laser frequency  $\nu$ . For small time-dependent frequency disturbances around resonance,  $\nu = N \cdot \Delta\nu_{\text{FSR}} + \delta\nu(t)$  with  $N \in \mathbb{N}$ , this equation reproduces the linear behavior that was approximated in Eq. (4.32).

## B. Analysis of the PDH Error Signal at UIBK

In this appendix chapter an analysis of the PDH error signal of the locked new Ti:Sa laser at UIBK is presented. Figure B.1a shows a trace of the PDH error signal when the laser frequency is scanned over 60 MHz around the resonance, from “left to right” in the figure. As a comparison, the theoretical prediction of the PDH error signal is depicted in Figure 4.5. The measured PDH error signal in Figure B.1a as a function of laser frequency differs from the theoretical prediction in Figure 4.5: The error signal shows some oscillatory behavior when the laser frequency is scanned from left to right in the figure. This feature, that does not appear in the theoretical model, arises from the finite photon lifetime inside the cavity. A light field builds up inside the reference cavity when the laser is on resonance. When the laser is not on resonance with the cavity anymore, the light field intensity inside the cavity rings down and leaks through the mirrors. The leaking laser light interferes constructively and destructively (as a function of time) with the incident laser field, which can be made out as oscillations in the error signal. The intention was to choose the modulation index in Figure B.1a close to the optimal value of  $\beta = 1.08$ . We estimated to be close to this optimal value as the first sidebands in Figure B.1a are approximately half as high as the carrier (discussion in Subsection 4.3.2) and the second sidebands at twice the modulation frequency, 22 MHz, are suppressed to a negligible amplitude (discussion in Appendix Chapter A).

Figure B.1b shows the Fast-Fourier transform (FFT) of the PDH error signal when the new Ti:Sa laser is locked. The FALC parameters are chosen as shown in Table 7.1. The three highest peaks in the FFT are at 1.4 kHz, 18.8 kHz and 53 kHz. The peak at 1.4 kHz is likely a mechanical resonance inside the new Ti:Sa laser, as it can be amplified by playing a tune at this specific frequency next to the laser head. The peak at 18.8 kHz is from the dither frequency that is used for the etalon top-of-fringe lock. This peak can be increased or decreased in amplitude by adjusting the “dither level” on the SolsTiS homepage. We assume that the peak at 53 kHz is a resonance that is affiliated with one of the Piezo elements inside the new Ti:Sa laser that is used for frequency feedback. The peak can be amplified by increasing the main gain of FALC1 that controls the fast and slow Piezos and it can also be decreased when the main gain is decreased. However, we deliberately do not decrease the main gain further as the chosen value for the main gain yields a better PDH lock stability. By further increasing the main gain at FALC1, a bump in the FFT at around 70 kHz appears that is of the same magnitude as the peak at 53 kHz. Similarly, by increasing the main gain of FALC2 that controls the intracavity EOM, a bump appears at around 30 kHz that is several kHz broad and also of the same magnitude as the peak at 53 kHz.

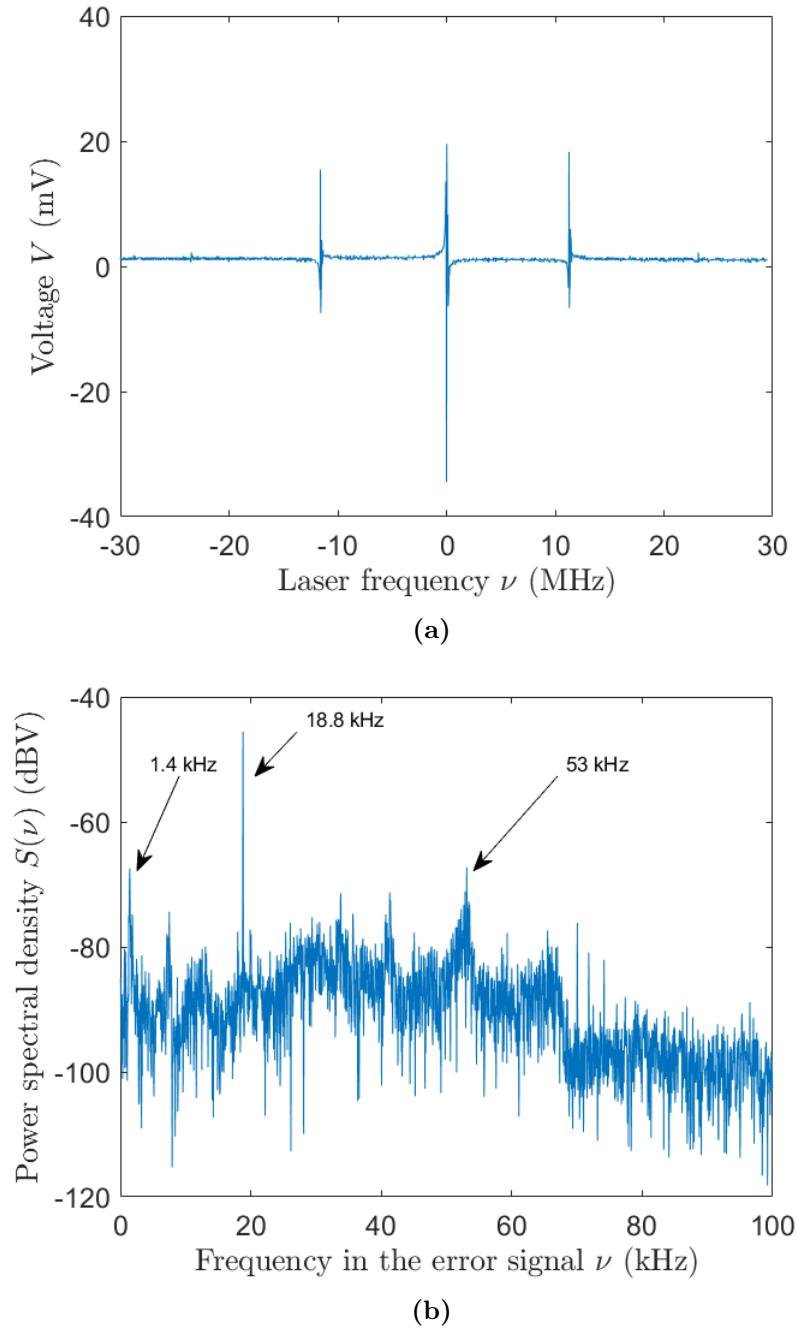


**Figure B.1.: Analysis of the new Ti:Sa laser error signal at UIBK.** Figure (a) shows the error signal when the laser frequency is scanned over the cavity resonance frequency, which is set to  $\nu = 0$ . The theoretical prediction of the function can be seen in Figure 4.5. The second sidebands can be seen as a small bump at twice the modulation frequency of 11 MHz. Figure (b) displays the FFT of the error signal when the new Ti:Sa laser is locked. The three highest peaks in the FFT are at 1.4 kHz, 18.8 kHz and 53 kHz.

## C. Proposing a Way to Optimize FALC Parameters in the PDH Lock

When control theory was introduced in Section 4.1, a strong emphasis was put on a description of the elements in a feedback loop in the frequency picture and a derivation of the transfer function of a PID controller. Even though the mathematical framework is necessary to understand why and how the PDH technique works, our approach in the master project to find FALC parameters was one of trial-and-error. The FALC parameters were chosen as is described in Subsection 5.3.1: Different actuators give corrections over different frequency ranges, with transition zones in which two actuators correct for frequency components in the error signal. Further, the fast Fourier transform of the error signal was viewed on an oscilloscope and the parameters at the FALC were chosen so that the power spectral density became as low as possible. In this appendix chapter, a proposal is given for a way to find the optimal FALC parameters in the PDH lock by using the mathematical tools that were developed in Section 4.1.

The reference signal in the PDH technique that is set by the reference cavity is

$$w(t) = \nu_w \tag{C.1}$$

where  $\nu_w$  is the reference cavity's resonance frequency, an integer multiple of the cavity's free spectral range. The ideal output signal is a laser that is locked exactly to the resonance frequency with zero linewidth. However, a discussion on the Schawlow-Townes limit in Subsection 3.1.3 and the shot-noise limit in Subsection 4.3.2 already showed that a laser with zero linewidth is fundamentally unattainable. A controller cannot narrow the laser linewidth below these fundamental limits, but other mechanisms that broaden the linewidth are collectively described by the disturbance  $d(t)$ , and a controller can correct for that. According to Eq. (4.4) and Eq. (4.5) it is possible to write the error signal in the frequency picture as

$$E(s) = W(s) \cdot \left(1 - \frac{G(s)S(s)}{1 + G(s)S(s)}\right) - D(s) \cdot \frac{S(s)}{1 + G(s)S(s)} \tag{C.2}$$

The Laplace transform of  $w(t)$  is known to be

$$W(s) = \int_0^\infty \nu_w e^{-st} dt = \frac{\nu_w}{s}. \tag{C.3}$$

The transfer function  $S(s)$  is given by the actuator elements and the transfer function  $G(s)$  is given by the controller and the chosen settings. The unknown part in the error signal comes from the disturbance  $D(s)$ . A look at Eq. (4.32) shows that for small changes from the resonance frequency, the error signal is directly proportional to frequency deviations  $\delta\nu(t)$ . These frequency deviations lead to a linewidth broadening and are introduced into the feedback loop through  $D(s)$ .

The proposal to optimally correct for  $D(s)$  in the feedback loop is now presented. First, the actuator transfer function  $S(s)$  for all involved actuators (in the PDH lock of this thesis e.g., the fast Piezo, the slow Piezo and the intracavity EOM) have to be found. This can be done by experimentally determining the *frequency response* of the elements in a test circuit. More information on the frequency response is given in [65] and [66]. Then, information about the controller (this thesis: FALC) transfer function  $G(s)$  has to be obtained. This information may be estimated through the data that is given in the controller manual (for the FALC the manual is [76]), or the controller transfer function frequency response can also be experimentally determined in a test circuit. The next step is to determine the disturbance  $D(s)$ . One attempt would be to find the most crucial constituents in the disturbance through an educated guess. However, the laser system and the environment seem to be too complex for this attempt. Another option is to somehow lock the laser through trial-and-error with the FALC parameters (it does not even have to be locked, just “sticking” to the resonance frequency for some time is sufficient) and record a time trace of the error signal. This error signal  $e(t)$  can then be transformed into  $E(s)$  and plugged into Eq. (C.2). Then, the disturbance  $D(s)$  can be calculated.

Combining both lines in Eq. (4.4) gives an expression for the output signal,

$$Y(s) = W(s) \cdot \frac{G(s)S(s)}{1 + G(s)S(s)} + D(s) \cdot \frac{S(s)}{1 + G(s)S(s)}. \quad (\text{C.4})$$

In this equation,  $W(s)$  is known from Eq. (C.3),  $D(s)$  is known from the error signal and  $S(s)$  is known from experimentally determining the frequency response. It is now the art of control theory to agree on an output signal  $Y(s)$ . The mandatory criterion is that the output shows *stability*. Further, it has to be decided how the system responds to low and high frequency components in the disturbance, how much these frequency components are damped, how much overshoot is acceptable and so on. The task is to find an output that corresponds to “the narrowest laser linewidth”. For a chosen  $G(s)$ , the output signal  $Y(s)$  can be calculated and back-transformed into the time picture  $y(t)$ . A simulated beat measurement with another perfectly stabilized laser can give a laser linewidth for the chosen  $G(s)$ . An optimization program can then scan through various functions  $G(s)$  to find the narrowest possible linewidth. Then, the FALC parameters that allow for the best approximation to  $G(s)$  are chosen for the real PDH lock.

This proposal was not tested or used in the master project. It requires knowledge of the transfer functions of all actuators and of all settings combinations on the controllers. The approach also assumes that  $W(s)$  is described by one function through all time, which is known to be wrong: The reference cavity expands over time, leading to a drift in resonance frequency, and effects like cavity vibrations change the reference signal on a much smaller timescale. Nonetheless, with an additional level of sophistication, changes in  $w(t)$  can also be considered. As a last point, the finite time it takes for signals to travel at the speed of light through free space and optical fibers and as electrical signals through cables will certainly have to be considered, too. The proposal requires the capability to numerically solve for  $y(t)$  and of optimization, this should be a possible task for a program like *Matlab*.

## D. Simulation of a Controller's Response to a Step Disturbance

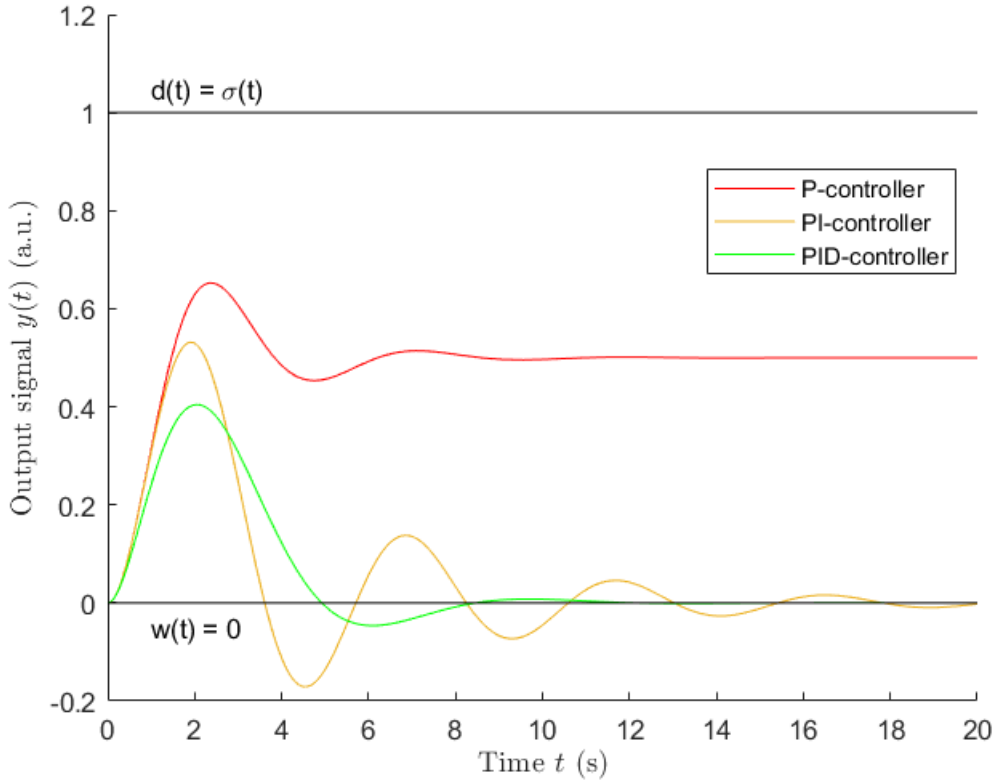


**Figure D.1.: The response of different controllers due to a step function disturbance.**

This Figure is supplementing the presentation of the principles of PID control in Subsection 4.1.2. Controllers correct the output signal  $y(t)$  for a disturbance  $d(t)$ . The reference signal is  $w(t) = 0$ , and at  $t = 0$  a step disturbance  $d(t) = \sigma(t)$  happens, where  $\sigma$  is the Heaviside function. The plant transfer function is  $S(s) = \omega_0^2 / (\omega_0^2 + \omega_0 s / \gamma + s^2)$ , where  $\omega_0$  is the actuator resonance frequency and  $\gamma$  the damping factor of the actuator resonance. This plant transfer function is an adequate description of e.g., a mirror attached to a Piezo element [74]. It can be seen that the P-controller corrects for the step disturbance, but never reaches  $y(t) = 0$  again because of the steady state error. The PI-controller overcomes the steady state error, but the output signal  $y(t)$  oscillates. This oscillation can be significantly reduced by the PID-controller. The D-part has a sharp reaction to the initial disturbance, but starts to reduce the slope of  $y(t)$  towards the value  $w(t) = 0$ . The chosen parameters are  $\omega_0 = 1 \text{ s}^{-1}$ ,  $\gamma = 1$ ,  $k_P = 1$ ,  $k_I = 1$ ,  $k_D = 1$ .

# Bibliography

- [1] R. Landauer. Information is a physical entity. *Physica A: Statistical Mechanics and its Applications*, 263:63–67, 1999.
- [2] T. D. Ladd, F. Jelezko, R. Laflamme, Y. Nakamura, C. Monroe, and J. L. O’Brien. Quantum computers. *Nature*, 464:45–53, 2010.
- [3] D. Deutsch. Quantum theory, the church-turing principle and the universal quantum computer. *Proc. R. Soc. Lond. A*, 400:97–117, 1985.
- [4] D. Deutsch and R. Josza. Rapid solution of problems by quantum computation. *Proc. R. Soc. Lond. A*, 439:553–558, 1992.
- [5] P. W. Shor. Algorithms for quantum computation: discrete logarithms and factoring. In *Proceedings of the 35th Annual Symposium on Foundations of Computer Science*, pages 124–134, 1994.
- [6] L. K. Grover. A fast quantum mechanical algorithm for database search. In *Proceedings of the 28th Annual ACM Symposium on the Theory of Computing*, pages 212–219, 1996.
- [7] D. P. DiVincenzo. The physical implementation of quantum computation. *Fortschritte der Physik*, 48:771–783, 2000.
- [8] N. Friis, O. Marty, C. Maier, C. Hempel, M. Holzäpfel, P. Jurcevic, M. B. Plenio, M. Huber, C. Roos, R. Blatt, and B. P. Lanyon. Observation of entangled states of a fully controlled 20-qubit system. *Phys. Rev. X*, 8:021012, 2018.
- [9] F. Arute, K. Arya, and J. M. Martinis et al. Quantum supremacy using a programmable superconducting processor. *Nature*, 574:505–510, 2019.
- [10] R. P. Feynman. Simulating physics with computers. *International Journal of Theoretical Physics*, 21:467–488, 1982.
- [11] J. I. Cirac and P. Zoller. Goals and opportunities in quantum simulation. *Nature Phys*, 8:264–266, 2012.
- [12] H. J. Kimble. The quantum internet. *Nature*, 453:1023–1030, 2008.
- [13] W. Dür, H.-J. Briegel, J. I. Cirac, and P. Zoller. Quantum repeaters based on entanglement purification. *Phys. Rev. A*, 59:169–181, 1999.
- [14] N. Gisin and R. Thew. Quantum communication. *Nature Photonics*, 1:165–171, 2007.
- [15] C. Monroe and J. Kim. Scaling the ion trap quantum processor. *Science*, 339:1164–1169, 2013.

- [16] C. H. Bennett and G. Brassard. An update on quantum cryptography. In G. R. Blakley and D. Chaum, editors, *Advances in Cryptology*, volume 196 of *CRYPTO 1984. Lecture Notes in Computer Science*. Springer, 1985.
- [17] Artur K. Ekert. Quantum cryptography based on Bell's theorem. *Phys. Rev. Lett.*, 67:661–663, 1991.
- [18] S. Pirandola, U. L. Andersen, L. Banchi, M. Berta, D. Bunandar, R. Colbeck, D. Englund, T. Gehring, C. Lupo, C. Ottaviani, J. L. Pereira, M. Razavi, J. Shamsul Shaari, M. Tomamichel, V. C. Usenko, G. Vallone, P. Villoresi, and P. Wallden. Advances in quantum cryptography. *Adv. Opt. Photon.*, 12:1012–1236, 2020.
- [19] W. Heisenberg. *Der Teil und das Ganze*. Piper Verlag Gmbh, 2001.
- [20] V. Giovannetti, S. Lloyd, and L. Maccone. Quantum-enhanced measurements: Beating the standard quantum limit. *Science*, 306:1330–1336, 2004.
- [21] Jeremy L. O'Brien. Optical quantum computing. *Science*, 318:1567–1570, 2007.
- [22] Immanuel Bloch. Quantum coherence and entanglement with ultracold atoms in optical lattices. *Nature*, 453:1016–22, 2008.
- [23] H. Häffner, C.F. Roos, and R. Blatt. Quantum computing with trapped ions. *Physics Reports*, 469:155–203, 2008.
- [24] M. H. Devoret and R. J. Schoelkopf. Superconducting circuits for quantum information: An outlook. *Science*, 339:1169–1174, 2013.
- [25] W. Gao, A. Imamoglu, H. Bernien, and R. Hanson. Coherent manipulation, measurement and entanglement of individual solid-state spins using optical fields. *Nature Photonics*, 9:363–373, 2015.
- [26] J. I. Cirac and P. Zoller. Quantum computations with cold trapped ions. *Phys. Rev. Lett.*, 74:4091–4094, 1995.
- [27] C. Monroe, D. M. Meekhof, B. E. King, W. M. Itano, and D. J. Wineland. Demonstration of a fundamental quantum logic gate. *Phys. Rev. Lett.*, 75:4714–4717, 1995.
- [28] F. Schmidt-Kaler, H. Häffner, M. Riebe, and et al. Realization of the Cirac-Zoller controlled-NOT quantum gate. *Nature*, 422:408–411, 2003.
- [29] H. C. Nägerl, Ch. Roos, D. Leibfried, H. Rohde, G. Thalhammer, J. Eschner, F. Schmidt-Kaler, and R. Blatt. Investigating a qubit candidate: Spectroscopy on the  $S_{1/2}$  to  $D_{5/2}$  transition of a trapped calcium ion in a linear paul trap. *Phys. Rev. A*, 61:023405, 2000.
- [30] P. Schindler, D. Nigg, T. Monz, J. T. Barreiro, E. Martinez, S. X. Wang, S. Quint, M. F. Brandl, V. Nebendahl, C. F. Roos, M. Chwalla, M. Hennrich, and R. Blatt. A quantum information processor with trapped ions. *New Journal of Physics*, 15:123012, 2013.
- [31] P. A. Barton, C. J. S. Donald, D. M. Lucas, D. A. Stevens, A. M. Steane, and D. N. Stacey. Measurement of the lifetime of the  $3d^2D_{5/2}$  state in  $^{40}\text{Ca}^+$ . *Phys. Rev. A*, 62:032503–032501, 2000.

## Bibliography

- [32] R. W. P. Drever, J. L. Hall, F. V. Kowalski, J. Hough, G. M. Ford, A. J. Munley, and H. Ward. Laser phase and frequency stabilization using an optical resonator. *Appl. Phys. B*, 31:97–105, 1983.
- [33] R. V. Pound. Electronic frequency stabilization of microwave oscillators. *Review of Scientific Instruments*, 17:490–505, 1946.
- [34] M. A. Nielsen and I. L. Chuang. *Quantum Computation and Quantum Information*. Cambridge University Press, 2010.
- [35] C. Cohen-Tannoudji, B. Diu, and F. Laloë. *Quantenmechanik Band 1*. de Gruyter, 2009.
- [36] E. Chitambar and G. Gour. Quantum resource theories. *Rev. Mod. Phys.*, 91:025001, 2019.
- [37] A. Einstein, B. Podolsky, and N. Rosen. Can quantum-mechanical description of physical reality be considered complete? *Phys. Rev.*, 47:777–780, 1935.
- [38] R. Horodecki, P. Horodecki, M. Horodecki, and K. Horodecki. Quantum entanglement. *Rev. Mod. Phys.*, 81:865–942, 2009.
- [39] C. Hempel. *Digital quantum simulation, Schrödinger cat state spectroscopy and setting up a linear ion trap*. PhD thesis, University of Innsbruck, 2014.
- [40] W. Paul. Electromagnetic traps for charged and neutral particles. *Rev. Mod. Phys.*, 62:531–540, 1990.
- [41] C. F. Roos. *Controlling the quantum state of trapped ions*. PhD thesis, University of Innsbruck, 2000.
- [42] C. Cohen-Tannoudji, J. Dupont-Roc, and G. Grynberg. *Atom-Photon Interactions: Basic Processes and Applications*. Wiley - VCH, 1998.
- [43] J. D. Jackson. *Classical Electrodynamics*. John Wiley & Sons, 2021.
- [44] J. Hu, Y. Chen, Y.-X. Bai, P.-S. He, Q. Sun, and A.-C. Ji. Corrections to atomic ground state energy due to interaction between atomic electric quadrupole and optical field. *Chin. Phys. B*, 27:043202, 2018.
- [45] C. J. Foot. *Atomic Physics*. Oxford University Press, 2005.
- [46] C. Cohen-Tannoudji, B. Diu, and F. Laloë. *Quantenmechanik Band 2*. de Gruyter, 2010.
- [47] D.F.V. James. Quantum dynamics of cold trapped ions with application to quantum computation. *Applied Physics B: Lasers and Optics*, 66:181–190, 1998.
- [48] D. Meschede. *Optics, Light and Lasers*. Wiley - VCH, 2017.
- [49] T.W. Hänsch and A.L. Schawlow. Cooling of gases by laser radiation. *Optics Communications*, 13:68–69, 1975.
- [50] D. J. Wineland and Wayne M. Itano. Laser cooling of atoms. *Phys. Rev. A*, 20:1521–1540, 1979.

## Bibliography

- [51] C. Cohen-Tannoudji and J. Dalibard. Single-atom laser spectroscopy. looking for dark periods in fluorescence light. *Europhysics Letters (EPL)*, 1:441–448, 1986.
- [52] H. Hainzer. *Laser Locking For Trapped-Ion Quantum Networks*. Master’s thesis, University of Innsbruck, 2018.
- [53] G. Kirchmair, J. Benhelm, F. Zähringer, R. Gerritsma, C. F. Roos, and R. Blatt. Deterministic entanglement of ions in thermal states of motion. *New Journal of Physics*, 11:023002, 2009.
- [54] D.J. Wineland, C. Monroe, W. M. Itano, D. Leibfried, B. E. King, and D.M. Meekhof. Experimental issues in coherent quantum-state manipulation of trapped atomic ions. *J. Res. Natl. Int. Stand. Technol.*, 103:259–328, 1998.
- [55] K. Mølmer and A. Sørensen. Multiparticle entanglement of hot trapped ions. *Phys. Rev. Lett.*, 82:1835–1838, 1999.
- [56] G. Di Domenico, S. Schilt, and P. Thomann. Simple approach to the relation between laser frequency noise and laser line shape. *Appl. Opt.*, 49:4801–4807, 2010.
- [57] L.-S. Ma, P. Jungner, J. Ye, and J. Hall. Delivering the same optical frequency at two places: accurate cancellation of phase noise introduced by an optical fiber or other time-varying path. *Optics Letters*, 19:1777–1779, 1994.
- [58] M. Chwalla. *Precision spectroscopy with  $^{40}\text{Ca}^+$  ions in a Paul trap*. PhD thesis, University of Innsbruck, 2009.
- [59] R. Stricker. *Gatteroperationen hoher Güte in einem optischen Quantenbit*. Master’s thesis, University of Innsbruck, 2017.
- [60] N. F. Ramsey. Experiments with separated oscillatory fields and hydrogen masers. *Rev. Mod. Phys.*, 62:541–552, 1990.
- [61] R. Paschotta. Titanium-sapphire lasers. [https://www.rp-photonics.com/titanium\\_sapphire\\_lasers.html](https://www.rp-photonics.com/titanium_sapphire_lasers.html). Taken on June 9, 2022.
- [62] K. F. Wall and A. Sanchez. Titanium sapphire lasers. *Lincoln Laboratory Journal*, 3:447–462, 1990.
- [63] A. Abragam and B. Bleaney. *Electron paramagnetic resonance of transition ions*. Oxford University Press, 1970.
- [64] DirectIndustry and Altechna. Titanium-doped sapphire ( $\text{Ti}:\text{Al}_2\text{O}_3$ ) crystal. <https://www.directindustry.com/prod/altechna/product-67070-1040033.html>. Taken on June 9, 2022.
- [65] G. F. Franklin, J. D. Powell, and A. Emami-Naeini. *Feedback Control of Dynamic Systems*. Pearson Education, 2019.
- [66] U. Tietze, C. Schenk, and E. Gamm. *Halbleiter-Schaltungstechnik*. Springer Vieweg, 2019.
- [67] J. L. Hall, M. S. Taubman, and J. Ye. *Laser Stabilization*. OSA Handbook v14, 1999.

## Bibliography

- [68] R. Neuhaus. TOPTICA Photonics AG: Diode laser locking and linewidth narrowing. Application note.
- [69] E. D. Black. An introduction to Pound-Drever-Hall laser frequency stabilisation. *Am. J. Phys.*, 69:79–87, 2001.
- [70] P. M. Morse and H. Feshbach. *Methods in Theoretical Physics, Part 1*. Feshbach Publishing, 1983.
- [71] E. Hirose, K. Kawabe, D. Sigg, R. Adhikari, and P. R. Saulson. Angular instability due to radiation pressure in the ligo gravitational-wave detector. *Appl. Opt.*, 49:3474–3484, 2010.
- [72] P. Dubé, A. Madej, J. Bernard, L. Marmet, and A. Shiner. A narrow linewidth and frequency-stable probe laser source for the  $^{88}\text{Sr}^+$  single ion optical frequency standard. *Applied Physics B*, 95:43–54, 2009.
- [73] M Squared Lasers Ltd. Solstis narrow linewidth, tunable cw ti:sapphire laser user manual v10.0. <https://www.manualslib.com/manual/1657768/M-Squared-Solstis.html>. Taken on June 27, 2022.
- [74] G. Kirchmair. *Frequency stabilization of a Titanium-Sapphire laser for precision spectroscopy on Calcium ions*, Diploma Thesis, University of Innsbruck, 2006.
- [75] J. Schupp. *Interface between trapped-ion qubits and travelling photons with close-to-optimal efficiency*. PhD thesis, University of Innsbruck, 2021.
- [76] TOPTICA Photonics AG. FALC 110 mFALC 110 Fast Analog Linewidth Control Manual.
- [77] Siglent. Spectrum analyzer basics: Bandwidth. <https://www.siglenteu.com/application-note/spectrum-analyzer-basics-bandwidth/>. Taken on August 5, 2022.
- [78] N. C. Wong and J. L. Hall. Servo control of amplitude modulation in frequency-modulation spectroscopy: demonstration of shot-noise-limited detection. *J. Opt. Soc. Am. B*, 2:1527–1533, 1985.
- [79] E. A. Whittaker, M. Gehrtz, and G. C. Bjorklund. Residual amplitude modulation in laser electro-optic phase modulation. *J. Opt. Soc. Am. B*, 2:1320–1326, 1985.
- [80] M. Bass, E. W. Van Stryland, D. R. Williams, and W. L. Wolfe. *Handbook of Optics Volume II: Devices, Measurements and Properties*. McGRAW-HILL, INC., 1995.
- [81] U. M. Körber. *Long-Lived and Efficient Qubit Memory for Photonic Quantum Networks*. PhD thesis, Max-Planck-Institut für Quantenoptik, Garching and Physik Department, Technische Universität München, 2020.
- [82] H. Hainzer, D. Kiesenhofer, T. Ollikainen, M. Bock, F. Kranzl, M. K. Joshi, G. Yoeli, R. Blatt, T. Gefen, and C. F. Roos. Correlation spectroscopy with multi-qubit-enhanced phase estimation. arXiv, 2022.

# Acknowledgements

I would like to thank all the people that helped me and supported me during my time as a master student, and without whom I would have not been able to finish my master.

First I want to thank Ben Lanyon, who allowed me to join his team as a master student after I had written my bachelor thesis with him. It was never a problem that after my bachelor I could only join the team off-season a year and a half later because of my military service, and I was greeted by Ben on the first day of my master project as if I had finished my bachelor thesis the day before. Ben knows how to communicate physics and find solutions to problems, and his enthusiasm and commitment were transferred to me and fueled my pursuit of new ideas and new attempts.

I would like to thank Rainer Blatt, an inspiring physicist, who created an outstanding research group at the University of Innsbruck. I am grateful to be a part of this group.

I am thankful to my team, first of all to Josef “OG” Schupp, who was a strict but fair mentor in my first months of my master project and who taught me to be tidy and persistent in experimental physics. I would like to thank all the members of my team that helped and supported me a lot: James Bate and Marco Canteri, two good lads, as well as Viktor Krutyanskiy, Zhe Xian Koong, Martin Meraner and Vojtech Krcmarsky. Especially towards the end of my project when a culprit for the broad laser linewidth was nowhere to be found, it was only the consequent teamwork that made the dream work.

I want to thank Christian Roos and his 2D crystals team. First I want to thank my office mates Helene Hainzer and Dominik Kiesenhofer who, after months of solitude in the new UIBK offices, now bring joy and meaningful discussions into every day. Helene was already working on laser stabilization and the reference cavity years ago, and I could stand firmly on the shoulders of her setup. I also want to thank the other members of the 2D crystals team: Matthias Bock, Tuomas Ollikainen and Artem Zhdanov.

I further want to thank Roman Stricker, Manoj Joshi and Milena Guevara-Bartsch from the Blatt group. I also thank all the staff from the mechanical and electronic workshops at IQOQI and UIBK and Claudia Mevenkamp, our institute secretary at UIBK.

Finally I want to say thank you to my parents without whom nothing of this would have been possible. I also want to thank my friends from university, my friends Mario, Tobias and Manuel, my flatmates Lorenz and Gibbs and the members of my music band.

The thesis was submitted on February 8, 2023. While preparing for the master thesis defense on March 13, 2023, small corrections to the text and to the equations were made in the thesis. No data or data analysis were changed.